BEHAVIOR OF SODIUM CLINOPYROXENES UNDER COMPRESSION

by

Andrew Charles McCarthy

_____

A Dissertation Submitted to the Faculty of the

DEPARTMENT OF GEOSCIENCES

In partial fulfillment of the Requirements
For the Degree of

DOCTOR OF PHILOSOPHY

In the Graduate College

THE UNIVERSITY OF ARIZONA

2007

THE UNIVERSITY OF ARIZONA
GRADUATE COLLEGE

As members of the Dissertation Committee, we certify that we have read the dissertation prepared by Andrew Charles McCarthy

entitled Behavior of Sodium Clinopyroxenes Under Compression

and recommend that it be accepted as fulfilling the dissertation requirement for the Degree of Doctor of Philosophy

_____ Date: 23 July 2007
Dr. Robert T. Downs

_____ Date: 23 July 2007
Dr. Bonner M. Denton

_____ Date: 23 July 2007
Dr. George Zandt

_____ Date: 23 July 2007
Dr. Charles T. Prewitt

_____ Date: 23 July 2007
Dr. Eric Seedorff

Final approval and acceptance of this dissertation is contingent upon the candidate's submission of the final copies of the dissertation to the Graduate College.

I hereby certify that I have read this dissertation prepared under my direction and recommend that it be accepted as fulfilling the dissertation requirement.

_____ Date: 23 July 2007
Dissertation Director: Dr. Robert T. Downs

STATEMENT BY AUTHOR

SIGNED: Andrew Charles McCarthy

ACKNOWLEDGMENTS

The research reported in this dissertation was made possible with funding from the National Science Foundation for the study Compression Mechanisms of Upper Mantle Minerals, grant No. EAR-9903104. The RRUFF Project, funded by Michael Scott, provided me employment during several years of my time as a graduate student.

My thanks go out to the members of my dissertation committee: Dr. Robert T. Downs, who took a chance on me as a student, employed me, and taught me much about an entirely new field (mineralogy); Dr. Charles T. Prewitt, who I am honored to have on my committee; Dr. Eric Seedorff, who was a late addition but has provided valuable feedback and interaction; Dr. Bonner Denton, a brilliant scientist I wish I could better emulate; and Dr. George Zandt, who has taught me much about tectonics and whose quiet, calm confidence I greatly admire.

I also thank those who have served as advisors to me in the past. Dr. Mihai Ducea convinced me to come to the University of Arizona in the first place, and got me through my first few years here; Dr. George Rossman was friendly, generous with his time and knowledge, and welcomed me into his lab; Drs. Jibamitra Ganguly and Clement Chase also provided assistance during portions of my graduate work.

Finally, I recognize my parents Michael and Christine, who never pushed me too hard in any particular direction; my brother Ryan, who inspires me with his penchant for quirky adventures; my good friend Erik Flesch, who at different times has been my student and my teacher; and my girl friend Debi Shaw Davis, who provided substantial support in the trying final months of this endeavor.

DEDICATION

I dedicate this work to:

Carl Sagan, for inspiring my interest in science as a child, as a college student,
and again in graduate school;

Ayn Rand, for setting forth an integrated system of thinking
that serves as a guide to my life;

—and—

Norman Borlaug, for his profound demonstration that
the human mind is the ultimate resource

TABLE OF CONTENTS

ABSTRACT.....7

INTRODUCTION.....9

Explanation of the Problem and its Context.....9

Literature Review.....10

Explanation of Dissertation Format.....10

PRESENT STUDY.....11

REFERENCES.....14

APPENDIX A – COMPRESSIBILITY TRENDS OF THE CLINOPYROXENES, AND IN-SITU HIGH-PRESSURE SINGLE-CRYSTAL X-RAY DIFFRACTION STUDY OF JADEITE.....15

APPENDIX B – IN-SITU HIGH-PRESSURE SINGLE-CRYSTAL X-RAY STUDY OF AEGIRINE, $NaFe^{3+}Si_2O_6$, AND THE ROLE OF M1 SIZE IN CLINOPYROXENE COMPRESSIBILITY.....66

APPENDIX C – $NaGaSi_2O_6$ CLINOPYROXENE AT HIGH PRESSURE: A RAMAN AND X-RAY SINGLE-CRYSTAL INVESTIGATION.....114

APPENDIX D – SUGGESTED FUTURE RESEARCH.....157

ABSTRACT

Three end-member clinopyroxenes from the $NaM1^{3+}Si_2O_6$ series, with M1 occupied by Al, Fe and Ga, have been examined by single-crystal X-ray diffraction at pressures up to 11 GPa. The $NaGaSi_2O_6$ end-member was also examined with Raman spectroscopy to 16.5 GPa. $NaAlSi_2O_6$ (jadeite) and $NaFeSi_2O_6$ (aegirine) are naturally occurring minerals, whereas $NaGaSi_2O_6$ is synthetic and not found in nature. Various characteristics of each of the three clinopyroxenes as a function of pressure are reported, including bulk moduli (K_0), unit cell volumes, atomic positions, and bond lengths. Phase transitions were sought but not observed and are postulated to occur at pressures above those achieved in the experiments reported here, based on observed changes in M2-O3 separations with pressure.

The compressibilities of a selection of clino- and orthopyroxenes from the literature were examined and considered in terms of M2-O3 bonding and unit cell volumes. As predicted by previous workers, pyroxene compressibilities generally correlate with unit cell volumes at ambient conditions. Compressibilities are also found, however, to be significantly affected by the relationship of M2-O3 bonds with the sense of rotation of silica tetrahedra upon compression. Two such relationships are observed: sympathetic, where the corner of the SiO_4 tetrahedron tilts toward M2, and antipathetic, where the corner of the tetrahedron tilts away from M2. All interatomic separations in pyroxenes decrease with pressure, but sympathetic-type separations decrease more than expected based on isotropic scaling of the unit cell. Pyroxene structures may have one of several M2-O3 bond configurations: none, one, two or four bonds, and none, only

sympathetic, only antipathetic, or a mixture of both types of bonds. Structures with antipathetic bonds are significantly stiffer than structures without, all other variables held constant. The presence of sympathetic M2-O3 bonds appears to have no effect on clinopyroxene compressibilities. The sympathetic/antipathetic bond hypothesis represents a new, previously unrecognized, first-order control on pyroxene compressibility.

M1 size controls ambient unit cell volumes of clinopyroxenes. However, M1 size does not correlate well with pyroxene bulk moduli. Applying the idea of sympathetic and antipathetic M2-O3 bonding, much of the dispersion in a plot of M1 cation size versus bulk modulus can be explained. The stiffening effect of antipathetic bonds is expected to cause dispersion in any plot of structural parameters versus clinopyroxene bulk moduli.

The three $NaM1^{3+}Si_2O_6$ clinopyroxenes examined in this study exhibit very similar behavior under compression. All show signs of approaching a $C2/c \rightarrow C2/c$ phase transition at ~20 GPa. All exhibit unit strain ellipsoids with similar orientations and dimensions. All have identical bond topologies and bulk moduli that correlate with their ambient unit cell volumes.

INTRODUCTION

Explanation of the Problem and its Context

Pyroxenes are common planetary materials. The Earth's upper mantle is thought to be >25% pyroxene minerals by volume. Since the mantle is not accessible for direct observation, studies of the mantle largely rely on modeling of mantle materials and geologic observations on materials thought or known to be present in the mantle. The input parameters for such models can be estimated, or they can be measured directly from mantle materials brought to high *P* or *T*. One important parameter of mantle models is the bulk modulus, which describes the compressibility of a material and its behavior in transmitting seismic waves. Pyroxenes are also known to undergo a variety of phase transitions at elevated *P* and *T* between at least five common polytypes. These transitions typically affect all the mineral's physical properties including density, bulk modulus, and the orientation and dimensions of the unit strain ellipsoid. Knowledge of the behavior of mantle materials at high *P* is essential for understanding the deep Earth.

The most common pyroxenes are those that contain the major Earth metals Ca, Mg, and Fe in the M cation sites (e.g., enstatite, ferrosilite, diopside, and hedenbergite). Somewhat less common volumetrically are pyroxenes that accommodate secondary major elements, such as Na. For this reason, the jadeite series structures, with the general formula $NaM1^{3+}Si_2O_6$, have historically been much less studied than the Ca+Mg+Fe pyroxenes. No systematic high-pressure structural studies have been reported prior to those herein. Knowledge about minerals such as the those of the jadeite series is

important when constructing accurate mantle models. Also, phase transitions in these relatively minor minerals can cause discontinuities in mantle properties.

Literature Review

Each appended manuscript contains a review of the relevant literature in its introduction. Previous work, where relevant, is also examined in the discussion sections.

Explanation of the Dissertation Format

This dissertation follows the University of Arizona Graduate College required format for dissertations composed primarily of published or publishable manuscripts. An introductory chapter and a research summary chapter serve to acquaint the reader with the nature of the research and major findings, which are presented in detail in three appended prepublication manuscripts.

The appended manuscripts were drafted almost entirely by me, and I am first author on all of the papers. I wrote all first drafts and I performed or controlled all subsequent revision work. My major advisor and co-author, Dr. Robert T. Downs, provided assistance with my presentation of ideas and with overall polishing of the manuscripts for publication. As my advisor, Dr. Downs also helped to guide the direction of my research and to identify which of my ideas were best to pursue. My co-author Dr. Richard M. Thompson provided valuable assistance and feedback at many steps in the writing process, and suggested many minor changes to improve the manuscripts.

PRESENT STUDY

The methods, results, and conclusions of this study are presented in three papers appended to this dissertation. The following is a summary of the major findings in these papers. This dissertation consists of three papers, each of which examines a $NaM1^{3+}Si_2O_6$ clinopyroxene at high pressure with single-crystal X-ray diffraction and also, in one case, high-pressure Raman spectroscopy. Along with the experimental results, a newly recognized first-order structural control on the compression of clinopyroxenes is explained and applied to explain dispersion in various clinopyroxene data.

The first paper reports a high-pressure single-crystal X-ray diffraction study of jadeite, $NaAlSi_2O_6$. In an effort to understand the wide variation in observed pyroxene compressibilities, a population of clino- and orthopyroxenes from the literature is examined. The pyroxene structures are found to approximately obey Bridgman's Law, which states that the bulk moduli of isostructural materials are proportional to their ambient unit cell volumes. However, for the clinopyroxenes, a significant range in bulk modulus is observed: from 69 GPa ($P2_1/c$ $ZnSiO_3$) to 148 GPa ($C2/c$ spodumene). A detailed examination of changes in the clinopyroxene structures with pressure reveals two types of M2-O3 bond behavior. As T-chains become more kinked, and individual tetrahedra rotate, one of the bridging oxygen atoms (O3) moves closer to M2 than would be expected based simply on scaled contraction of the unit cell, while the other bridging O3 atom in the same chain moves away from M2. When bonds are present across these M2-O3 separations, the first type tend to resist tetrahedral rotation, while the second type

tend to assist it. The resistive bonds tend to stiffen the structure and are termed "antipathetic". The assistive bonds would be expected to soften the structure and are termed "sympathetic". Two near-linear trends are identified in a plot of clinopyroxene bulk moduli versus ambient cell volumes. These trends are explained by the type of M2-O3 bonds present. The stiff upper trend contains structures that have some antipathetic bonds, while the lower soft trend contains structures with no antipathetic bonds.

The second paper reports a high-pressure single-crystal X-ray diffraction study of aegirine, $NaFe^{3+}Si_2O_6$. The idea that M1 size controls ambient unit cell volumes of the clinopyroxenes has been established (Thompon and Downs 2004). However, the correlation between M1 size and bulk modulus is examined and found to be poor. Invoking the antipathetic/sympathetic bond hypothesis from the jadeite study, and using an empirical model to "correct" the sympathetic bulk moduli, the entire population is brought more onto a single trend. Antipathetic/sympathetic bonding will cause dispersion in any plot of clinopyroxene parameters versus bulk modulus. Essentially, this phenomenon defines two distinct clinopyroxene groups in terms of compressibility.

The third and final paper reports a high-pressure single-crystal X-ray diffraction study and high-pressure Raman spectroscopy study of the synthetic clinopyroxene $NaGaSi_2O_6$. The $NaGaSi_2O_6$ bulk modulus, unit strain ellipsoid orientation and dimensions, and structural information with pressure are reported. Raman spectroscopy was collected to a pressure of 16.5 GPa in an attempt to observe a postulated $C2/c \rightarrow C2/c$ phase transition. Evidence for this transition was not observed in this study, but some notable changes did occur in the Raman spectra with pressure. The empirical

model put forth in Chapter 2 for calculating clinopyroxene bulk moduli is applied, and found to predict the bulk modulus of $NaGaSi_2O_6$ within ~3 GPa. The unit strain ellipsoid orientations and dimensions from a population of clinopyroxenes are considered, and bulk moduli are found to be correlated with ε_3, generally the most compressible axis.

REFERENCES FOR CHAPTERS 1 AND 2

Thompson, R.M., and Downs, R.T. (2004) Model pyroxenes II: Structural variation as a function of tetrahedral rotation. American Mineralogist, 89, 614–628.

APPENDIX A:

COMPRESSIBILITY TRENDS OF THE CLINOPYROXENES, AND IN-SITU HIGH-PRESSURE SINGLE-CRYSTAL X-RAY DIFFRACTION STUDY OF JADEITE

Compressibility trends of the clinopyroxenes, and in-situ high-pressure single-crystal X-ray diffraction study of jadeite

Andrew C. McCarthy*, Robert T. Downs, and Richard M. Thompson

Department of Geosciences, University of Arizona, Tucson, Arizona 85721-0077, U.S.A.

* E-mail: mccarthy@geo.arizona.edu

Abstract

The crystal structure of a natural jadeite, $NaAlSi_2O_6$, was studied at room temperature over the pressure range 0-9.17 GPa using single-crystal X-ray diffraction. Unit cell data were determined at 16 pressures, and intensity data were collected at nine of these pressures. A third-order Birch-Murnaghan equation of state fit to the *P*-*V* data yielded V_0 = 402.03(2) Å^3, K_0 = 136.5(14) GPa, and $K_0^{'}$ = 3.4(4). Jadeite exhibits strongly anisotropic compression with unit strain axial ratios of 1.00:1.63:2.10. Silicate chains become more O-rotated with pressure, reducing ∠O3-O3-O3 from 174.7(1)º at ambient pressure to 169.2(6)º at 9.17 GPa and bringing the anions of jadeite closer to a cubic closest-packed arrangement. No evidence of a phase transition was observed over the studied pressure range.

In an effort to understand pyroxene compressibilities, selected clinopyroxene bulk moduli were plotted against ambient unit cell volumes. Two trends were identified and are explained in terms of differences in M2–O3 bonding topologies and the geometric relationship of the bonds with tetrahedral rotation in the silicate chains. Bonds positioned

to favor the tetrahedral rotation upon compression are termed “sympathetic”, whereas bonds positioned to resist the rotation are termed “antipathetic”. Examination of the different pyroxene structures indicates that structures containing antipathetic M2–O3 bonds are less compressible than those with only sympathetic M2–O3 bonds. This behavior has not been previously recognized.

Introduction

This study examines the compressibilities of *C*2/*c* and $P2_1/c$ clinopyroxenes, taken from the literature, in terms of chemistry, symmetry and M2 bonding topology. In addition, this study presents new high-pressure X-ray diffraction data on jadeite. Clinopyroxenes have been the subject of many recent high-pressure single-crystal X-ray diffraction studies (Hugh-Jones and Angel 1994; Hugh-Jones et al. 1997; Zhang et al. 1997; Arlt et al. 1998; Yang et al. 1999; Arlt and Angel 2000; Hattori et al. 2000; Tribaudino et al. 2000; Origlieri et al. 2003; Gatta et al. 2005; Bindi et al. 2006; Downs and Singh 2006; Nestola et al. 2006a). Many of the clinopyroxenes have been found to undergo phase transitions with pressure, changing symmetry between *C*2/*c* and $P2_1/c$. For example, spodumene ($LiAlSi_2O_6$), $LiScSi_2O_6$ (Arlt and Angel 2000), and $LiFeSi_2O_6$ (Pommier et al. 2005) transform from *C*2/*c* to $P2_1/c$ with increasing pressure. $ZnSiO_3$ exhibits two transitions, from *C*2/*c* to $P2_1/c$ and to *C*2/*c* with increasing pressure (Arlt and Angel 2000). Previous attempts to examine systematics of clinopyroxene compressibilities have been thwarted by these phase transitions, which cause Birch-Murnaghan fits to cell parameter data across phase transitions to give spurious results,

especially the K_0' values. Recognition of the clinopyroxene phase transitions has allowed better calculation of compressibilities for these structures. The K_0' values—the accuracy of which reflect the quality of the cell parameter data and indicate the goodness of the Birch-Murnaghan fit to the data—now average ~3.5 for the clinopyroxenes considered in this study (Table 1). Still, a large dispersion exists in the compressibilities of clinopyroxenes which cannot be explained by unrecognized phase transitions or poor data quality.

Pyroxenes are a major component of the Earth's upper mantle. It appears that much of the upper mantle is composed of clinopyroxene, since orthopyroxene transforms to monoclinic symmetry at pressure equivalent to a depth of ~225 km (Hugh-Jones et al. 1996; Woodland 1998). The mantle contains non-trivial amounts of Na, and Na-clinopyroxenes appear to be stable over a wide range of mantle conditions. McDonough and Sun (1995) estimated a Na_2O content of the bulk silicate Earth (BSE) of 0.36%, equivalent to 2670 ppm Na. The major concentration mechanism for incompatible elements such as Na occurs at mid-ocean ridges, where mantle partial melting serves to partition Na into the basaltic oceanic crust. Average mid-ocean ridge basalt (MORB) contains ~2.5% Na (McKenzie and Bickle 1988), an enrichment of one order of magnitude over BSE. Most MORB is returned to the mantle via subduction, and may be carried as deep as the lower mantle as part of the subducting oceanic lithosphere (van der Hilst et al. 1997). Holland (1980) defined the *P-T* conditions of the albite ($NaAlSi_3O_8$) ↔ jadeite + quartz reaction over the range 600-1200ºC and 15-35 kbar, showing that albite transforms to jadeite at conditions near the crust-mantle boundary. Gasparik

(1992) calculated the high-*P* and high-*T* stability fields of the jadeite-enstatite ($MgSiO_3$) join, concluding that jadeite is stable up to ~20 GPa at mantle temperatures. These studies constrain the mantle stability field of jadeite from lower crust to ~600 km depth. However, at low concentrations (< 5%), jadeite is a soluble component in other pyroxenes. Thus, while it is unlikely that jadeite is present as a free phase in the mantle, except in localized areas, the properties of the jadeite component of the mantle are still significant.

Pyroxenes dominated by the major mantle metals (i.e., Mg, Fe, Si and Ca) have been the subject of extensive study at high pressures and at high temperatures, as tabulated in Yang and Prewitt (2000). A primary motivation of much of the high-*P* and high-*T* work was to identify phase transitions in these pyroxenes, which, if they occur in the mantle, could result in discontinuities in mantle properties (cf. Gasparik 1989; Duffy et al. 1995; Hugh-Jones et al. 1996).

Less common pyroxenes such as Na-dominated clinopyroxenes have not been studied as much at *P*, although some data exists. In a recent study of the compressibilities of jadeite and aegirine, Nestola et al. (2006a) determined cell parameters as a function of pressure, and examined changes in compressional anisotropy with variations in chemistry along the jadeite-aegerine ($NaFeSi_2O_6$) solid solution. However, no structural data were determined in their study. Zhao et al. (1997) performed a synchrotron X-ray powder diffraction study on jadeite at simultaneous *P* and *T* to 8.2 GPa and 1280 K. They fit their data with a modified Birch-Murnaghan equation of state, with $K_0^{'} \equiv 5.0$, and found the bulk modulus of jadeite to be 125(4) GPa. Cameron et al.

(1973) examined the jadeite structure at four temperatures from ambient to 800ºC. They found that jadeite cell parameters (a, b, c, β) and average M–O distances (Na–O, Al–O) increased linearly with temperature. No significant changes in Si–O bond lengths were observed, although rotation of the SiO_4 tetrahedra, on the order of a few degrees, was found to accommodate some of the expansion of the structure.

The pyroxene structure consists of chains of edge-sharing M1 octahedra and chains of corner-linked Si tetrahedra, both parallel to **c**. Large, irregular M2 polyhedra reside between, and cross-link, the M1 and T chains. It has been suggested that compressibility of *C*2/*c* pyroxenes seems to be controlled, to a first order, by the $M1O_6$ chains. Size of the M1 cation is positively correlated with ambient unit cell volumes (Thompson et al. 2005). The same authors demonstrate that M2 cation size is not correlated with unit cell volume. The tetrahedral chain links are relatively flexible and the chain length can vary along **c** by tetrahedral rotation, associated with change in the O3-O3-O3 angle and Si–Si distances. The tetrahedra themselves compress very little due to the short O–O contacts related to the strong, short Si–O bonds. Average O–O polyhedral edge lengths in jadeite at ambient pressure are as follows: NaO_6, 2.90 Å; AlO_6, 2.72 Å; SiO_4, 2.65 Å. Atoms at M2 in clinopyroxenes reside in a site with irregular coordination that varies from 4- to 8-fold, depending on the structure. The M2–O bonds tend to be long and compressible compared to M1–O bonds. Thus M2 was not thought to have much effect on pyroxene compression. Downs (2003) indicates that the only variation in bonding topology of the pyroxenes involves M2–O3 bonds, where O3 are bridging oxygens in the tetrahedra chains. An examination of *C*2/*c* pyroxenes

indicates that coordination of M2 cations appears to be correlated with the charge of the cation.

Experimental Methods

A natural jadeite crystal from Clear Creek, San Benito County, California, USA, supplied by Hatt Yoder, was selected for study based on crystal quality as determined by examination of peak profiles. A crystal from the same sample was used by Prewitt and Burnham (1966) in their original description of the jadeite structure. Typical peak widths were 0.10º in ω. The size of the crystal was 80 μm × 70 μm × 40 μm. The composition of a jadeite crystal picked from the same hand specimen was determined by an average of 20 microprobe analyses to be $Na_{1.002(8)}Al_{1.000(10)}(Si_{1.979(8)}Al_{0.024})_{\sum 2.003(8)}O_6$. The same piece, numbered R050220, was examined as part of the RRUFF project, and information on these analyses can be found at www.rruff.info.

Diffraction data were collected with an automated Picker four-circle diffractometer using unfiltered MoKα radiation and operating at 45 kV and 40 mA. Before loading in the diamond cell, the crystal was examined in air. The positions of 28 high-intensity peaks ($9º < 2\theta < 33º$) were determined using a modification of the eight-peak centering technique of King and Finger (1979), by fitting both $K\alpha_1$ and $K\alpha_2$ profiles with Gaussian functions. Refined cell parameters constrained to monoclinic symmetry are given in Table 2. A half sphere of intensity data was collected to $2\theta \leq 60º$, using ω scans of 1º width, step size 0.025º, and 5 s per step counting times. The structure was refined on *F* with anisotropic displacement parameters using a modification of RFINE

(Finger and Prince, 1975) to $R_w = 0.027$. Structural data at room conditions are summarized in Table 3. These data have smaller errors than Prewitt and Burnham (1966) ($R = 0.040$), but otherwise compare favorably.

The jadeite crystal was loaded into a four-pin Merrill-Bassett type diamond-anvil cell with beryllium seats. The vector perpendicular to the (110) plane was oriented parallel to the diamond-anvil cell axis. The diamond anvil culet size was 600 μm. A 250 μm thick stainless steel gasket, pre-indented to 120 μm, with a hole diameter of 350 μm, was used. Along with the jadeite crystal, the cell was loaded with a small ruby fragment and a 4:1 mixture of methanol:ethanol as pressure medium. Ruby fluorescence spectra were collected before and after each collection of intensity data, and the positions of the R_1 and R_2 peaks were determined by fitting with Lorentzian functions. Pressure was calculated from the fitted R_1 and R_2 peak positions using the function of Mao et al. (1978), with an estimated error of ±0.05 GPa.

The experiment was carried out to a pressure of 9.17 GPa. The gasket failed when the pressure was raised further. Unit-cell data were collected at 16 pressures, and intensity data were collected at 9 of these pressures.

Every accessible reflection allowed by $C2/c$ symmetry, up to 672 intensity data ($2\theta \leq 60^\circ$), were collected at pressure, with ω scans of 1° width, in steps of 0.025° and counting times of 10 s per step. These data reduced to 214 symmetry-equivalent reflections. Reflections violating $C2/c$ were examined, but none with significant intensities were found throughout the experiment. Absorption corrections for the beryllium seats and diamond anvils were made from an absorption correction profile of

the empty diamond cell. Structure factors were weighted by $\omega = [\sigma_F^2 + (pF)^2]^{-1}$, where σ_F was obtained from counting statistics and p chosen to insure normally distributed errors (Ibers and Hamilton 1974). Structural data were refined with isotropic displacement factors using a modified version of RFINE (Finger and Prince 1975) and are summarized in Table 4. R_w ranged from 0.027 to 0.047.

Bond lengths and angles were calculated using BOND91 software, modified after Finger and Prince (1975). Polyhedral volumes and quadratic elongations were obtained with XTALDRAW (Downs and Hall-Wallace 2003). Selected bond lengths, angles, and polyhedral volumes are presented in Table 5.

Results and Discussion

A third-order Birch-Murnaghan equation was fit to the data in Table 2 to determine a pressure-volume equation of state for jadeite, resulting in V_0 = 402.03(2) Å^3, K_0 = 137(1) GPa, and $K_0^{'}$ = 3.4(4), or V_0 = 402.03(2) Å^3 and K_0 = 134.4(3) GPa with $K_0^{'} \equiv 4.0$. Our values closely match those reported by Nestola et al. (2006a): V_0 = 402.26(2) Å^3, K_0 = 134.0(7) GPa and $K_0^{'}$ = 3.7(6). Brillouin spectroscopy has also been used to determine single-crystal elasticity of jadeite from the same locality, with results (K_0 = 143 GPa) that compare well with those from this study (Kandelin and Weidner 1988). Constraining K_0 to the value derived from Brillouin measurements (143 GPa) results in V_0 = 402.01(2) and $K_0^{'}$ = 1.6(1). Our data and fitted curve are plotted in Figure 1. The compressibility of jadeite, reflected by V/V_0, is compared to other Na

clinopyroxenes in Figure 2. No evidence of a phase transition in jadeite was observed to a pressure of 9.17 GPa. All observed cell parameters decrease continuously with increasing pressure. Cell-parameter data were used to construct unit strain ellipsoids with STRAIN, modified after Ohashi (1982). The unit strain ellipsoid is highly anisotropic, with axial ratios of 1.00:1.63:2.10 in the range 0-9.17 GPa, and is illustrated in Figure 3. The axial values of the unit strain ellipsoid are: ε_1, –0.001391; ε_2, –0.002274; and ε_3, –0.002922 GPa^{-1}. The ε_3 axis is 53.7º from **c**, and in the clinopyroxene structures, ε_2 is constrained to be parallel to **b**, with ε_1 90º from the $\varepsilon_2\varepsilon_3$ plane. Our results compare well with Nestola et al. (2006a) who report unit strain ellipsoid axial ratios of 1.00:1.60:2.10 in the range 0-5.82 GPa.

Procrystal electron density analysis of jadeite indicates six Na–O bonds at room conditions (Downs 2003). Na in jadeite resides on a two-fold symmetry axis, constraining the coordination of Na to an even number, and resulting in three pairs of equivalent Na–O bonds. In this paper equivalent bonds are represented, for example, in the manner Na–$O3_{2,3}$, where Na is bonded to $O3_2$ and $O3_3$, which are symmetrically equivalent atoms. Figure 4B shows the environment around Na in jadeite, which is bonded to two O1, two O2 and the two bridging oxygen atoms $O3_2$ and $O3_3$, following the nomenclature of Downs (2003). The nearest unbonded oxygen atoms are $O3_1$ and $O3_4$, at a distance of 2.741(1) Å from Na at ambient pressure. All Na–O distances in jadeite decrease with pressure, although at different rates (Fig. 5). The Na–$O3_{1,4}$ distance decreases at nearly 10 times the rate of the Na–$O3_{2,3}$ distance, the bond distance displaying the least decrease with pressure. Linear extrapolation of the decreasing Na–

$O3_{2,3}$ and Na–$O3_{1,4}$ distances shows they would be the same length at 22.8 GPa. At this or a lesser pressure, jadeite is expected to undergo a bonding transition as Na forms bonds to $O3_{1,4}$. The longest Na–O bond in jadeite at room conditions is Na–$O3_{2,3}$, at 2.414(1) Å. It may be more reasonable to assume Na–$O3_{1,4}$ bond formation at this Na–O distance rather than the extrapolated, decreasing Na–$O3_{2,3}$ distance. In this case, the linearly extrapolated Na–$O3_{1,4}$ distance reaches 2.414 Å at a pressure of 17.8 GPa.

The Al atom in jadeite resides in the octahedral M1 site. It is 6-coordinated with oxygen at all pressures in this study. Al–O bond lengths decrease systematically with pressure (Fig. 6). The Al octahedron becomes more regular with pressure, with the mean quadratic elongation decreasing from 1.0151 at ambient conditions to 1.0139 at 9.17 GPa.

The ∠O3-O3-O3 in jadeite decreases from 174.7(1)º at ambient conditions to 169.2(6)º at 9.17 GPa (Fig. 7). The decrease is approximately linear with pressure and the slope is similar to that found for kosmochlor ($NaCrSi_2O_6$) (Origlieri et al. 2003). In both minerals, the silicate tetrahedra become more O-rotated with increased pressure. Ideal pyroxenes with perfectly closest-packed oxygen arrays exhibit O3-O3-O3 angles of 120º (cubic) and 240º (hexagonal) (Thompson 1970). Thus the oxygen atoms in jadeite move toward a cubic-closest-packed arrangement with pressure, but they are still far from it at 9.17 GPa. The distortion from a cubic closest-packed arrangement of oxygen atoms is reflected by the mismatch in nearest neighbor O-O distances at the edges of the three types of polyhedral units, as described above.

The M2–O3 distances in Na-clinopyroxenes are positively correlated with unit cell volumes as shown in Figure 8. Structures with the smallest unit cell volumes have

the shortest M2–O3 bonds. Jadeite has the smallest unit cell volume of any Na-pyroxene in this study (Table 1), and thus has the shortest unbonded, nearest-neighbor M2–O3 distance ($Na–O3_{1,4}$ distance of 2.741(1) Å). *C*2/*c* → *C*2/*c* bonding transitions may occur in *C*2/*c* pyroxenes with pressure as M2–O3 bond pairs form or break. In a Raman spectroscopy study of diopside ($CaMgSi_2O_6$), Chopelas and Serghiou (2002) observed discontinuities in Raman spectra as a function of pressure. They attributed this change to *C*2/*c* → *C*2/*c* transitions, with Ca coordination changing from eight to six with increasing pressure. Origlieri et al. (2003) reported incipient M2–O3 bond formation in kosmochlor with pressure, which would represent a *C*2/*c* → *C*2/*c* transition. Still, such a transition has not been observed in a high-pressure X-ray diffraction study. The Na-pyroxene that undergoes a *C*2/*c* → *C*2/*c* transition at lowest pressure is likely to be determined by the (nearest neighbor) unbonded M2–O3 distance and the rate of decrease of this distance with pressure. Jadeite, with its short unbonded M2–O3 distance, is thus a good candidate for the Na-pyroxene with the lowest *C*2/*c* → *C*2/*c* transition pressure. However, our current experiment did not reach the requisite pressure of ~20 GPa.

Thompson and Downs (2003) suggested that M2–T repulsion may influence distortion of pyroxene structures with pressure, specifically silicate chain bending. The M2–T distances are the shortest cation-cation distances in the jadeite structure, and decrease with pressure. Based on this short distance, the strongest cation-cation Coulomb repulsion in the jadeite structure is between the cation at M2 and the nearest Si atom (Table 6). As jadeite is compressed, the $Na–O3_{1,4}$ distance decreases dramatically (as

mentioned, Fig. 5). However, the repulsion between Na and the nearest Si atom (2.985(1) Å away at ambient conditions) resists shortening of the M2–T distance.

Compressibility Systematics of C2/c and $P2_1/c$ Pyroxenes

One goal in the study of pyroxenes is to find a model that will provide a prediction of bulk moduli. Thompson and Downs (2005) developed a model that could predict *C*2/*c* pyroxene unit cell volumes at *P* and *T*. Their model was based on the chemistry of the pyroxene and used empirically determined polyhedral expansion and contraction coefficients. Their study showed that unit cell volume is largely a function of M1, and the bulk modulus of *C*2/*c* pyroxenes depends primarily on the occupancy of the M1 site.

Another approach to predicting bulk moduli is based on the observation, first made by Bridgman (1923), of the empirical relationship between bulk moduli and molar volumes of isostructural materials. Bridgman's ideas have been successfully applied by Anderson and others to a variety of minerals (cf. Anderson and Anderson 1970; Anderson 1972), as tabulated in Hazen and Finger (1982). "Bridgman's Law" implies that, for isostructural materials, cell volumes at ambient conditions are inversely correlated with the bulk modulus. "Bridgman's Law" seems to hold when the compressibility of a mineral is controlled by: 1) shortening of cation-anion bonds as in simple oxides and halides, and/or 2) angle bending, which occurs in more topologically complex minerals such as pyroxenes, feldspars, and silica polymorphs. Angle bending behavior is sometimes modified by bonds to bridging anions. Downs et al. (1999)

examined the compressibilities of various feldspars and found them to be controlled by: 1) the stiffness of T-O-T angles—which varies depending on the identity of the tetrahedral cations (e.g. Si^{4+}, Al^{3+}, B^{3+})—and 2) the number and strength of bonds between the M cations and the oxygen atoms. Although the Al-O-Si angles found in common feldspars are roughly twice as soft as Si-O-Si angles, feldspars are generally stiffer than low-density SiO_2 polymorphs, illustrating the role of metal bonds to bridging oxygens in stiffening the feldspar structures. Among feldspars with the relatively soft Al-O-Si angles, Downs et al. (1999) proposed that microcline had a higher bulk modulus than low albite due to stiffening of the T-O-T angle by additional M–O bonds to the bridging oxygen atoms. This is an example of an exception to "Bridgman's Law" since albite has a smaller unit cell volume and thus was expected to be stiffer. Generally, then, where exceptions to "Bridgman's Law" are observed among nearly isostructural materials, factors that modify simple bond compression and bending behavior are likely to be present.

To explore the application of "Bridgman's Law" to the clinopyroxenes, we tabulated data from high-pressure X-ray diffraction studies in the literature (Table 1). Figure 9A is a plot of bulk moduli versus ambient unit cell volumes for *C*2/*c* and $P2_1/c$ pyroxenes which have been examined at high pressures. In order to create an internally consistent set of pyroxene bulk moduli, published *P*-*V* data for each pyroxene were fit with a third-order Birch-Murnaghan equation of state with $K_0^{'}$ fixed at 4.0. Nestola et al. (2005) argued that fixing $K_0^{'} \equiv 4.0$ may be unreasonable because of the observed large range in $K_0^{'}$ values for pyroxenes. However, $K_0^{'}$ is so dependent on quality and number

of the cell parameter data, it is likely that the unconstrained $K_0^{'}$ values from the tabulated dataset are unreasonable. Furthermore, we found the average unconstrained $K_0^{'}$ value for *C*2/*c* pyroxenes in this study to be 3.5, with a standard deviation of 2.7.

Data presented in Figure 9A show a broad vertical dispersion in K_0 of about 40 GPa with K_0 varying inversely with cell volume. The vertical dispersion can be eliminated by observing that there are two trends that diverge with increasing pressure. These trends have been illustrated by fitted lines. On first inspection, the upper trend appears to be populated by *C*2/*c* pyroxenes and the lower trend by $P2_1/c$ pyroxenes. However, two $ZnSiO_3$ *C*2/*c* polymorphs are exceptions, and appear to be associated with the lower trend. Based on their unit cell volumes, the HT *C*2/*c* and HP *C*2/*c* $ZnSiO_3$ pyroxenes have bulk moduli much lower than expected if the upper trend were to represent *C*2/*c* polymorphs. Linear fits to the upper and lower trends in the pyroxene data result in R^2 values of 0.83 and 0.91, respectively.

There is another way to distinguish these two trends, not based on symmetry, but based on bonding topology. The only significant topological difference in bonding among pyroxenes involves M2–O3 bonding, as discussed by Downs (2003). M2–O3 bonds display one of two behaviors as pyroxene structures are compressed and SiO_4 tetrahedra rotate, changing the O3-O3-O3 angles and decreasing M2–O3 distances. M2–O3 *bonds* whose length decreases are inhibited by pressure-induced tetrahedral rotation tend to resist the rotation, and are thus termed “antipathetic” bonds. In contrast, M2–O3 *bonds* that are further shortened by tetrahedral rotation would either assist or have no effect on tetrahedral rotation, and are thus termed “sympathetic” bonds. Both types are

illustrated in Figure 4. In the *C*2/*c* pyroxenes of the upper trend of Figure 9A, the M2–$O3_{1,4}$ bonds, where present, are sympathetic and the M2–$O_{2,3}$ bonds are antipathetic. This is illustrated in Figure 5, which shows the change in Na–O distances in jadeite as a function of pressure. The antipathetic Na–$O3_{2,3}$ bonds decrease in length much more slowly than the other Na–O bonds, since tetrahedral rotation provides a component of $O3_{2,3}$ displacement away from Na. The Na–$O_{2,3}$ distance has the smallest decrease with pressure while the Na–$O3_{1,4}$ distance has the greatest decrease. This can be interpreted as coupling of the isotropic compression of the structure (shortening all interatomic distances) and the rotation of the silicate tetrahedra (working to shorten some interatomic distances and lengthen others). Thus *all* the structures in the upper trend are not only *C*2/*c*, but they have two (topologically identical) antipathetic M2–O3 bonds, adding a resistive component to compression.

In contrast, all the structures in the lower trend, regardless of symmetry, have only sympathetic M2–O3 bonds, or none at all. In particular, the HT *C*2/*c* $ZnSiO_3$ has no M2–O3 bonds, while the HP *C*2/*c* $ZnSiO_3$ structure has sympathetic M2–$O3_{1,4}$ bonds. Thus, the pyroxenes of the lower trend, displaying greater compressibility than the others, can be interpreted as the pyroxenes without antipathetic M2–O3 bonds. The lack of these bonds removes a component resistive to compression. Figure 4 shows three different pyroxene topologies with arrows indicating the approximate component of displacement of O3 atoms contributed by the tetrahedral rotation with compression.

It is worth noting that not all pyroxenes in the upper trend in Figure 9A have identical bonding topologies. Rather, there are two groups: 1) the monovalent-M2 *C*2/*c*

pyroxenes, $LiAlSi_2O_6$, $NaAlSi_2O_6$, $NaCrSi_2O_6$ and $NaFeSi_2O_6$, where M2 is 6-coordinated and bonded to two bridging oxygens, $O3_2$ and $O3_3$ (Fig. 4A); and 2) the Ca pyroxenes, $CaMgSi_2O_6$, $CaNiSi_2O_6$ and $CaFeSi_2O_6$, where Ca is 8-coordinated and bonded to all bridging oxygens, $O3_1$, $O3_2$, $O3_3$ and $O3_4$ (Fig. 4B). Therefore, the upper trend in Figure 9A provides evidence that antipathetic M2–O3 bonds affect compressibility while sympathetic M2–O3 bonds do not. The monovalent-M2 *C*2/*c* pyroxenes (left side of Figure 9A) all contain two antipathetic M2–O3 bonds but no sympathetic ones. In contrast, the Ca-clinopyroxenes have two antipathetic and two sympathetic M2–O3 bonds. Still, these pyroxenes lie on-trend with the monovalent-M2 pyroxenes. If sympathetic bonds increased compressibility, the Ca-pyroxenes would be expected to lie on their own trend and to have lower bulk moduli than the monovalent-M2 *C*2/*c* pyroxenes.

P2_1/*c* pyroxene topologies vary slightly. They lack the 2-fold axis through M2 and thus this site is not constrained to an even number of bonds with O3 atoms. *P*2_1/*c* $LiFeSi_2O_6$, $LiScSi_2O_6$ and spodumene ($LiAlSi_2O_6$) all have identical M2 bonding topology at minimum stability pressures, with M2 bonded to one bridging oxygen, $O3_2$, illustrated in Figure 4A. Over the pressure range 3.34-8.8 GPa, spodumene gains an M2–$O3_4$ bond (Downs 2003), making M2 6-coordinated, which gives it the same bonding topology as *P*2_1/*c* $ZnSiO_3$, illustrated in Figure 10.

Arlt and Angel (2000) examined the structure of $ZnSiO_3$ at pressures from ambient to 5.05 GPa and discovered two phase transitions over this pressure range. $ZnSiO_3$ is stable in space group HT *C*2/*c* at room conditions, transforms to *P*2_1/*c* at 1.92

GPa, and to HP *C*2/*c* at ~4.9 GPa (Arlt and Angel 2000). It turns out that the behavior of the $ZnSiO_3$ polymorphs provides another confirmation of the sympathetic/antipathetic bond hypothesis. Figure 10 illustrates the three known $ZnSiO_3$ pyroxene structures. HT *C*2/*c* $ZnSiO_3$ has no M2–O3 bonds. Thus this pyroxene exhibits a different topology than all other divalent-M2 *C*2/*c* pyroxenes, which have topologies similar to diopside. The lack of antipathetic M2–O3 bonds appears to allow relatively unrestricted tetrahedral rotation and makes the structure the most compressible of any known *C*2/*c* silicate pyroxene. The *P*2_1/*c* $ZnSiO_3$ exhibits two M2–O3 bonds (to $O3_2$ and $O3_4$; see Figure 10). Both bonds are sympathetic to tetrahedral rotation; thus this structure is softer than *C*2/*c* pyroxenes and falls on the lower trend in Figure 9A. The HP *C*2/*c* $ZnSiO_3$ exhibits two M2–O3 bonds (to $O3_1$ and $O3_4$); both are sympathetic.

The fact that HP *C*2/*c* $ZnSiO_3$ is less compressible than HT *C*2/*c* $ZnSiO_3$ provides further evidence that sympathetic M2–O3 bonds do not make pyroxene structures more compressible; rather, it appears that the important effect is that antipathetic M2–O3 bonds stiffen the structures. HP *C*2/*c* $ZnSiO_3$ appears to be stiffer than the HT *C*2/*c* polymorph due to a smaller (fitted) ambient unit cell.

An examination of the *P*/ V/V_o plot for various clinopyroxenes (Fig. 2) also shows two distinct trends. The structures of the upper trend, which include jadeite, kosmochlor, aegirine and *C*2/*c* spodumene, contain antipathetic bonds. The structures of the lower trend do not contain antipathetic bonds. Therefore, the origin of these two trends is completely explained by our model of sympathetic and antipathetic bonding.

According to Thompson et al. (2005), compressibility of *C*2/*c* pyroxenes is controlled largely by the rigid chains of edge-sharing $M1O_6$ octahedra parallel to the c-axis. It seems that these chains of octahedra should resist compression because the relatively high charge of M1 cations (2+ or 3+), coupled with the short M1–M1 distance, results in strong electrostatic repulsion. However, examination of the unit strain ellipsoid for jadeite show the most compressible direction is only ~54º from the axis of the $M1O_6$ chains ($\parallel$ **c**). In contrast, the chains of silicate tetrahedra offer minor resistance to compression because the tetrahedra can easily rotate, as demonstrated by the decreasing the O3-O3-O3 angle. Figure 7 illustrates the decrease of the O3-O3-O3 angle with pressure in jadeite and kosmochlor, the only two end-member Na clinopyroxenes that have been subjected to high-pressure X-ray diffraction structural studies.

In *C*2/*c* pyroxenes, all M2–O3 distances decrease with pressure due to the decrease of all dimensions of the unit cell. To discern M2–O3 bond length changes not related solely to changes in the shape and size of the unit cell, we generated structures using the ambient atomic positions and the unit cell parameters at each pressure at which we collected structural data. These model structures give an indication of how bond lengths would change with scaling of the unit cell but no other relative atomic translations. This approach is comparable to normalizing bond lengths to the unit cell volume. By normalizing measured bond lengths to the bond lengths from the equivalent model structure, we can identify bond lengths that change in an unusual manner (not caused by simple cell scaling) in the real structure. Our results from jadeite and diopside are plotted in Figure 11. We observe that M2–O3 distances (bonded or unbonded) which

exhibit sympathetic behavior decrease at a greater rate with pressure than expected, based on the scaled-cell model. Antipathetic M2–O3 bonds tend to become slightly longer than their model equivalents with pressure. This occurs because, with pressure, M2 moves toward the tetrahedral chains, but the antipathetically bonded O3 atoms move away from M2 as the tetrahedral chains kink. On the contrary, sympathetically bonded O3 atoms move toward M2 with tetrahedral chain kinking. This is, after all, what gives the bonds their sympathetic or antipathetic character.

We predict that the bulk moduli of silicate clinopyroxenes with antipathetic M2–O3 bonds should follow K_0 (GPa) = $-0.5051V_0$ (Å^3) + 339.37 (linear fit to upper trend in Fig. 9A), whereas silicate clinopyroxenes without antipathetic M2–O3 bonds should follow K_0 (GPa) = $-0.7784V_0$ (Å^3) + 419.14 (linear fit to lower trend in Fig. 9A). Table 7 lists predicted bulk moduli for $C2/c$ and $P2_1/c$ silicate pyroxene structures based on these equations. Structural data from high pressures is not available for many of the structures considered; therefore the antipathetic versus sympathetic nature of the M2–O3 bonds cannot be known with certainty for these structures. However, the nature of these bonds can be estimated based on the similarity of each structure with structures known to either contain antipathetic bonds (e.g. jadeite, diopside) or to contain none (e.g. $P2_1/c$ spodumene, HP $C2/c$ $ZnSiO_3$). If new high-pressure structural data becomes available for any of these materials, the nature of the M2–O3 bonds can be identified and the predicted bulk modulus can be calculated based on the appropriate equation.

Where high-pressure data is not available, data at multiple temperatures may elucidate the sympathetic/antipathetic nature of M2–O3 bonds in pyroxene structures.

Decreasing temperature can be analogous to increasing pressure in terms of the effect on a crystal structure of pyroxene (Hazen and Finger 1982), and increasing temperature should have the opposite effect. We suggest that the expansivities of pyroxene structures with temperature may show a dichotomy similar to that displayed by the compressibilities. Structures exhibiting only sympathetic bonds under compression would be expected to have the lower expansivities because these bonds would become resistive to the now-reversed tetrahedral rotations. However, pyroxene structures, even at temperatures approaching the melting point of the material (i.e., ~1000ºC), show a small amount of expansion compared to the compression observed with pressures up to ~10 GPa. For example, in the classic study of the structures of several pyroxenes at high temperatures by Cameron et al. (1973), the expansion of the jadeite structure from ambient temperature to 800ºC shows an increase in the unit cell volume of only 1.9%. In contrast, the unit cell volume contracts by 5.9% with increased pressure over the range 0-9.17 GPa as shown in this study. Therefore, if it is even possible to elucidate antipathetic versus sympathetic bond behavior using temperature data, the data will need to be of the highest quality.

Orthopyroxene Compressibility

If antipathetic M2–O3 bonds resist silicate tetrahedra rotation and thus compression of clinopyroxene structures, it seems reasonable to expect a similar phenomenon in orthopyroxenes, which exhibit a similar set of M2–O3 topologies. Unfortunately, few orthopyroxenes have been subjected to high-pressure single-crystal

X-ray diffraction studies to determine bulk moduli (Yang and Prewitt 2000). No clear trends are observed in the available data (Fig. 9B), except that "Bridgman's Law" appears to hold for orthopyroxenes as well.

Acknowledgments

We would like to thank the National Science Foundation for funding our study, Compression Mechanisms of Upper Mantle Minerals, through grant No. EAR-9903104. The manuscript benefited greatly from comments by Dmitry L. Lakshtanov and an anonymous reviewer. The authors are also grateful to the late Hatt Yoder, who provided the jadeite sample used in this study.

References

Anderson, D.L. and Anderson, O.L. (1970) The bulk modulus-volume relationship for oxides. Journal of Geophysical Research, 75, 3494–3500.

Anderson, O.L. (1972) Patterns in elastic constants of minerals important to geophysics. In: Nature of the Solid Earth, Robinson E.C. (ed) McGraw-Hill, New York, p 575–613.

Arlt, T. and Angel, R.J. (2000) Displacive phase transitions in *C*-centred clinopyroxenes: spodumene, $LiScSi_2O_6$ and $ZnSiO_3$. Physics and Chemistry of Minerals, 27, 719–731.

Arlt T., Angel R.J., Miletich R., Armbruster T., and Peters T. (1998) High pressure $P2_1/c$-$C2/c$ phase transitions in clinopyroxenes: Influence of cation size and electronic

structure. American Mineralogist, 83, 1176–1181.

Bindi, L., Downs, R.T., Harlow, G.E., Safonov, O.G., Litvin, Y.A., Perchuck, L.L., Uchida, H., and Menchetti, S. (2006) Compressibility of synthetic potassium-rich clinopyroxene: In-situ high-pressure single-crystal X-ray study. American Mineralogist, 91, 802–808.

Bridgman P.W. (1923) The compressibility of thirty metals as a function of pressure and temperature. Proceedings of the American Academy of Arts and Sciences, 58, 165–242.

Cameron, M., Sueno, S., Prewitt, C.T., and Papike, J.J. (1973) High-temperature crystal chemistry of acmite, diopside, hedenbergite, jadeite, spodumene and ureyite. American Mineralogist, 58, 594–618.

Chopelas, A. and Serghiou, G. (2002) Spectroscopic evidence for pressure-induced phase transitions in diopside. Physics and Chemistry of Minerals, 29, 403–408.

Downs, R.T. (2003) Topology of the pyroxenes as a function of temperature, pressure and composition determined from the procrystal electron density. American Mineralogist, 88, 556–566.

Downs, R.T. and Hall-Wallace, M. (2003) The American Mineralogist crystal structure database. American Mineralogist, 88, 247–250.

Downs, R.T. and Singh, A.K. (2006) Analysis of deviatoric stress from nonhydrostatic pressure on a single crystal in a diamond anvil cell: The case of monoclinic aegirine, $NaFeSi_2O_6$. Journal of Physics and Chemistry of Solids, 67, 1995–2000.

Downs, R.T., Yang, H., Hazen, R.M., Finger, L.W., and Prewitt, C.T. (1999)

Compressibility mechanisms of alkali feldspars: New data from reedmergnerite. American Mineralogist, 84, 333–340.

Duffy, T.S., Zha, C.S., Downs, R.T., Mao, H.K., and Hemley, R.J. (1995) Elasticity of forsterite to 16 GPa and the composition of the upper mantle. Nature, 378, 170-173.

Finger, L.W. and Prince, E. (1975) A system of Fortran IV computer programs for crystal structure computations. US Bureau of National Standards Technical Note 854, 128 pp.

Freed, R.L. and Peacor D.R. (1967) Refinement of the crystal structure of johannsenite. American Mineralogist, 52, 709–720.

Gasparik, T. (1989) Transformation of enstatite-diopside-jadeite pyroxenes to garnet. Contributions to Mineralogy and Petrology, 102, 389–405.

Gasparik, T. (1992) Enstatite-jadeite join and its role in the Earth's mantle. Contributions to Mineralogy and Petrology, 111, 283–298.

Gatta, G.D., Ballaran, T.B., and Iezzi, G. (2005) High-pressure X-ray and Raman study of a ferrian magnesian spodumene. Physics and Chemistry of Minerals, 32, 132–139.

Ghose, S., Wan, C., and Okamura, F.P. (1987) Crystal structures of $CaNiSi_2O_6$ and $CaCoSi_2O_6$ and some crystal-chemical relations in *C*2/*c* pyroxenes. American Mineralogist, 72, 375–381.

Hattori, T., Nagai, T., Yamanaka, T., Werner, S., and Schulz, H. (2000) Single-crystal X-ray diffraction of $FeGeO_3$ high-P clinopyroxene (*C*2/*c*) up to 8.2 GPa. American Mineralogist, 85, 1485–1491.

Hazen, R.M. and Finger, L.W. (1982) Comparative Crystal Chemistry: Temperature,

Pressure, Composition and the Variation of Crystal Structure. 231 p. John Wiley & Sons, New York, New York, USA.

Holland, T.J.B. (1980) Reaction albite = jadeite + quartz determined experimentally in the range 600-1200ºC. American Mineralogist, 65, 129–134.

Hugh-Jones, D.A. and Angel, R.J. (1994) A compressional study of $MgSiO_3$ orthoenstatite to 8.5 GPa. American Mineralogist, 79, 405–410.

Hugh-Jones, D., Sharp T., Angel, R., and Woodland, A. (1996) The transition of orthoferrosilite to high-pressure *C*2/*c* clinoferrosilite at ambient temperature. European Journal of Mineralogy, 8, 1337–1345.

Hugh-Jones, D.A., Chopelas, A., and Angel, R.J. (1997) Tetrahedral compression in $(Mg,Fe)SiO_3$ orthopyroxenes. Physics and Chemistry of Minerals, 24, 301–310.

Ibers, J.A. and Hamilton, W.C., Eds. (1974) International Tables for X-ray Crystallography, Vol IV, 366 p. Kynoch Press, Birmingham, U.K.

Kandelin, J. and Weidner, D.J. (1988) The single-crystal elastic properties of jadeite. Physics of the Earth and Planetary Interiors, 50, 251-260.

King, H.E. Jr. and Finger, L.W. (1979) Diffracted beam crystal centering and its application to high-pressure crystallography. Journal of Applied Crystallography, 12, 374–378.

Kopnin, E.M., Sato, A., and Muromachi, E.T. (2003) High pressure synthesis and structure refinement of $LiTiSi_2O_6$. Journal of Alloys and Compounds, 354, L16–L19.

Levien, L. and Prewitt, C.T. (1981) High-pressure structural study of diopside. American

Mineralogist, 66, 315–323.

Mao, H.K., Bell, P.M., Shaner, J.W., and Steinberg, D.J. (1978) Specific volume measurements of Cu, Mo, Pd, and Ag and calibration of the ruby R1 fluorescence pressure gauge from 0.06 to 1 Mbar. Journal of Applied Physics, 49, 3276–3283.

McDonough, W.F. and Sun, S.S. (1995) The composition of the Earth. Chemical Geology, 120, 223–253.

McKenzie, D. and Bickle, M.J. (1988) The volume and composition of melt generated by extension of the lithosphere. Journal of Petrology, 29, 625–679.

Nestola, F., Ballaran, T.B., Tribaudino, M., and Ohashi, H. (2005) Compressional behaviour of $CaNiSi_2O_6$ clinopyroxene: bulk modulus systematic and cation type in clinopyroxenes. Physics and Chemistry of Minerals, 32, 222–227.

Nestola, F., Ballaran, T.B., Liebske, C., Bruno, M., and Tribaudino, M. (2006a) High-pressure behaviour along the jadeite $NaAlSi_2O_6$-aegerine $NaFeSi_2O_6$ solid solution up to 10 GPa. Physics and Chemistry of Minerals, 33, 222–227.

Nestola F., Gatta G.D., and Ballaran T.B. (2006b) The effect of Ca substitution on the elastic and structural behavior of orthoenstatite. American Mineralogist, 91, 809–815.

Ohashi, Y. (1982) A program to calculate the strain tensor from two sets of unit-cell parameters. In: Hazen, R.M. and Finger, L.W. (eds) Comparative crystal chemistry. John Wiley & Sons, New York, New York, 231 pp.

Ohashi, H., Fujita, T., and Osawa, T. (1982) Crystal structure of sodium titanium silicate ($NaTiSi_2O_6$) pyroxene. Journal of the Japanese Association of Mineralogy, Petrology and Economic Geology, 77, 305–309.

Ohashi H., Osawa T., and Tsukimura K. (1987) Refinement of the structure of manganese sodium dimetasilicate. Acta Crystallographica, C43, 605–607.

Ohashi, H., Osawa, T., and Sato, A. (1990) Structures of $Na(In,Sc)Si_2O_6$ clinopyroxenes formed at 6 GPa pressure. Acta Crystallographica, B50, 838–840.

-- -- -- . (1994a) $NaScSi_2O_6$. Acta Crystallographica, B46, 742–747.

-- -- -- . (1994b) $NaVSi_2O_6$. Acta Crystallographica, C50, 1652–1655.

-- -- -- . (1995) Low-density form of $NaGaSi_2O_6$. Acta Crystallographica, C51, 2476–2477.

Origlieri, M.J., Downs, R.T., Thompson, R.M., Pommier, C.J.S., Denton, M.B., and Harlow, G.E. (2003) High-pressure crystal structure of kosmochlor, $NaCrSi_2O_6$, and systematics of anisotropic compression in pyroxenes. American Mineralogist, 88, 1025–1032.

Pommier, C.J.S., Downs, R.T., Stimpfl, M., Redhammer, G.J., and Denton, M.B. (2005) Raman and X-ray investigations of $LiFeSi_2O_6$ pyroxene under pressure. Journal of Raman Spectroscopy 36, 864–871.

Prewitt, C.T. and Burnham, C.W. (1966) The crystal structure of jadeite, $NaAlSi_2O_6$. American Mineralogist, 51, 956–975.

Redhammer, G.J., Amthauer, G., Lottermoser, W., and Treutmann, W. (2000) Synthesis and structural properties of clinopyroxenes of the hedenbergite $CaFeSi_2O_6$ - aegirine $NaFeSi_2O_6$ solid-solution series. European Journal of Mineralogy, 12, 105–120.

Redhammer, G.J., and Roth, G. (2004) Structural variation and crystal chemistry of $LiMe^{3+}Si_2O_6$ clinopyroxenes, Me^{3+} = Al, Ga, Cr, V, Fe, Sc and In. Zeitschrift fur

Kristallographie, 219, 278–294.

Redhammer, G.J., Ohashi, H., and Roth, G. (2003) Single-crystal structure refinement of $NaTiSi_2O_6$ clinopyroxene at low temperatures ($298 < T < 100$ K). Acta Crystallographica, B59, 730–746.

Sato, A., Osawa, T., and Ohashi, H. (1994) $LiGaSi_2O_6$. Acta Crystallographica, C50, 487-488.

Thompson, J.B. (1970) Geometric possibilities for amphibole structures: model biopyriboles. American Mineralogist, 55, 292–293.

Thompson, R.M. and Downs, R.T. (2003) Model pyroxenes I: Ideal pyroxene topologies. American Mineralogist, 88, 653–666.

Thompson, R.M. and Downs, R.T. (2004) Model pyroxenes II: Structural variation as a function of tetrahedral rotation. American Mineralogist, 89, 614–628.

Thompson, R.M., Downs, R.T., and Redhammer, G.J. (2005) Model pyroxenes III: Volume of *C*2/*c* pyroxenes at mantle *P*, *T*, and *x*. American Mineralogist, 90, 1840–1851.

Tribaudino, M., Prencipe, M., Bruno, M., and Levy, D. (2000) High-pressure behaviour of Ca-rich *C*2/*c* clinopyroxenes along the join diopside-enstatite ($CaMgSi_2O_6$-$Mg_2Si_2O_6$). Physics and Chemistry of Minerals, 27, 656–664.

van der Hilst, R.D., Widiyantoro, S., and Engdahl, E.R. (1997) Evidence for deep mantle circulation from global tomography. Nature, 386, 578–584.

Woodland, A.B. (1998) The orthorhombic to high-*P* monoclinic phase transition in Mg-Fe pyroxenes: Can it produce a seismic discontinuity? Geophysical Research Letters,

25, 1241–1244.

Yang, H., Finger, L.W., Pamela, C.G., Prewitt, C.T., and Hazen, R.T. (1999) A new pyroxene structure at high pressure: Single-crystal X-ray and Raman study of the *Pbcn-P2$_1$cn* phase transition in protopyroxene. American Mineralogist, 84, 245–256.

Yang, H. and Prewitt, C.T. (2000) Chain and layer silicates at high temperatures and pressures. Reviews in Mineralogy and Geochemistry, 41, High-Temperature and High-Pressure Crystal Chemistry, Robert M. Hazen and Robert T. Downs, Editors. Mineralogical Society of America, Washington D.C.

Zhang, L., Ahsbahs, H., Hafner, S.S., and Kutoglu, A. (1997) Single-crystal compression and crystal structure of clinopyroxene up to 10 GPa. American Mineralogist, 82, 245–258.

Zhao Y.S., VonDreele R.B., Shankland T.J., Weidner D.J., Zhang J.Z., Wang Y.B., and Gasparik T. (1997) Thermoelastic equation of state of jadeite $NaAlSi_2O_6$: An energy-dispersive Reitveld refinement study of low symmetry and multiple phases diffraction. Geophysical Research Letters, 24, 5–8.

Figure 1. Unit cell volume as a function of pressure for jadeite. Data are fit with a third-order Birch-Murnaghan equation, with V_0 = 402.03(2) Å^3, K_0 = 137(1) GPa, and $K_0^{'}$ = 3.4(4). Errors in *P* and *V* are significantly smaller than the symbols used.

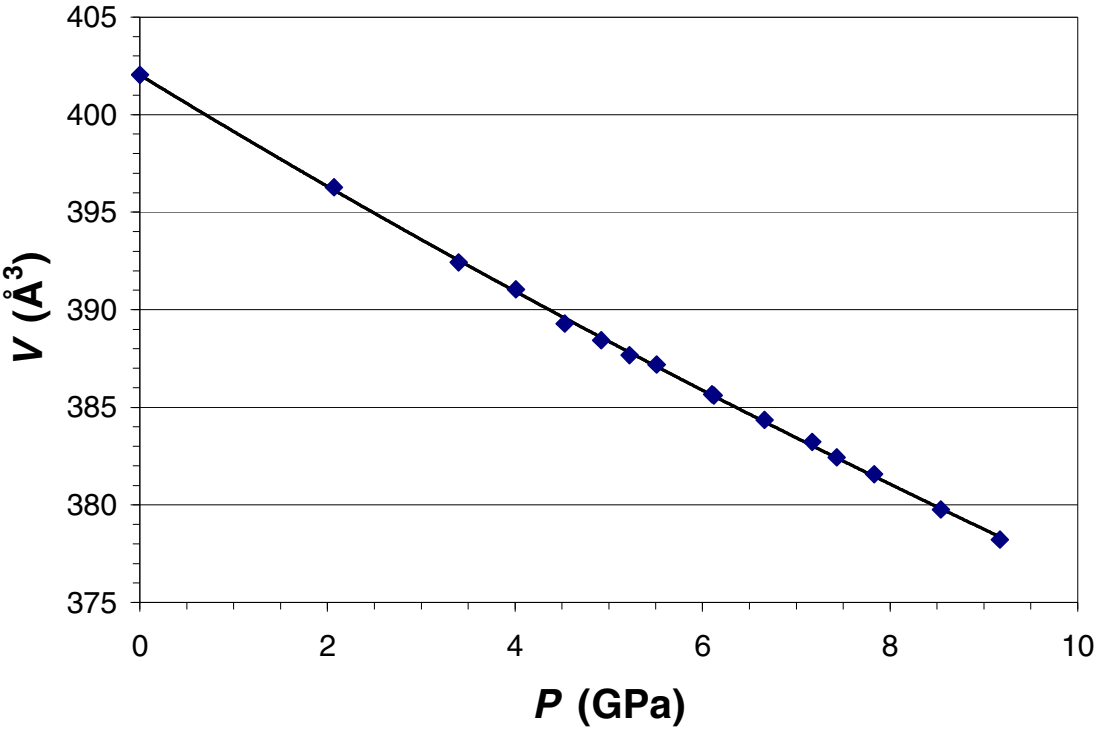

Figure 2. Normalized unit-cell volumes versus pressure for jadeite, and for a selection of $C2/c$ and $P2_1/c$ pyroxenes from the literature. The jadeite unit cell volume decreases less than that of other clinopyroxenes over the P range examined. Errors in P and V are significantly smaller than the symbols used.

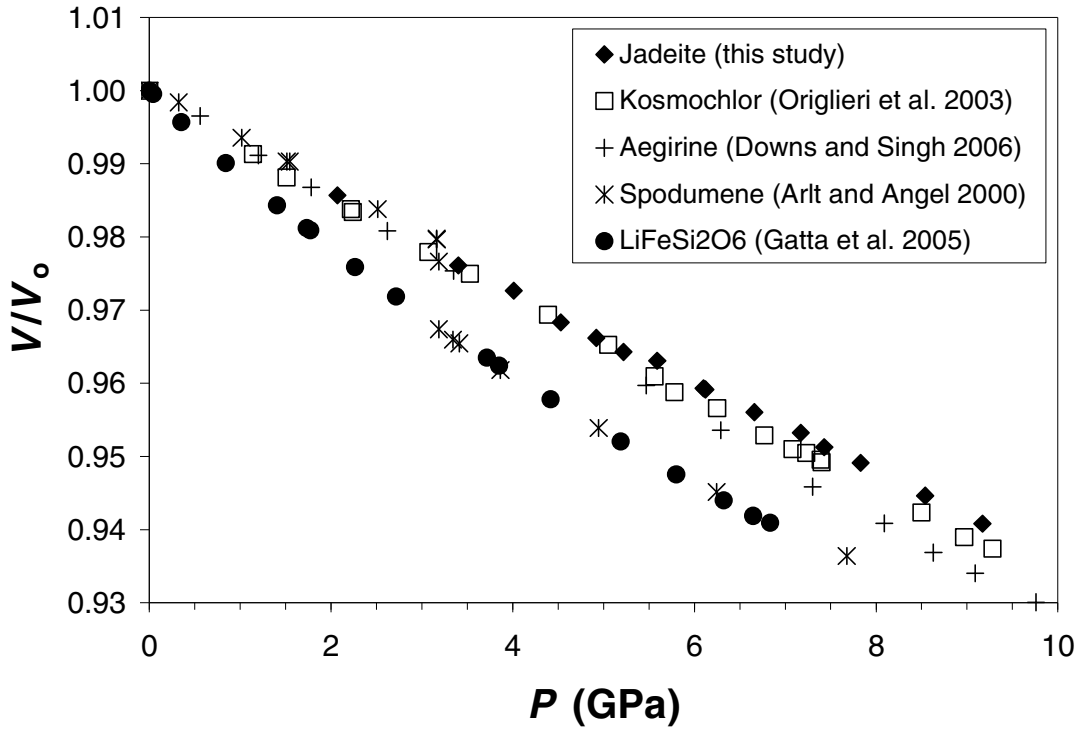

Figure 3. Oriented unit strain ellipsoid superimposed on the jadeite structure viewed down **b**. M2 (Na) is illustrated as a sphere. Although edge-sharing $M1O_6$ polyhedral chains are thought to control compressibility of pyroxene structures, the most compressible direction in jadeite is only ~54º from **c**.

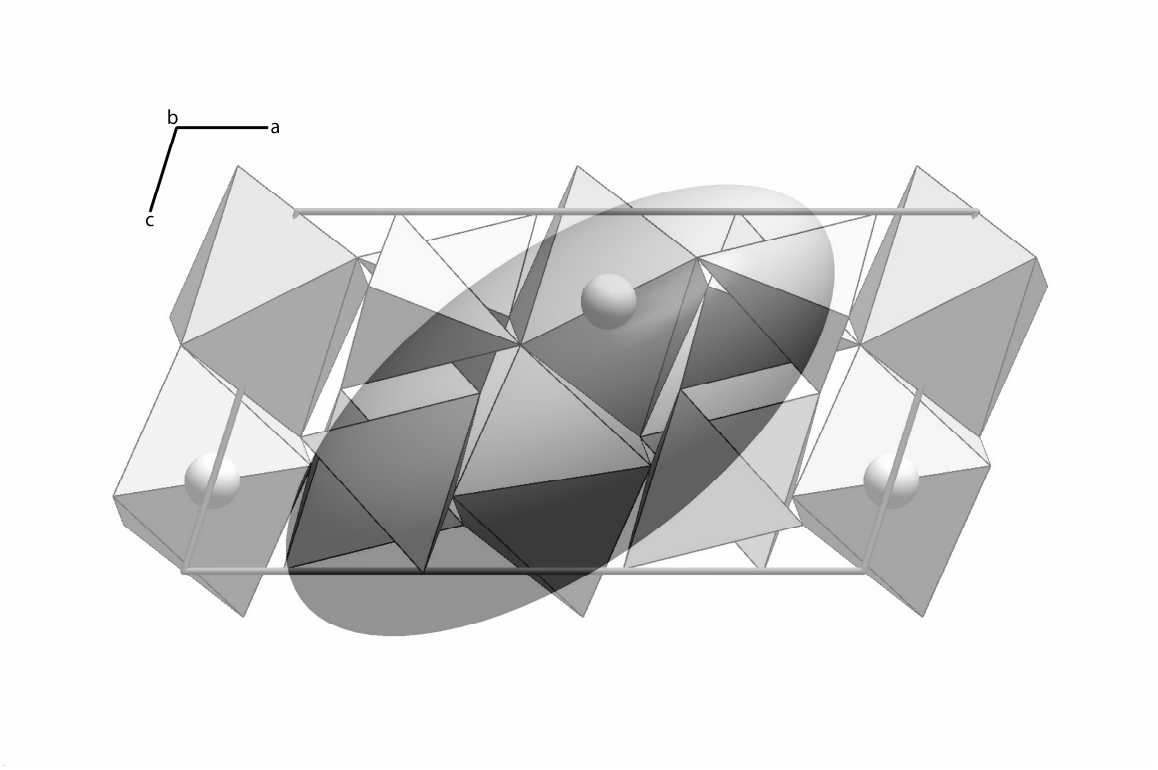

Figure 4. Various M2–O bonding topologies exhibited by the clinopyroxene structures examined in this study. View is down **a***. The solid lines connect the center of bridging (O3) oxygens, which are labeled following the nomenclature of Downs (2003). The arrows represent schematically the displacement direction of the O3 atoms, relative to the unit cell, as pressure increases. Although all interatomic distances in jadeite decrease with pressure, distances associated with sympathetic M2–O3 movement decrease more with pressure than suggested by a purely compressional model. (A) M2–O bonding in $P2_1/c$ spodumene, which is characteristic of all the Li-$P2_1/c$ pyroxenes in this study. M2 has one sympathetic bond with O3, and no antipathetic bonds, making the structure more compressible than jadeite- or diopside-type structures. (B) M2–O bonding in jadeite, which is characteristic of all the $M2^{1+}$ $C2/c$ pyroxenes in this study. M2 has two antipathetic bonds to O3, which makes this structure stiff compared to topologies lacking antipathetic bonds. (C) M2–O bonding in diopside, which is characteristic of all the Ca-$C2/c$ pyroxenes in this study. M2 has two antipathetic and two sympathetic M2–O3 bonds. Structures with this bonding topology lay on-trend with jadeite-type structures in Figure 9A, providing evidence that sympathetic M2–O3 bonds do not affect compressibilities.

Fig. 4 cont.

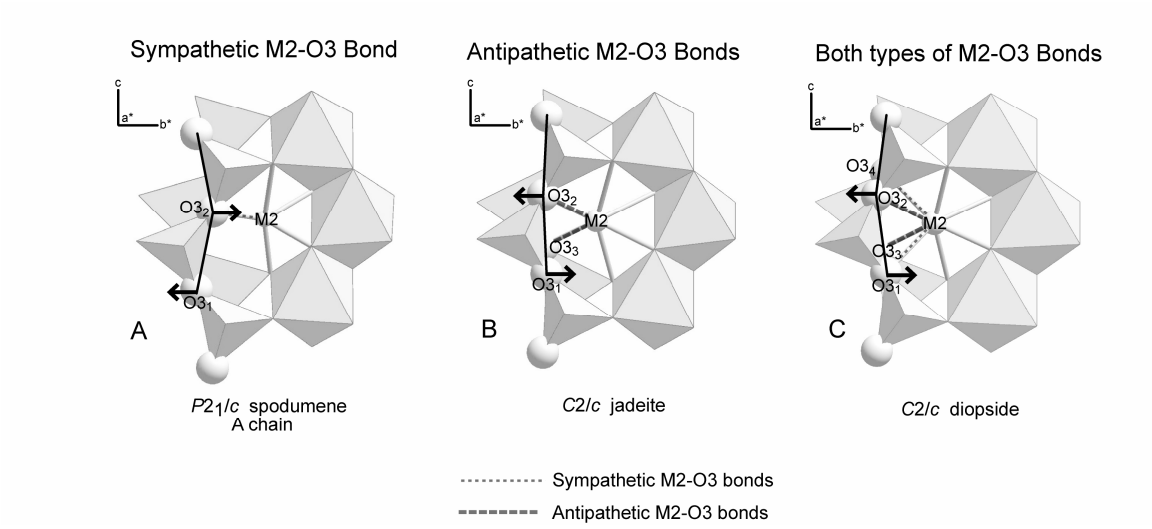
Sympathetic M2-O3 Bond
Antipathetic M2-O3 Bonds
Both types of M2-O3 Bonds
c
a*
b*
O3₂
M2
O3₁
A
O3₂
M2
O3₃
O3₁
B
O3₄
O3₂
M2
O3₃
O3₁
C
P2₁/c spodumene
A chain
C2/c jadeite
C2/c diopside
Sympathetic M2-O3 bonds
Antipathetic M2-O3 bonds

Figure 5. Variation of Na–O distances in jadeite with pressure at room temperature. Na–$O3_{1,4}$ is the only unbonded pair over the pressure range examined in this study. At a pressure of 17.8 GPa, the linearly extrapolated Na–$O3_{1,4}$ distance is the same as the Na–$O3_{2,3}$ distance at ambient pressure. At near this pressure, Na–$O3_{1,4}$ bonds may form, making Na 8-coordinated and constituting a *C*2/*c* → *C*2/*c* bonding transition. Solid lines are linear fits to the data.

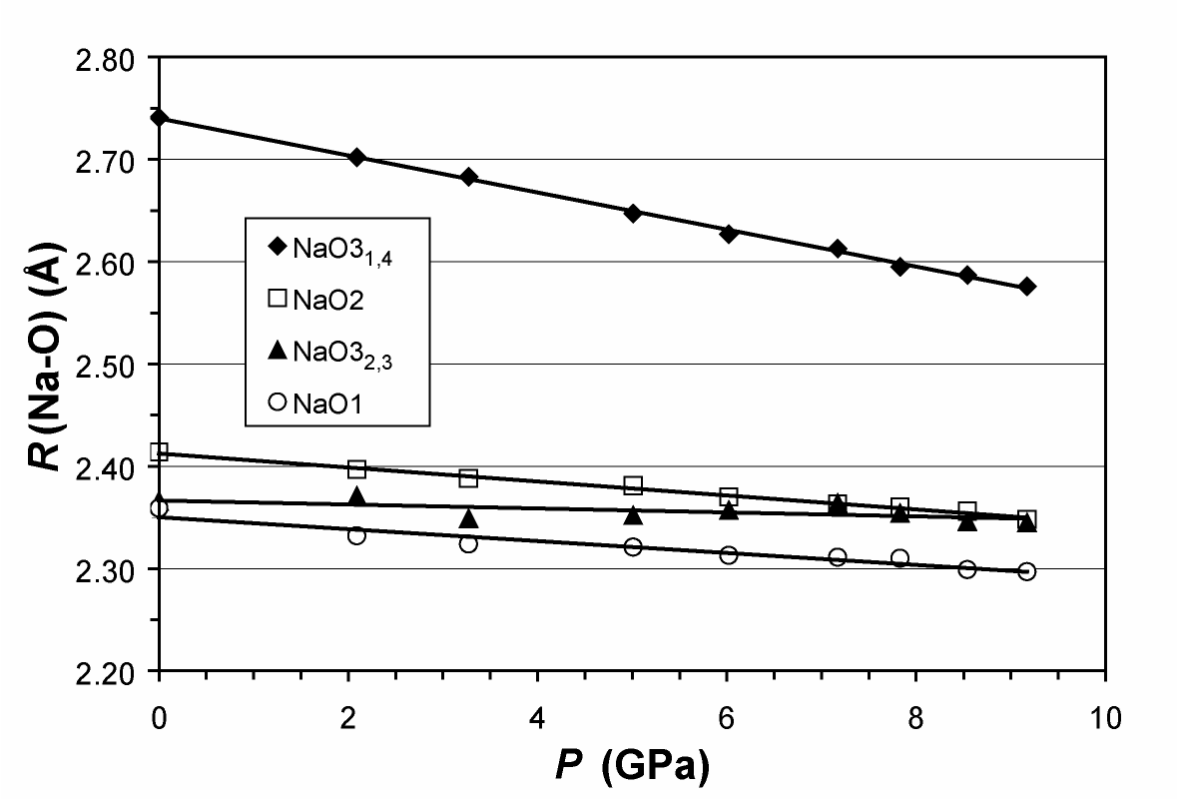

Figure 6. Variation of Al–O distances in jadeite with pressure at room temperature. Solid lines are linear fits to the data.

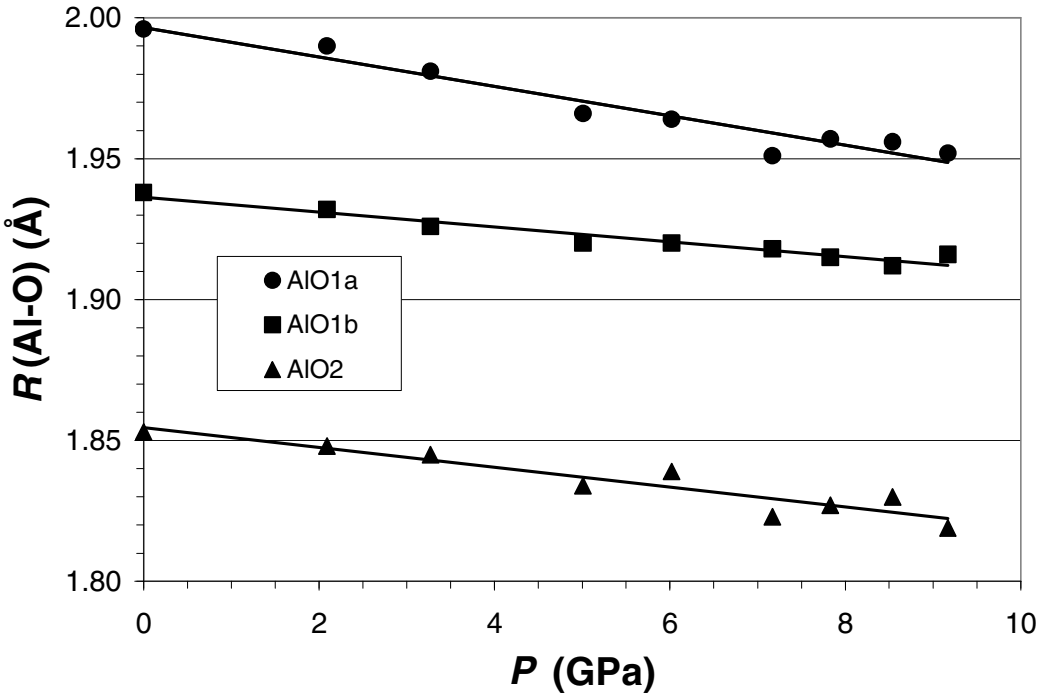

Figure 7. Variation of ∠O3-O3-O3 in two Na-clinopyroxenes (jadeite and kosmochlor) with pressure at room temperature. Kosmochlor data from Origlieri et al. (2003). Estimated errors in *P* are significantly smaller than the symbols used.

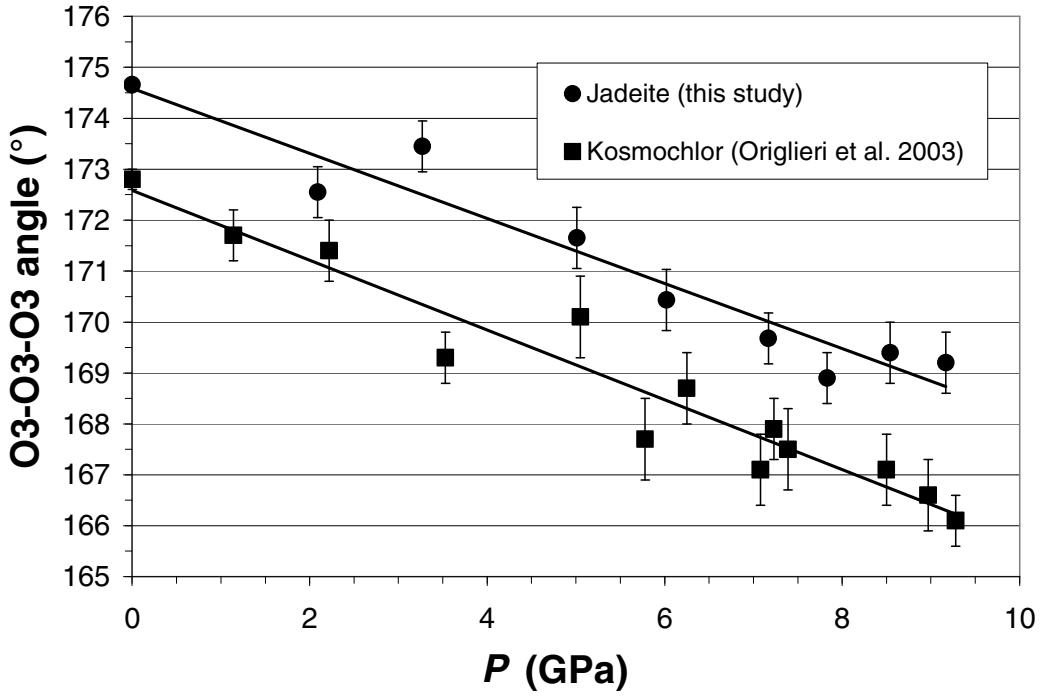

Figure 8. Unbonded nearest-neighbor M2–$O3_{1,4}$ distances and bonded M2–$O3_{2,3}$ in Na-clinopyroxenes from the literature. M2–$O3_{1,4}$ distance is correlated with unit cell volume at ambient conditions. Therefore, at room conditions, jadeite is the Na-clinopyroxene structure geometrically closest to a postulated *C*2/*c* → *C*2/*c* transition. Which pyroxene transforms first will also be a function of the rate of decrease in the M2–$O3_{1,4}$ distance with *P*. The linear fits to the upper and lower trends have R^2 values of 0.97 and 0.91, respectively. Structural data taken from: jadeite, this study; namansilite (NaMnSi2O6), Ohashi et al. 1987; aegirine, Redhammer et al. 2000; $NaTiSi_2O_6$, Redhammer et al. 2003; jervisite ($NaScSi_2O_6$), Ohashi et al. 1994a; natalyite ($NaVSi_2O_6$), Ohashi et al. 1994b; kosmochlor, Origlieri et al. 2003; $NaGaSi_2O_6$, Ohashi et al. 1995; $NaInSi_2O_6$, Ohashi et al. 1990.

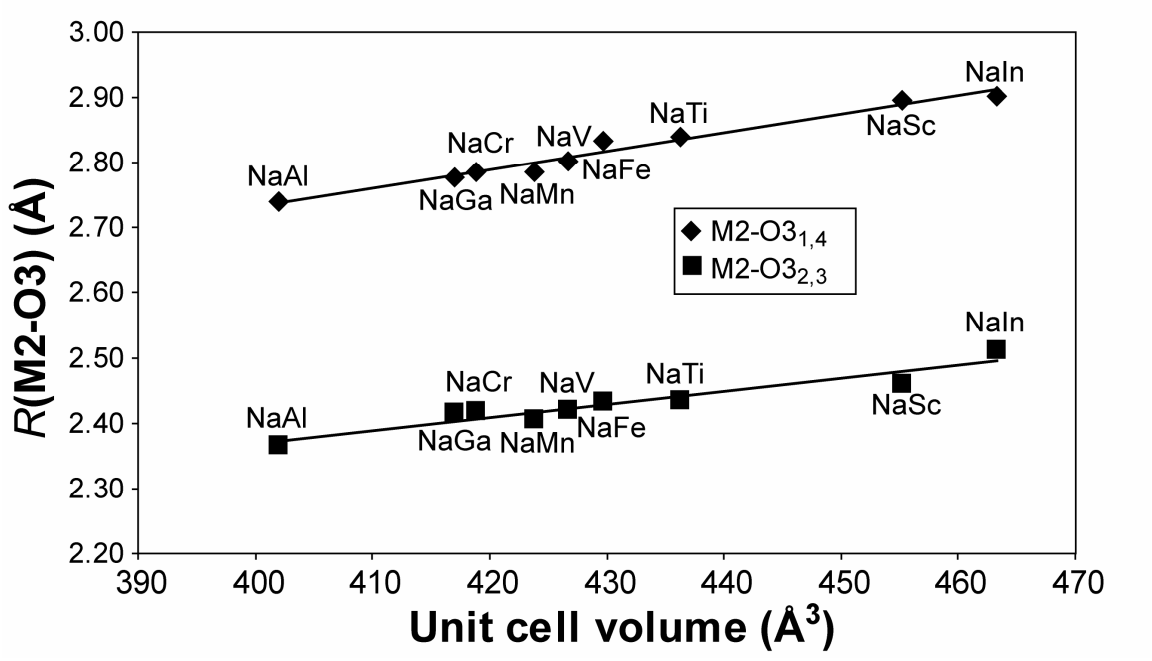

Figure 9. (A) Bulk moduli versus cell volume for *C*2/*c* and *P*2$_1$/*c* silicate pyroxenes recalculated (with $K_0^{'} \equiv 4.0$) using data from the literature. All pyroxenes in the upper trend have two antipathetic M2–O3 bonds. Pyroxenes in the lower trend do not exhibit these bonds. The difference in M2–O3 bonding is the only topological difference among the pyroxenes considered. (B) Constrained bulk moduli versus cell volume for *Pbca* and *P*2$_1$*cn* silicate pyroxenes from the literature. No clear trends are observed, perhaps due to the limited number of data points.

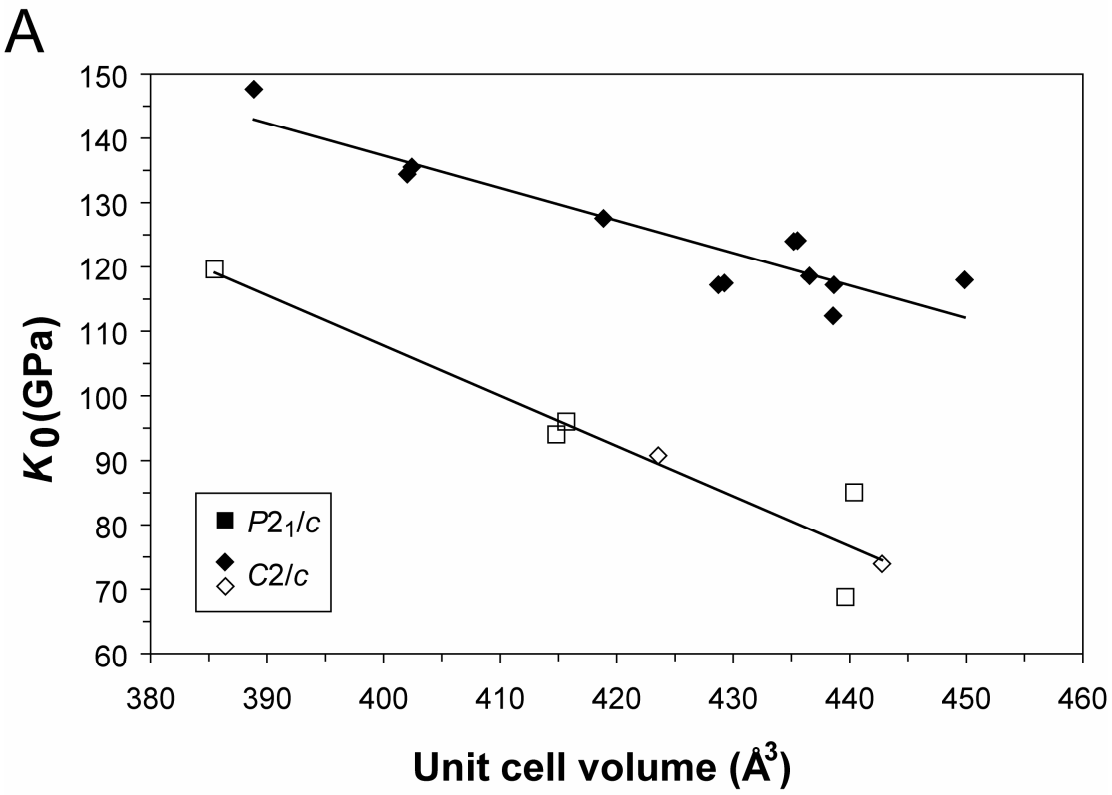

Fig. 9 cont.

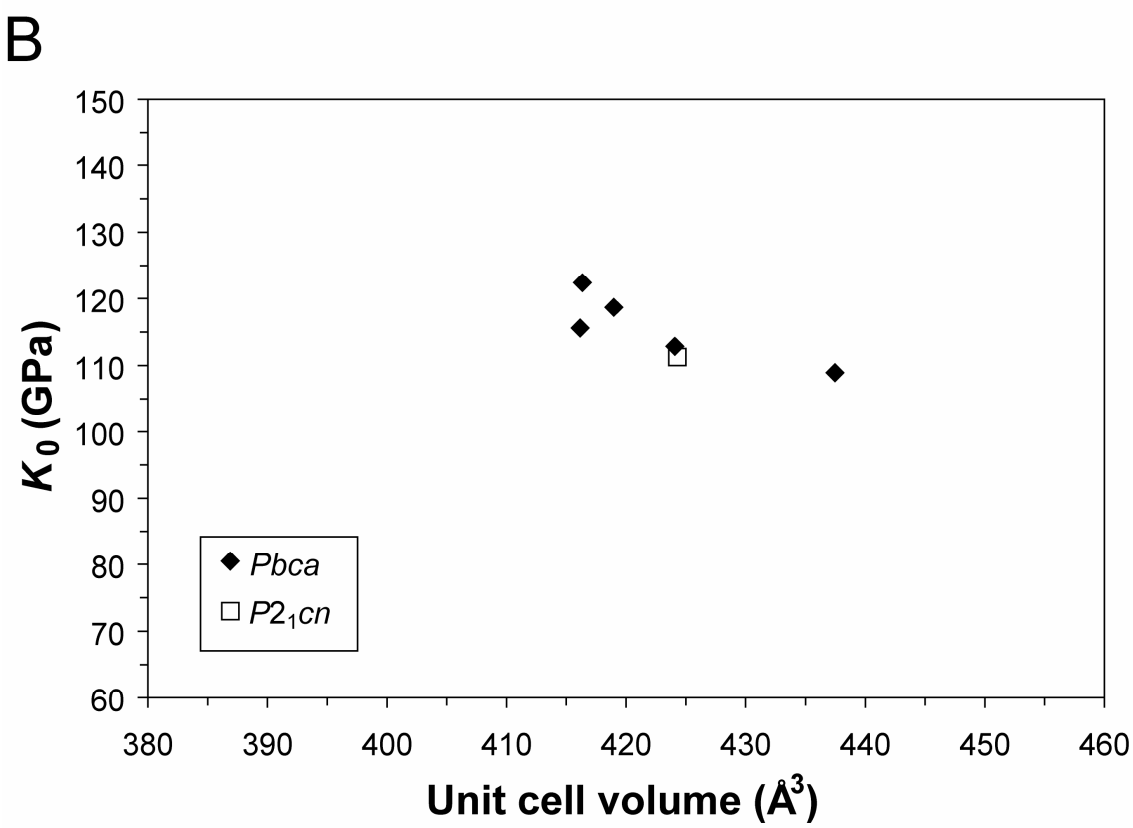
B
150
140
130
120
110
100
90
80
70
60
K_0 (GPa)
380
390
400
410
420
430
440
450
460
Unit cell volume (Å^3)
Pbca
P2$_1$cn

Figure 10. Bonding environments of the M2 cation in HT *C*2/*c*, *P*2$_1$/*c* and HP *C*2/*c* $ZnSiO_3$ structures. (A) HT *C*2/*c* $ZnSiO_3$, with no M2–O3 bonds, is the most compressible of all the *C*2/*c* pyroxenes considered in this study (K_0 ~ 74 GPa). (B) *P*2$_1$/*c* $ZnSiO_3$, with two sympathetic M2–O3 bonds, is even more compressible (K_0 ~ 69 GPa). (C) HP *C*2/*c* $ZnSiO_3$, also with two sympathetic M2–O3 bonds, has a much smaller cell volume V_0 and is thus much stiffer (K_0 ~ 91 GPa).

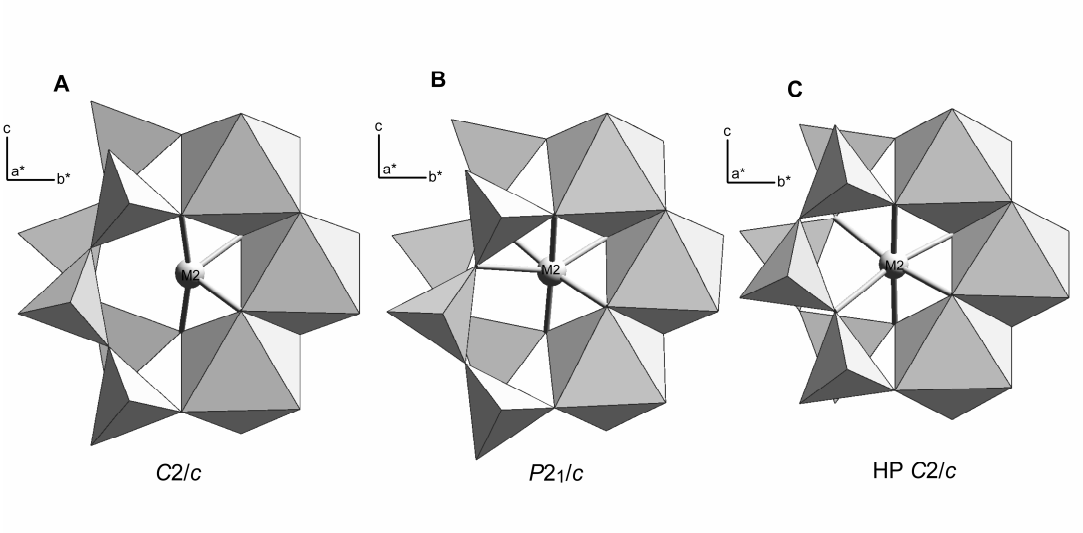

Figure 11. Measured M2–O3 distances normalized to model M2–O3 distances created by scaling of the unit cell and the β angle, in jadeite (solid symbols) and diopside (outlined symbols). Interatomic distances associated with sympathetic M2–O3 motion become shorter with pressure than predicted by the scaled-cell model, whereas antipathetic M2–O3 bonds become slightly longer than expected, with increasing pressure.

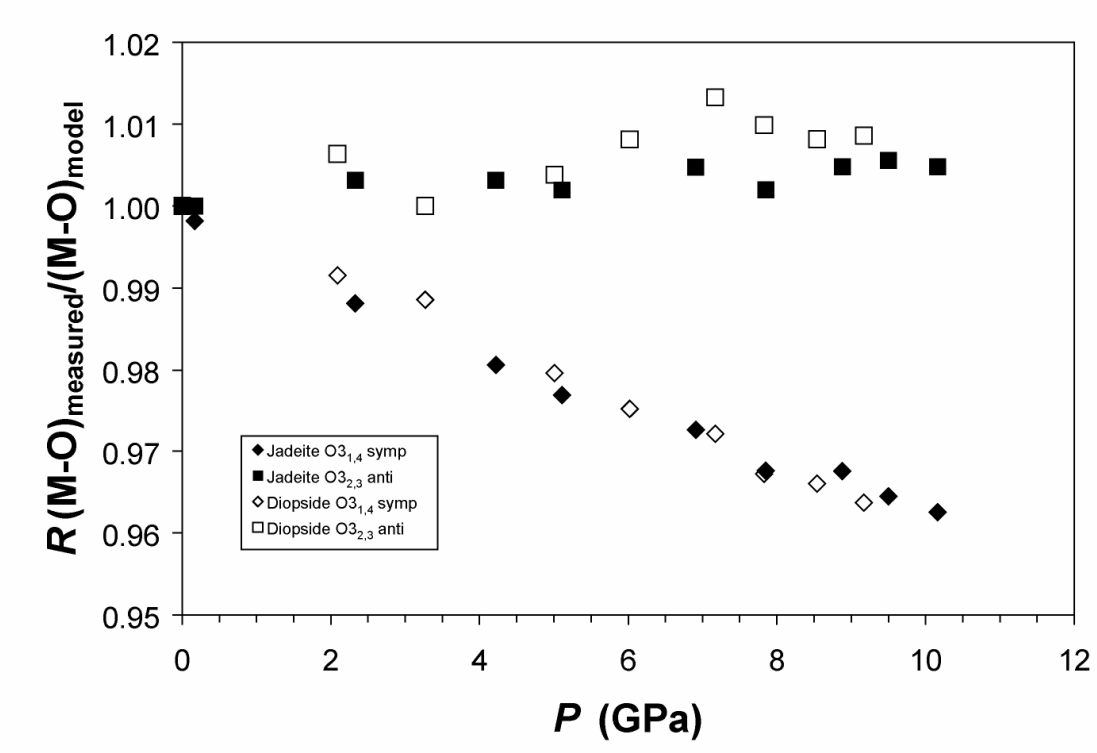

Table 1. Constrained bulk moduli and other parameters, determined by high-pressure single-crystal X-ray diffraction, for pyroxenes considered in this study. Values have been recalculated using reported cell parameters from the literature. Bulk moduli versus ambient cell volumes from this table are plotted in Figure 9.

M2M1	Space Group	Mineral Name	Pressure Range (GPa)	# Measured Cell Params	Fitted V_0* (Å^3)	Constrained Bulk Modulus (GPa)*	M2-O3 bonds**	Sympathetic or Antipathetic?	Ref.
LiAl	*C*2/*c*	spodumene	0-3.19	7	388.87	147.7	2,3	anti	b
NaAl	*C*2/*c*	jadeite	0-9.17	16	402.03	134.4	2,3	anti	a
NaAl	*C*2/*c*	jadeite	0-8.31	13	402.42	135.5	2,3	anti	c
NaFe	*C*2/*c*	aegirine	0-11.55	15	428.72	117.2	2,3	anti	d
NaFe	*C*2/*c*	aegirine	0-9.74	12	429.25	117.5	2,3	anti	c
NaCr	*C*2/*c*	kosmochlor	0-9.28	19	418.87	127.5	2,3	anti	e
CaMg	*C*2/*c*	diopside	0-10.16	10	438.64	117.2	2,3 1,4	both	g
CaMg	*C*2/*c*	diopside	0-9.97	33	438.56	112.4	2,3 1,4	both	h
$(Ca_{0.80}Mg_{0.20})(Mg_{1.00})$	*C*2/*c*	diopside	0-15.1	23	436.55	118.6	2,3 1,4	both	q
$(Ca_{0.88}K_{0.12})(Mg_{0.83}Al_{0.17})$	*C*2/*c*	diopside	0-9.48	16	435.52	124.1	2,3 1,4	both	i
CaNi	*C*2/*c*	n/a	0-7.76	18	435.20	124.0	2,3 1,4	both	n
CaFe	*C*2/*c*	hedenbergite	0-9.97	33	449.86	118.0	2,3 1,4	both	h
ZnZn	*C*2/*c*	n/a	0-1.92	7	442.77	73.9	none	--	b
ZnZn	HP *C*2/*c*	n/a	4.90-7.43	6	423.57	90.8	1,4	symp	b
LiFe	*P*2$_1$/*c*	n/a	1.08-7.22	16	414.82	94.0	2	symp	j
$(Li_{0.85}Mg_{0.09}Fe_{0.06})(Fe_{0.85}Mg_{0.15})$	*P*2$_1$/*c*	n/a	0-6.83	17	415.67	96.0	2?	symp?	o
LiSc	*P*2$_1$/*c*	n/a	0.66-4.80	9	440.39	85.1	2	symp	b
LiAl	*P*2$_1$/*c*	spodumene	3.34-8.84	7	385.50	119.6	2 then 2 4	symp	b
ZnZn	*P*2$_1$/*c*	n/a	1.99-4.80	9	439.63	68.8	1 3	symp	b
MgMg	*Pbca*	enstatite	0-8.51	26	416.25	115.8	2 4	symp	k
$(Mg_{0.59}Fe_{0.41})(Mg_{0.59}Fe_{0.41})$	*Pbca*	enstatite	0-7.50	17	424.19	113.0	2 4	symp	l
$(Mg_{0.66}Fe_{0.24}Al_{0.08}Ca_{0.01})(Mg_{1.00})$	*Pbca*	enstatite	0-8.62	21	416.44	122.6	2 4	symp	l
FeFe	*Pbca*	ferrosilite	0-5.41	17	437.60	109.1	2 4	both	l
$(Mg_{0.93}Ca_{0.07})(Mg_{1.00})$	*Pbca*	enstatite	0-10.16	10	419.07	118.9	2 4	symp	p
$(Mg_{0.77}Sc_{0.23})(Mg_{0.77}Li_{0.23})$	*P*2$_1$*cn*	enstatite	2.50-9.98	5	424.39	111.4	1+	?	m

Notes: Column labels are defined as: M2M1: identification of the atoms in the M2 and M1 sites. Space Group: space group of the structure over the pressure range used to calculate bulk modulus. Mineral Name: mineral name, if applicable. Many pyroxenes reported here do not occur naturally and thus do not have mineral names. Pressure Range: the pressure range over which cell parameters were collected and used to calculate bulk modulus. # Measured Cell Params: the number of measured cell parameters fit to calculate bulk modulus. Fit V_0: the resulting fit V_0 from our software used to fit the *P-V* data. Constrained Bulk Modulus: bulk modulus calculated with Down's BMUR software, with $K'_0 \equiv 4.0$. M2-O3 bonds: identity of existing M2-O3 bonds following the nomenclature of Downs (2003). Sympathetic or Antipathetic?: nature of the M2-O3 bonds in relation to Si chain kinking (see text). Ref.: References; (a) This study; (b) Arlt and Angel (2000); (c) Nestola et al. (2006a); (d) Downs and Singh (2006); (e) Origlieri et al. (2003); (g) Thompson et al. (in preparation); (h) Zhang et al. (1997); (i) Bindi et al (2006); (j) Downs et al. (in preparation); (k) Hugh-Jones and Angel (1994); (l) Hugh-Jones et al. (1997); (m) Yang et al. (1999); (n) Nestola et al. (2005); (o) Gatta et al. (2005); (p) Nestola et al. (2006b); (q) Tribaudino et al. (2000).

* K'_0 constrained to 4.0. For comparison with clinopyroxenes, orthopyroxene cell volumes are halved.
** Numbers represent the oxygens to which M2 is bonded, following the nomenclature of Downs (2003).

Table 2. Jadeite unit-cell data as a function of pressure

P (GPa)	*a* (Å)	*b* (Å)	*c* (Å)	β (°)	*V* (Å^3)
0.0001*	9.4242(2)	8.5657(2)	5.2242(2)	107.578(2)	402.03(2)
2.07*	9.3718(3)	8.5240(6)	5.1985(3)	107.399(3)	396.28(4)
3.40*	9.3372(3)	8.4966(6)	5.1805(3)	107.285(3)	392.43(4)
4.01	9.3260(5)	8.4854(9)	5.1735(4)	107.228(5)	391.04(5)
4.53	9.3112(2)	8.4724(5)	5.1656(2)	107.194(2)	389.29(3)
4.92*	9.3030(4)	8.4666(8)	5.1609(4)	107.140(4)	388.44(5)
5.22	9.2968(2)	8.4602(4)	5.1576(2)	107.124(2)	387.67(3)
5.51	9.2926(5)	8.4566(9)	5.1553(5)	107.110(5)	387.19(6)
6.1	9.2800(2)	8.4452(5)	5.1474(2)	107.056(2)	385.67(3)
6.12*	9.2793(3)	8.4446(6)	5.1474(3)	107.054(3)	385.61(4)
6.66	9.2688(4)	8.4346(8)	5.1411(4)	107.002(4)	384.36(5)
7.17*	9.2593(2)	8.4268(5)	5.1354(3)	106.979(3)	383.23(3)
7.43	9.2532(1)	8.4199(3)	5.1315(1)	106.955(1)	382.43(2)
7.83*	9.2455(4)	8.4137(8)	5.1269(4)	106.910(4)	381.57(5)
8.54*	9.2305(2)	8.3999(5)	5.1178(2)	106.854(3)	379.77(3)
9.17	9.2185(2)	8.3871(5)	5.1099(2)	106.794(2)	378.23(3)

Note: Space group = *C*2/*c*

* Intensity data collected at this pressure

Table 3. Structural parameters for jadeite in air at room conditions.

atom	*x*	*y*	*z*	B_{eq} (Å^2)	β_{11}	β_{22}	β_{33}	β_{12}	β_{13}	β_{23}
NaM2	0	0.3006(1)	¼	1.305(17)	0.00432(10)	0.00419(12)	0.01090(33)	0	0.00034(15)	0
AlM1	0	0.90601(7)	¼	0.746(14)	0.00197(7)	0.00324(9)	0.00637(24)	0	0.00091(103)	0
Si	0.29063(4)	0.09334(4)	0.22786(8)	0.733(12)	0.00189(5)	0.00320(7)	0.00640(17)	-0.00007(3)	0.00094(7)	-0.00005(6)
O1	0.1093(1)	0.0759(1)	0.1280(2)	0.824(19)	0.00207(12)	0.00373(13)	0.00692(37)	-0.00006(9)	0.00093(16)	0.00014(17)
O2	0.3611(1)	0.2634(1)	0.2929(2)	0.975(19)	0.00284(11)	0.00374(13)	0.00929(36)	-0.00037(10)	0.00164(17)	-0.00031(17)
O3	0.3537(1)	0.0071(1)	0.0057(2)	0.935(19)	0.00249(10)	0.00415(129)	0.00779(19)	0.00003(12)	0.00124(14)	-0.00063(37)

Note: Space group = *C*2/*c*

Table 4. Structural parameters for jadeite as a function of pressure

P (GPa)	2.07	3.40	4.92	6.12	7.17	7.83	8.54	9.17
obs refl	229	223	218	231	226	236	184	184
total refl	279	280	277	276	275	283	270	268
*p**	0.025	0.03	0.035	0.03	0.03	0.03	0.022	0.022
R_w	0.039	0.043	0.047	0.044	0.044	0.045	0.035	0.034
Al *y*	0.9066(3)	0.9072(4)	0.9077(4)	0.9076(4)	0.9081(4)	0.9075(4)	0.9080(5)	0.9078(5)
B	0.65(4)	0.72(4)	0.57(4)	0.66(4)	0.63(4)	0.62(4)	0.55(4)	0.54(4)
Na *y*	0.3010(5)	0.3021(5)	0.3032(6)	0.3029(5)	0.3025(5)	0.3039(6)	0.3043(6)	0.3044(6)
B	1.24(5)	1.29(6)	1.12(6)	1.10(6)	1.16(6)	1.13(6)	0.92(6)	1.06(6)
Si *x*	0.2910(1)	0.2912(1)	0.2913(2)	0.2914(1)	0.2913(1)	0.2913(2)	0.2915(2)	0.2913(2)
y	0.0939(2)	0.0941(2)	0.0945(3)	0.0946(2)	0.0946(2)	0.0948(2)	0.0956(3)	0.0957(3)
z	0.2285(2)	0.2284(2)	0.2290(3)	0.2289(2)	0.2291(3)	0.2291(3)	0.2297(3)	0.2297(3)
B	0.63(3)	0.67(3)	0.61(4)	0.65(3)	0.64(3)	0.65(3)	0.51(3)	0.55(3)
O1 *x*	0.1089(3)	0.1085(3)	0.1081(4)	0.1086(3)	0.1086(3)	0.1085(3)	0.1082(4)	0.1087(4)
y	0.0780(5)	0.0788(5)	0.0787(6)	0.0787(6)	0.0779(6)	0.0789(6)	0.0801(7)	0.0799(7)
z	0.1286(6)	0.1288(6)	0.1288(7)	0.1294(6)	0.1295(7)	0.1293(7)	0.1295(7)	0.1306(7)
B	0.63(6)	0.74(6)	0.63(7)	0.65(6)	0.74(6)	0.59(6)	0.58(7)	0.60(7)
O2 *x*	0.3610(3)	0.3606(4)	0.3608(4)	0.3601(4)	0.3610(4)	0.3602(4)	0.3599(4)	0.3609(4)
y	0.2639(6)	0.2650(6)	0.2664(7)	0.2658(6)	0.2675(7)	0.2672(7)	0.2672(7)	0.2677(7)
z	0.2954(6)	0.2975(6)	0.2988(7)	0.3002(6)	0.3012(6)	0.3024(6)	0.3032(7)	0.3040(7)
B	0.95(6)	0.92(7)	0.86(7)	0.87(7)	0.84(7)	0.86(7)	0.78(7)	0.95(8)
O3 *x*	0.3543(3)	0.3550(3)	0.3554(4)	0.3562(3)	0.3562(4)	0.3570(4)	0.3570(4)	0.3573(4)
y	0.0099(6)	0.0087(7)	0.0111(8)	0.0128(7)	0.0138(7)	0.0148(7)	0.0142(8)	0.0145(9)
z	0.0048(5)	0.0037(6)	0.0022(7)	0.0018(6)	0.0005(6)	0.0016(6)	0.0005(7)	-0.0005(8)
B	0.76(6)	0.88(6)	0.78(7)	0.81(6)	0.86(6)	0.73(6)	0.63(7)	0.78(7)

Note: $x_{Al} = x_{Na} = 0$; $z_{Al} = z_{Na} = ¼$.

* Weights computed by $\omega = [\sigma_F^2 + (pF)^2]^{-1}$

Table 5. Selected bond lengths (Å), volumes (Å^3), distortion parameters, and angles (°) from structure refinements

P (GPa)	0.0001$^{\delta}$	2.07	3.40	4.92	6.12	7.17	7.83	8.54	9.17
R(SiO1)	1.636(1)	1.634(3)	1.634(3)	1.634(4)	1.628(3)	1.624(3)	1.623(3)	1.625(3)	1.617(3)
R(SiO2)	1.595(1)	1.586(5)	1.587(5)	1.591(6)	1.580(5)	1.593(5)	1.585(5)	1.575(6)	1.580(6)
R(SiO3a)	1.632(1)	1.621(4)	1.627(4)	1.624(4)	1.618(4)	1.617(4)	1.611(4)	1.618(4)	1.622(5)
R(SiO3b)	1.637(1)	1.640(4)	1.627(4)	1.627(5)	1.631(5)	1.627(4)	1.636(5)	1.628(5)	1.624(6)
<*R*(SiO)>	1.6247	1.6203	1.6189	1.6187	1.6140	1.6147	1.6136	1.6116	1.6109
V(SiO_4)	2.1833	2.1678	2.1621	2.1619	2.1436	2.1481	2.1424	2.1342	2.1304
TAV*	22.9813	20.2149	19.6380	19.1417	18.7610	19.6542	18.6671	18.6510	20.2520
MTQE**	1.0055	1.0049	1.0048	1.0047	1.0045	1.0047	1.0045	1.0045	1.0048
R(NaO1)	2.360(1)	2.332(5)	2.324(6)	2.321(6)	2.313(6)	2.311(6)	2.310(6)	2.299(7)	2.297(7)
R(NaO2)	2.414(1)	2.397(3)	2.388(3)	2.381(4)	2.371(3)	2.363(4)	2.360(4)	2.356(4)	2.348(4)
R(NaO3c)	2.366(1)	2.371(5)	2.349(6)	2.352(7)	2.357(6)	2.364(6)	2.354(6)	2.346(7)	2.345(7)
R(NaO3d)	2.741(1)	2.702(5)	2.683(5)	2.647(6)	2.627(5)	2.613(5)	2.595(5)	2.587(5)	2.576(6)
diff	0.375	0.331	0.334	0.295	0.270	0.249	0.241	0.241	0.231
<*R*(NaO)>	2.470	2.451	2.436	2.425	2.417	2.413	2.405	2.397	2.392
R(AlO1a)	1.996(1)	1.990(4)	1.981(5)	1.966(5)	1.964(4)	1.951(4)	1.957(4)	1.956(5)	1.952(5)
R(AlO1b)	1.938(1)	1.932(3)	1.926(3)	1.920(3)	1.920(3)	1.918(3)	1.915(3)	1.912(3)	1.916(4)
R(AlO2)	1.853(1)	1.848(5)	1.845(5)	1.834(5)	1.839(5)	1.823(5)	1.827(5)	1.830(6)	1.819(6)
<*R*(AlO)>	1.9288	1.9233	1.9175	1.9072	1.9078	1.8996	1.8996	1.8990	1.8956
V(AlO_6)	9.3676	9.2955	9.2119	9.0623	9.0759	8.9299	8.9568	8.9511	8.9079
OAV*	47.7746	45.5977	45.5225	45.9720	44.8669	44.7608	45.5179	44.8290	43.3377
MOQE**	1.0151	1.0145	1.0144	1.0146	1.0141	1.0142	1.0144	1.0141	1.0139
Si-O3-Si	139.12(7)	138.8(2)	138.6(2)	138.2(3)	137.6(2)	137.4(2)	136.8(2)	137.0(3)	136.7(3)
O3-O3-O3	174.7(1)	172.6(5)	173.5(5)	171.7(6)	170.4(6)	169.7(5)	168.9(5)	169.4(6)	169.2(6)

Notes: δ Structure at 0.0001 GPa was refined with anisotropic temperature factors
The O3a in SiO3a is at [0.355,0.008,0.004]
The O3c in NaO3c is at [0.145,0.508,0.496]
The O1a in AlO1a is at [0.108,0.078,0.129]
* TAV/OAV: Tetrahedral/octahedral angle variance
** MTQE/MOQE: Mean tetrahedral/octahedral quadratic elongation
diff: length difference between the shortest and longest reported Na-O bonds

Table 6. Coulomb repulsion for selected cation-cation distances in jadeite over the pressure range in this study

	Repulsion (N) ($\times 10^{-28}$)					
P (GPa)	M2-T (edge sharing)	M2-T (2nd closest)	M1-M1	M1-M2	M1-T	T-T
0.0001	1.036	0.918	0.981	0.927	0.961	0.984
2.09	1.047	0.927	0.993	0.934	0.965	0.990
3.27	1.055	0.938	1.003	0.935	0.968	0.996
5.01	1.064	0.947	1.014	0.937	0.971	1.001
6.02	1.068	0.951	1.019	0.943	0.974	1.005
7.17	1.071	0.953	1.026	0.947	0.976	1.011
7.83	1.075	0.961	1.026	0.948	0.978	1.013
8.54	1.082	0.963	1.033	0.949	0.978	1.011
9.17	1.084	0.965	1.035	0.952	0.980	1.014

Table 7. Predicted bulk moduli for silicate clinopyroxenes from two groups: 1) those with antipathetic M2-O3 bonds; and 2) those without such bonds. Measured bulk moduli from single-crystal X-ray diffraction experiments are reported where available. The sympathetic versus antipathetic nature of M2-O3 bonds cannot be verified without structural data from several pressures (or possibly temperatures; see text).

M2M1	Space group	V_0*	Predicted K_0	Observed K_0**	Reference
Posess antipathetic M2-O3 bonds					
LiAl	*C*2/*c*	388.78	143.0	148(3)	b
NaAl	*C*2/*c*	402.03	136.3	134.4(3)	a
NaGa	*C*2/*c*	417.73	128.4	--	d
NaCr	*C*2/*c*	418.84	127.8	127.5(3)	e
NaMn	*C*2/*c*	423.85	125.3	--	f
NaV	*C*2/*c*	426.72	123.8	--	g
NaFe	*C*2/*c*	428.69	122.8	117(1)	h
CaNi	*C*2/*c*	435.21	119.5	124.0(4)	i
NaTi	*C*2/*c*	436.35	119.0	--	j
CaMg	*C*2/*c*	438.82	117.7	112.4(6)	k
CaCo	*C*2/*c*	443.52	115.3	--	l
CaFe	*C*2/*c*	449.90	112.1	118.0(4)	k
NaSc	*C*2/*c*	455.20	109.4	--	m
NaIn	*C*2/*c*	463.26	105.4	--	n
CaMn	*C*2/*c*	466.02	104.0	--	o
Do not posess antipathetic M2-O3 bonds					
LiAl	$P2_1/c$	385.50	119.1	120(2)	b
LiCr	*C*2/*c*	406.10	103.0	--	c
LiGa	*C*2/*c*	408.30	101.3	--	c
LiV	*C*2/*c*	413.31	97.4	--	c
LiFe	$P2_1/c$	414.82	96.2	94(2)	p
LiFe	*C*2/*c*	415.78	95.5	--	c
ZnZn	HP *C*2/*c*	423.57	89.4	91(3)	b
LiTi	*C*2/*c*	423.93	89.2	--	q
ZnZn	$P2_1/c$	439.63	76.9	69(2)	b
LiSc	*C*2/*c*	440.21	76.5	--	b
LiSc	$P2_1/c$	440.39	76.3	85(3)	b
ZnZn	*C*2/*c*	442.77	74.5	74(1)	b
LiIn	*C*2/*c*	447.78	70.6	--	c

References: (a) This study; (b) Arlt and Angel 2000; (c) Redhammer and Roth 2004; (d) Ohashi et al. 1995; (e) Origlieri et al. 2003; (f) Ohashi et al. 1987; (g) Ohashi et al. 1994b; (h) Downs and Singh 2006; (i) Nestola et al. 2005; (j) Ohashi et al. 1982; (k) Zhang et al. 1997; (l) Ghose et al. 1987; (m) Ohashi et al. 1994a; (n) Ohashi et al. 1990; (o) Freed and Peacor 1967; (p) Downs et al. (in preparation); (q) Kopnin et al. 2003.

* As reported by referenced authors

** As calculated in this study, with $K'_0 \equiv 4.0$.

APPENDIX B:

IN-SITU HIGH-PRESSURE SINGLE-CRYSTAL X-RAY STUDY OF AEGIRINE, $NaFe^{3+}Si_2O_6$, AND THE ROLE OF M1 SIZE IN CLINOPYROXENE COMPRESSIBILITY

In-situ high-pressure single-crystal X-ray study of aegirine, $NaFe^{3+}Si_2O_6$, and the role of M1 size in clinopyroxene compressibility

Andrew C. McCarthy[1]*, Robert T. Downs[1], Richard M. Thompson[1] and Günther J. Redhammer[2]

[1]*Department of Geosciences, University of Arizona, Tucson, Arizona 85721-0077, U.S.A.*

[2]*Department of Materials Engineering and Physics, Division of Mineralogy, University of Salzburg, Hellbrunnerstr. 34, A-5020 Salzburg, Austria*

* Email: mccarthy@geo.arizona.edu

Abstract

The crystal structure of a synthetic aegirine crystal, $NaFe^{3+}Si_2O_6$, was studied at room temperature, under hydrostatic conditions, over the pressure range 0-11.55 GPa using single-crystal X-ray diffraction. Unit cell data were determined at 16 pressures, and intensity data were collected at eight of these pressures. A third-order Birch-Murnaghan equation of state fit to the *P-V* data from 0-11.55 GPa yielded K_0 = 117(1) GPa, $K_0^{'}$ = 3.2(2) and V_0 = 429.40(9) Å^3. Aegirine, like the other Na-clinopyroxenes that have been examined at high pressure, exhibits strongly anisotropic compression, with unit strain axial ratios ε_1:ε_2:ε_3 of 1.00:2.38:2.63. Silicate chains in aegirine become more O-rotated with pressure, reducing ∠O3-O3-O3 from 174.1(1)º at ambient pressure to 165.5(5)º at 10.82 GPa. No evidence of a phase transition was observed over the studied pressure range. The relationship between M1 cation radius and bulk modulus is

examined for 14 clinopyroxenes, and two distinct trends are identified in a plot of these values. The distinction between these trends can be explained by the presence or absence of antipathetic bonds around M2, a feature first described by McCarthy et al. (2007). Adjusting the bulk moduli for the effect of antipathetic bonds eliminates the two distinct trends and produces a single relationship between M1 cation radii and bulk moduli. Aegirine, with Fe^{3+}, has nearly the same bulk modulus, within error, as hedenbergite, with Fe^{2+}, despite the difference in M2 bonding topology, M2 (Fe) valence and ambient unit cell volume. Several explanations for this apparent paradox are considered.

Introduction

This study examines the relationship between M1 chemistry and compressibility in *C*2/*c* and $P2_1/c$ silicate clinopyroxenes. Many such pyroxenes have been subjected to high-pressure single-crystal X-ray diffraction studies (Hugh-Jones and Angel 1994; Hugh-Jones et al. 1997; Zhang et al. 1997; Arlt et al. 1998; Yang et al. 1999; Arlt and Angel 2000; Hattori et al. 2000; Tribaudino et al. 2000; Origlieri et al. 2003; Gatta et al. 2005; Bindi et al. 2006; Downs and Singh 2006; Nestola et al. 2006; McCarthy et al. 2007; Thompson and Downs, accepted). We examine data for 14 pyroxenes: aegirine (this study) plus 13 from the literature. First-order structural controls of the compressibility of individual pyroxenes are thought to be well understood (cf. Thompson and Downs 2004); however, measured pyroxene compressibility systematics are still an area of active research.

Thompson and Downs (2004) hypothesized that clinopyroxene compressibility is largely controlled by the compressive strength of the $M1O_6$ chains, which run parallel to **c**. These chains of edge-sharing polyhedra derive their compressive strength from short average M-O bonds and small M1-M1 separations. Examination of the bulk moduli of $Fe^{3+}O_6$ versus $Fe^{2+}O_6$ octahedra in various minerals shows that $Fe^{3+}O_6$ octahedra are significantly stiffer. Details are examined in the discussion section of this paper. The Si-O bonds in the SiO_4 tetrahedra are significantly shorter and therefore stronger than other M-O bonds in the pyroxene structures and the tetrahedra do not compress significantly, nor do they share edges with other polyhedra. This allows each SiO_4 tetrahedron significant freedom to rotate relative to its neighbors, subject to the constraints of M2-O3 bonds to bridging oxygens (McCarthy et al. 2007). The result is a SiO_4 tetrahedral chain that, by itself, does not offer significant resistance to compression parallel to the chain. Instead, the tetrahedra rotate, with concomitant kinking of the chains as measured by the O3-O3-O3 angle. The M1 chains cannot respond to compression in a similar manner due to the edge-sharing polyhedra that comprise the chain.

Unit strain ellipsoids represent the three-dimensional shape change of a unit cell, incorporating all influences on compressional behavior. If M1 chains are the major controller of pyroxene compressibility, we might expect the short (i.e. least compressible) axis of the unit strain ellipsoid to lie roughly parallel to the $M1O_6$ chain axis ($\|$**c**). This is, however, not generally the case. Instead, the short axis of the unit strain ellipsoid in clinopyroxenes typically bisects the **a** and **c**-axes, ~45º from **c** (Fig. 1) (cf. Orgilieri et al.

2003), demonstrating that there are other significant factors. Thompson and Downs (submitted) present a discussion of other controlling factors of pyroxene compression.

Downs (2003) showed that the major differences in pyroxene bond topologies involve M2 bonding. In pyroxenes, M2 is always bonded to at least four O atoms: two O1s and two O2s. In addition, M2 is usually bonded to either 1, 2 or 4 O3s. Figure 2 illustrates the bonding around M2 in aegirine and the atom nomenclature (Downs 2003) used in this paper. McCarthy et al. (2007) examined the effects of the various types of M2-O3 bonds on the bulk modulus in $C2/c$ and $P2_1/c$ pyroxenes. Increasing pressure on pyroxenes increases the kinking of their tetrahedra chains, as shown in numerous high-P studies. As T-chains become more kinked, and individual tetrahedra rotate, one of the bridging oxygen atoms (O3) moves closer to M2 than would be expected based simply on scaled contraction of the unit cell, while the other bridging O3 atom in the same chain moves away from M2. Figure 3 illustrates the SiO_4 rotation in aegirine and the resulting effects on M2-O3 separations. When M2-O3 bonds are present across these M2-O3 separations, the first type provide no opposition to kinking and are termed "sympathetic" (to T-chain kinking). In contrast, the second type of M2-O3 bonds shorten less than expected when the T-chains kink. In other words, in the absence of compression, T-chain kinking would lengthen these bonds. This has the effect of opposing tetrahedral rotation. Thus these bonds are termed "antipathetic" (to T-chain kinking). It must be noted that all interatomic distances in pyroxenes are observed to decrease with pressure, and that antipathetic M2-O3 bond lengths simply decrease less than expected based on scaling of the unit cell (McCarthy et al. 2007).

McCarthy et al. (2007) plotted bulk moduli versus ambient (or minimum stability pressure) unit cell volumes for 19 silicate clinopyroxenes (space groups $C2/c$ and $P2_1/c$). The data show wide dispersion, but the dispersion could be removed by describing two roughly linear trends with R^2 values of 0.83 (stiff trend) and 0.91 (soft trend). Close examination of M2-O3 bonding in relation to tetrahedral rotation with pressure revealed that all the structures in the upper, stiff trend exhibited some antipathetic M2-O3 bonds, while the structures in the lower, more compressible or soft trend exhibited no such bonds. Thus it turned out that M2-O3 bonding does impact pyroxene compressibilities, primarily due to its relationship with T-chain kinking.

Previous work

The structure of aegirine – at the time called acmite – was first reported by Clark et al. (1969). The mineral is isostructural with jadeite, $NaAlSi_2O_6$, kosmochlor, $NaCrSi_2O_6$, and other $C2/c$ pyroxene group minerals with Na at M2. Aegirine has been the subject of several previous studies at non-ambient conditions: at high temperatures by Cameron et al. (1973); at non-hydrostatic high pressures by Downs and Singh (2006); and at high pressures by Nestola et al. (2006). However, high-pressure structural information (i.e., atomic positions) for aegirine has not been previously reported.

Cameron et al. (1973) examined the aegirine structure at four temperatures from ambient to 800ºC. They found that aegirine cell parameters (a, b, c, β) and average M-O distances (Na-O, Fe-O) increased linearly with temperature. Over the temperature range studied, they observed rather minor changes in the aegirine cell parameters and

interatomic angles. For example, a change in the O3-O3-O3 angle of 0.7º (from 174.0(2)º to 174.7(2)º) was observed. In contrast, high-pressure studies such as the present one often observe an O3-O3-O3 angle change of ≥8º. An examination of data from Cameron et al. (1973) indicates that pyroxenes do follow the behavior suggested by Hazen and Finger (1982): namely, that increasing *T* has the opposite effect on cell parameters as increasing *P*. However, it is also clear that there is little variation in structures over the physically possible *T* range—i.e., from near 0 K to near the melting point of the material—to compare with high *P* data.

Downs and Singh (2006) examined data from the same high-pressure experiment discussed in this paper. Their focus was the response of aegirine above 11.55 GPa, caused by the non-hydrostatic freezing of the ethanol:methanol pressure medium.

Nestola et al. (2006) examined four crystals from the jadeite-aegirine solid solution at high pressures. They examined an end-member aegirine crystal over the pressure range 0-9.74 GPa and reported unit-cell parameters at 12 pressures. They reported a bulk modulus of 116.1(5) GPa and its pressure derivative, $K_0^{'} = 4.4(1)$, based on a third-order Birch-Murnaghan fit of their unit-cell data.

Experimental Methods

A pure synthetic aegirine crystal reported in Redhammer et al. (2000), run Nahp2, was selected for study based on crystal quality as determined by examination of peak profiles. Typical peak widths were 0.08º in ω. The size of the crystal was ~115 μm × 70 μm × 50 μm.

Diffraction data were collected with an automated Picker four-circle diffractometer using unfiltered MoKα radiation and operating at 45 kV and 40 mA. Before loading in the diamond cell, the crystal was examined in air. The positions of 28 high-intensity peaks ($13^\circ < 2\theta < 30^\circ$) were determined using a modification of the eight-peak centering technique of King and Finger (1979) by fitting both $K\alpha_1$ and $K\alpha_2$ profiles with Gaussian functions. Refined cell parameters constrained to monoclinic symmetry are reported in Table 1. A half-sphere of intensity data was collected to $2\theta \leq 60^\circ$, using ω scans of 1° width, step size 0.025°, and 5 s per step counting times. The structure was refined on *F* with anisotropic displacement parameters using a modification of RFINE (Finger and Prince, 1975) to $R_w = 0.012$. Structural data at room conditions are summarized in Table 2. These data have smaller errors than Clark et al. (1969) (R_w = 0.039) but otherwise compare favorably.

The aegirine crystal was loaded into a four-pin Merrill-Bassett type diamond-anvil cell with beryllium seats, with the (110) face parallel to the culet surfaces. The diamond anvil culet size was 600 μm. A 250 μm thick stainless steel gasket, pre-indented to 100 μm, with a hole diameter of 300 μm, was used. The cell was loaded with the aegirine crystal, a small ruby fragment, and a 4:1 mixture of methanol:ethanol as pressure medium. Ruby fluorescence spectra were collected before and after each collection of intensity data, and the positions of the R_1 and R_2 peaks were determined by fitting with Lorentzian functions. Pressure was calculated from the fitted R_1 and R_2 peak positions using the method of Mao et al. (1978), with an estimated error of ±0.05 GPa.

The experiment was carried out under hydrostatic conditions to a pressure of 11.15 GPa. Intensity data were collected at 9 pressures. Above this pressure, conditions appeared to be non-hydrostatic due to the freezing of the pressure medium. A discussion of the behavior of aegirine at non-hydrostatic conditions from this experiment is presented by Downs and Singh (2006).

Every accessible reflection allowed by *C*2/*c* symmetry, up to 728 intensity data ($2\theta \leq 60^{\circ}$), were collected at pressure, with ω scans of 1° width, in steps of 0.025° and counting times of 10 s per step. These data reduced to 320 symmetry-equivalent reflections. Reflections violating *C*2/*c* were examined, but none with significant intensities was found throughout the experiment. Absorption corrections for the beryllium seats and diamond anvils were made from an absorption correction profile of the diamond cell before loading. Structure factors were weighted by $\omega = [\sigma_F^2 + (pF)^2]^{-1}$, where σ_F was obtained from counting statistics and *p* chosen to insure normally distributed errors (Ibers and Hamilton, 1974). Structural data were refined with isotropic displacement factors using a modified version of RFINE (Finger and Prince, 1975) and are summarized in Table 3. Refinements from data collected at pressure yield R_w values ranging from 0.041 to 0.051.

Bond lengths, angles and errors were calculated using BOND91 software, modified after Finger and Prince (1975). Polyhedral volumes and quadratic elongations were obtained with XTALDRAW (Downs and Hall-Wallace, 2003). Selected bond lengths, angles, and polyhedral volumes are presented in Table 4.

Results and Discussion

Downs and Singh (2006) report a third-order Birch-Murnaghan *P-V* equation of state fit to measured cell parameters of aegirine from this experiment, over 0-11.15 GPa. This fit resulted in values of K_0 = 117(1) GPa, K_0' = 3.2(2), and V_0 = 429.40(9) Å^3. These values, with the exception of K_0', closely correspond to those reported by Nestola et al. (2006) from the pressure range 0-9.74 GPa: K_0 = 116.1(5) GPa, K_0' = 4.4(1), V_0 = 429.26(2) Å^3. The data and fitted curve from our experiment are plotted in Figure 4. The compressibility of aegirine, as reflected by V/V_0, is compared to that of other clinopyroxenes in Figure 2 of McCarthy et al. (2007). Aegirine is the most compressible of the Na-clinopyroxenes studied to date (a group that comprises jadeite, kosmochlor, and aegirine). No evidence of a symmetry transformation in aegirine was observed to a pressure of 11.15 GPa. All observed cell parameters decrease continuously with increasing pressure.

Cell-parameter data were used to construct unit strain ellipsoids with STRAIN, modified after Ohashi (1982). The unit strain ellipsoid (Fig. 1) is highly anisotropic, with axial ratios ε_1:ε_2:ε_3 of 1.00:2.38:2.63 in the range 0-11.55 GPa. The axial values of the unit strain ellipsoid are: ε_1, –0.001196; ε_2, –0.002725; and ε_3, –0.003050 GPa^{-1}, with ε_3 oriented 55.9º from **c**, and ε_2 parallel to **b**. Our results are similar to those of Nestola et al. (2006), who report aegirine unit strain ellipsoid axial ratios of 1.00:2.38:2.76 between 0 and ~5 GPa.

Procrystal electron density analysis of aegirine indicates the presence of six Na–O bonds at room conditions (Downs 2003), giving the mineral a bond topology identical to

jadeite, kosmochlor, and all other known *C*2/*c* pyroxenes with Na occupying M2 (Thompson et al. 2005). Na in aegirine resides on a two-fold axis, constraining the coordination of Na to an even number, and resulting in three pairs of equivalent Na–O bonds. The bond nomenclature used in this paper is described in Downs (2003) and illustrated in Figure 2. Na is not bonded to two nearest-neighbor oxygen atoms, $O3_1$ and $O3_4$, found at a distance of 2.834(2) Å at ambient pressure. All Na–O distances in aegirine decrease with pressure, although at different rates (Fig. 5). As in other Na clinopyroxenes, the (unbonded) Na–$O3_{1,4}$ distance is observed to decrease at a much higher rate (d*R*(NaO)/d*P*) than the bonded Na-O distances (McCarthy et al. 2007; Origlieri et al. 2003). At a sufficiently high pressure, the unbonded $O3_{1,4}$ atoms are expected to come close enough to Na at M2 to allow bond formation, making Na 8-coordinated with oxygen and bringing about a *C*2/*c* → *C*2/*c* bonding transition. The trend of the decreasing Na–$O3_{1,4}$ distance certainly suggests this. However, aegirine has a relatively long M2-$O3_{1,4}$ distance (McCarthy et al. 2007) and so does not seem an ideal candidate for displaying the *C*2/*c* → *C*2/*c* bonding transition at the lowest pressure of any Na clinopyroxene. Still, the unbonded Na-$O3_{1,4}$ distance in aegirine is projected to decrease to the ambient length of Na-O2 (2.409(1) Å) at 17.9 GPa, functionally identical to the predicted transition pressure of 17.8 GPa in jadeite (McCarthy et al. 2007). It appears that a high-pressure single-crystal X-ray diffraction study on aegirine or jadeite to ~20 GPa should observe a bond transition phenomenon, perhaps similar to the postulated *C*2/*c* → *C*2/*c* transition (Chopelas and Serghiou 2002), assuming other bond configurations in the structure remain stable.

The Fe atom in aegirine resides in the octahedral M1 site. It is 6-coordinated with oxygen at all pressures in this study. Fe–O bond lengths decrease systematically with pressure (Fig. 6). The $Fe^{3+}O_6$ octahedron becomes slightly more regular with pressure, with the mean quadratic elongation (Robinson et al. 1971) decreasing from 1.0135 at ambient conditions to 1.0118 at 10.82 GPa.

The O3-O3-O3 angle in aegirine decreases from 174.1(1)º at ambient conditions to 165.5(5)º at 10.82 GPa (Fig. 7). The resulting change in the structure due to the decrease in ∠O3-O3-O3 is illustrated in Figure 3. The decrease is approximately linear with P and the slope ($d\angle / dP$ –0.79º GPa^{-1}) generally compares with those of kosmochlor (–0.72º GPa^{-1}) (Origlieri et al. 2003) and jadeite (–0.60º GPa^{-1}) (McCarthy et al. 2007). In all three minerals, the silicate tetrahedra become more O-rotated with increased pressure. Model pyroxenes with closest-packed oxygen arrays exhibit O3-O3-O3 angles of 120º (cubic closest packed) and 240º (hexagonal closest packed) (Thompson 1970). Thus the oxygen atoms in aegirine move toward a cubic-closest-packed arrangement with pressure, but they are still far from it at 10.82 GPa.

M1 size versus bulk modulus

Thompson et al. (2005) demonstrated a near-linear, strongly correlated relationship (R^2 = 0.92) between M1 cation radii and unit cell volumes in a population of 22 *C*2/*c* pyroxenes (Fig. 8). Since bulk moduli are generally correlated with ambient unit cell volumes in isostructural materials (cf. Bridgman 1923; Anderson and Anderson 1970; Anderson 1972), it follows that clinopyroxene bulk moduli should be correlated

with M1 radii and other measures of the size of M1 polyhedra (e.g., polyhedral volume). This relationship is, however, too simple to completely explain the variation in clinopyroxene bulk moduli.

In Figure 9A we plot M1 cation radii versus bulk moduli for 14 clinopyroxene structures (space groups $C2/c$ and $P2_1/c$) that have been subjected to high-pressure X-ray diffraction studies. (Data used to create Figures 9 and 10 are presented in Table 5.) Although a general correlation exists between bulk moduli and M1 radii in $C2/c$ pyroxenes, this relationship is not as robust ($R^2 = 0.48$) as anticipated. This is probably related to the fact that the $C2/c$ pyroxenes considered are not completely isostructural (i.e., M2-O bonding varies), and, therefore, do not show identical structural behavior under compression. Unfortunately, our sample population is limited to a subset of the known end-member silicate clinopyroxenes because many have not been subjected to high-pressure X-ray diffraction studies sufficient to allow calculation of reliable bulk moduli. If the pyroxenes are considered based on their M2-O3 bonding topology as described by McCarthy et al. (2007), two trends can be identified in the data from Figure 9A, as shown in Figure 9B. Pyroxenes with no M2-O3 bonds, or M2-O3 bonds which are solely sympathetic, fall on the bottom portion of the figure. A linear fit to this trend yields $R^2 = 0.80$. Pyroxenes with some antipathetic M2-O3 bonds fall on the upper portion of the figure. A linear fit to this trend yields $R^2 = 0.68$. The dispersion among the trends indicates that structural factors other than the size of the M1 cation, and the details of M2-O3 bonding, influence the compression behaviors of the pyroxenes. For instance, three polymorphs of $ZnSiO_3$ are represented in Figures 9A and 9B. All three

fall in the sympathetic trend, with M1 (Zn) radius = 0.74 Å (Shannon 1976), and bulk moduli of 69 ($P2_1/c$), 74 (HT $C2/c$), and 91 (HP $C2/c$) GPa (Arlt and Angel, 2000). Each polymorph has a distinct M2 bonding topology that affects the compressibility of the structure, whereas the M1 cation radius remains constant.

There are other ways to measure the influence of M1 on the compressibilities of pyroxene structures. Since M1-O distances do vary slightly in real clinopyroxenes (Fig. 6), an alternate measure of the three-dimensional influence of M1 polyhedra may be its volume. We plot the ambient volume of the M1 polyhedra versus bulk moduli for the same 14 pyroxenes from the literature (Fig. 10A). Whereas the bulk moduli generally increase with decreasing M1 volume, a linear fit to all the data again produces a poor correlation ($R^2 = 0.48$). It is clear, therefore, that even though the volumes of the M1 polyhedra vary approximately linearly with the volumes of the pyroxene unit cell (Thompson et al. 2005), and the volumes of the pyroxene unit cell vary approximately linearly with the bulk moduli (when antipathetic/sympathetic M2-O3 bonding is taken into account) (McCarthy et al. 2007), the bulk moduli do not vary linearly with the size of M1. Thus, factors other than the considered measures of M1 size influence the bulk moduli of clinopyroxenes.

Figure 10A can be split into the same two categories shown in Figure 9B: those with antipathetic M2-O3 bonds and those without. The six pyroxenes on the lower part of Figure 10B have only sympathetic bonds, which has the effect of shifting them down on the figure (i.e., they are softer than expected based on the M1 polyhedral volumes). All the other pyroxenes represented have some antipathetic M2-O3 bonds.

Some of the dispersion in bulk moduli (y-axis) noted in plots such as Figure 10B can, therefore, be explained by the secondary control on bulk moduli: the antipathetic/sympathetic bond behavior of M2-O3. It is possible to remove this component and attempt to see more clearly the contribution of M1 polyhedra volume to the bulk moduli. McCarthy et al. (2007) suggested empirically-derived linear models for the bulk moduli of sympathetic and antipathetic pyroxenes. To correct the bulk moduli of the sympathetically-bonded clinopyroxenes, we found the difference (in units of bulk modulus, GPa) between the two models at the unit cell volume corresponding to each pyroxene, and added this value to the calculated bulk modulus. Figure 10C shows all the pyroxene data with the sympathetic pyroxene bulk moduli corrected as described. The correlation between M1 polyhedral volume and bulk modulus for the entire group of 14 pyroxenes improves significantly after applying this correction. A linear fit to the corrected population of 14 pyroxenes yields $R^2 = 0.66$.

Compression behavior of Fe^{2+} versus Fe^{3+} polyhedra

If clinopyroxene compressibilities are controlled to any significant degree by the size of M1, then those materials with Fe^{3+} at M1 should tend to be stiffer than those containing Fe^{2+} at this site. The O-O contacts in $Fe^{3+}O_6$ octahedra are shorter than those in $Fe^{2+}O_6$ octahedra, and M1-M1 electrostatic repulsion is stronger for a given M1-M1 separation. Also, Fe^{3+}-O bonds are shorter and stiffer than Fe^{2+}-O bonds due to the increased electrostatic forces between Fe^{3+} and O. Shannon (1976) reports the ionic radii of six-coordinated Fe^{2+} and Fe^{3+} as 0.780 Å and 0.645 Å, respectively. The average

ambient-condition Fe^{2+}-O bond distance in the $Fe^{2+}O_6$ octahedra in hedenbergite is 2.128(1) Å (Zhang et al. 1997), whereas the average Fe^{3+}-O bond in the $Fe^{3+}O_6$ octahedra in aegirine is 2.024(1) Å (this study). The ambient unit-cell volumes of hedenbergite and aegirine are 449.90(7) $Å^3$ (Zhang et al. 1997) and 428.69(2) $Å^3$ (this study). Each one of these factors indicates that aegirine, with Fe^{3+} at M1, should be significantly stiffer than hedenbergite, with Fe^{2+} at M1. Unexpectedly, however, the compressibilities of the two materials are nearly identical within error, with bulk moduli of 121(2) GPa (hedenbergite, Zhang et al. 1997) and 117(1) GPa (aegirine, Downs and Singh 2006). (All bulk moduli reported herein are recalculated using data from the literature with the constraint that $K_0^{'}$ ≡ 4.0.) It is rather surprising that aegirine does not have a markedly higher bulk modulus than other nearly isostructural pyroxenes with similar ambient unit-cell volumes. Both the aegirine and hedenbergite structures contain antipathetic M2-O3 bonds and thus fall on the upper trend described in McCarthy et al. (2007). Hedenbergite and aegirine are isostructural except for bonding around M2. Procrystal analysis shows that hedenbergite has 8-coordinated Ca whereas aegerine has 6-coordinated Na in M2 at room conditions (Downs 2003). It is tempting to suggest that this difference in bonding could account for the anomalous stiffness of hedenbergite. Other *C*2/*c* pyroxenes with 8-coordinated Ca at M2, however, fall on a roughly linear trend (with $R^2 = 0.82$) with Na-clinopyroxenes when bulk modulus is plotted versus ambient unit cell volume (Figure 9 in McCarthy et al. 2007). The compressibility of the NaO_6 versus the CaO_8 polyhedra is considered further, below.

The only other studied silicate clinopyroxene with Fe^{3+} at M1 is Li-aegirine ($LiFeSi_2O_6$), which exhibits $P2_1/c$ symmetry above 1.08 GPa (Hugh-Jones et al. 1997) and has a bulk modulus of 94(1) GPa. This structure contains only sympathetic M2-O3 bonds and thus falls on the lower, "soft" trend of McCarthy et al. (2007). Because of this, the $LiFeSi_2O_6$ structure is not isostructural with and thus not directly comparable to that of aegirine, although the compressibility of the $Fe^{3+}O_6$ octahedra in $LiFeSi_2O_6$ is considered below.

To test our assumptions about the compressibility of the $Fe^{2+}O_6$ versus $Fe^{3+}O_6$ octahedra, we identified materials in the literature that contain Fe in octahedral coordination and have been examined with high-pressure single-crystal X-ray diffraction. Polyhedral volumes were derived from reported structures and were fit with a Birch-Murnaghan *P-V* equation of state in the same manner described above, with $K_0' \equiv 4.0$. The results from ten structures containing FeO_6 polyhedra are reported in Table 6. These results show that $Fe^{3+}O_6$ octahedra are stiffer than $Fe^{2+}O_6$ octahedra, as expected based on polyhedral volumes and average Fe-O bond lengths. Strikingly, the bulk moduli of the $Fe^{3+}O_6$ octahedra in the silicate minerals andradite (Hazen and Finger 1989), aegirine (this study), and Li-aegirine (Downs et al. in prep) were found to be identical within error: ~150 GPa. However, $Fe^{3+}O_6$ octahedra in the oxide structures of magnetite (Haavik et al. 2000), goethite (Nagai et al. 2003) and Fe_2O_3 (corundum structure, Sato and Akimoto 1979) exhibit significantly higher bulk moduli: ~220 GPa. A similar dichotomy can be observed among the structures containing $Fe^{2+}O_6$ octahedra. Non-oxide structures exhibit $Fe^{2+}O_6$ polyhedra with bulk moduli ranging from 79(33) GPa

(ferrosilite) to 123(3) GPa (hedenbergite). The NaCl-structure oxide FeO contains $Fe^{2+}O_6$ octahedra with a significantly higher bulk modulus: 153(8) GPa. Clearly, the compression behavior of the FeO_6 octahedra in the non-oxide structures is influenced by the surrounding structure.

An approach to compare the relative compressibilities of the various MO_x polyhedra in the pyroxene structures is to examine normalized polyhedral volumes versus normalized cell volumes. Such comparisons show which structural units are soft and which are stiff relative to the overall structure. Figures 11A-E contain such plots for the Fe^{3+}-containing minerals aegirine (this study) and Li-aegirine (Downs et al. in prep), the Fe^{2+}-containing mineral hedenbergite (Zhang et al. 1997), in addition to jadeite (McCarthy et al. 2007) and diopside (Thompson and Downs, accepted). Several general trends are observed. First, the $M1O_6$ polyhedra compress relatively less (i.e., they are stiffer) than the overall structure in all the minerals except diopside. This observation agrees with the oft-repeated argument that the M1 polyhedra in pyroxenes provide stiffness to the structure. Conversely, the $M2O_x$ polyhedra in all of the minerals examined compress more (i.e., they are softer) than the overall structure.

The behavior of both types of MO_x polyhedra in aegirine is comparable to that of those in jadeite. In both minerals, the NaO_6 polyhedra compress more readily than the overall structure, while the $M1^{3+}O_6$ polyhedra compress less readily. In contrast to aegirine and jadeite, hedenbergite contains M2 polyhedra (CaO_8) that are only slightly more compressible than the overall structure. Also, the normalized compression of the Fe^{2+}O6 octahedra in hedenbergite closely matches the compression of the unit cell,

whereas the $Fe^{3+}O6$ octahedra in aegirine compress relatively less than the overall structure. To understand why hedenbergite is stiffer than expected, it can be contrasted with the isostructural mineral diopside. The diopside structure exhibits some unusual compression behavior in that both the MgO_6 and the CaO_8 polyhedra compress relatively more (i.e., they are softer) than the overall structure. This indicates that non-polyhedral volumes must be acting to stiffen the structure through interpolyhedral atomic interactions. The important contrast between hedenbergite and diopside is the difference in compression behavior of the M1 octahedra, $Fe^{2+}O_6$ and MgO_6. The $Fe^{2+}O_6$ octahedra are stiffer than the MgO_6 octahedra, lending hedenbergite its anomalously high bulk modulus considering its ambient unit cell volume compared to diopside.

Acknowledgments

We would like to thank the National Science Foundation for funding our study, Compression Mechanisms of Upper Mantle Minerals, through grant No. EAR-9903104.

References

Anderson, D.L. and Anderson, O.L. (1970) The bulk modulus-volume relationship for oxides. Journal of Geophysical Research, 75, 3494–3500.

Anderson, O.L. (1972) Patterns in elastic constants of minerals important to geophysics. In: Nature of the Solid Earth, Robinson E.C. (ed) McGraw-Hill, New York, p 575–613.

Arlt, T. and Angel, R.J. (2000) Displacive phase transitions in *C*-centred clinopyroxenes:

spodumene, $LiScSi_2O_6$ and $ZnSiO_3$. Physics and Chemistry of Minerals, 27, 719–731.

Arlt T., Angel R.J., Miletich R., Armbruster T., and Peters T. (1998) High pressure $P2_1/c$-$C2/c$ phase transitions in clinopyroxenes: Influence of cation size and electronic structure. American Mineralogist, 83, 1176–1181.

Bindi, L., Downs, R.T., Harlow, G.E., Safonov, O.G., Litvin, Y.A., Perchuck, L.L., Uchida, H., and Menchetti, S. (2006) Compressibility of synthetic potassium-rich clinopyroxene: In-situ high-pressure single-crystal X-ray study. American Mineralogist, 91, 802–808.

Bridgman, P.W. (1923) The compressibility of thirty metals as a function of pressure and temperature. Proceedings of the American Academy of Arts and Sciences, 58, 165–242.

Cameron, M., Sueno, S., Prewitt, C.T., and Papike, J.J. (1973) High-temperature crystal chemistry of acmite, diopside, hedenbergite, jadeite, spodumene and ureyite. American Mineralogist, 58, 594–618.

Clark, J.R., Appleman, D.E., and Papike, J.J. (1969) Crystal-chemical characterization of clinopyroxenes based on eight new structure refinements. Mineralogical Society of America Special Paper. 2, 31-50.

Chopelas, A. and Serghiou, G. (2002) Spectroscopic evidence for pressure-induced phase transitions in diopside. Physics and Chemistry of Minerals, 29, 403–408.

Downs, R.T. (2003) Topology of the pyroxenes as a function of temperature, pressure and composition determined from the procrystal electron density. American

Mineralogist, 88, 556–566.

Downs, R.T. and Hall-Wallace, M. (2003) The American Mineralogist crystal structure database. American Mineralogist, 88, 247-250.

Downs, R.T. and Singh, A.K. (2006) Analysis of deviatoric stress from nonhydrostatic pressure on a single crystal in a diamond anvil cell: The case of monoclinic aegirine, $NaFeSi_2O_6$. Journal of Physics and Chemistry of Solids, 67, 1995–2000.

Finger, L.W. and Prince, E. (1975) A system of Fortran IV computer programs for crystal structure computations. US Bureau of National Standards Technical Note 854, 128 pp.

Gatta, G.D., Ballaran, T.B., and Iezzi, G. (2005) High-pressure X-ray and Raman study of a ferrian magnesian spodumene. Physics and Chemistry of Minerals, 32, 132–139.

Haavik, C., Stolen, S., Fjellvag, H., Hanfland, M., and Hausermann, D. (2000) Equation of state of magnetite and its high-pressure modification: Thermodynamics of the Fe-O system at high pressure. American Mineralogist, 85, 514-523.

Hattori, T., Nagai, T., Yamanaka, T., Werner, S., and Schulz, H. (2000) Single-crystal X-ray diffraction of FeGeO3 high-P clinopyroxene (*C*2/*c*) up to 8.2 GPa. American Mineralogist, 85, 1485–1491.

Hazen, R.M. and Finger, L.W. (1982) Comparative Crystal Chemistry: Temperature, Pressure, Composition and the Variation of Crystal Structure. 231 p. John Wiley & Sons, New York, New York, USA.

Hazen, R.M. and Finger, L.W. (1989) High-pressure crystal chemistry of andradite and pyrope: Revised procedures for high-pressure diffraction experiments. American

Mineralogist, 74, 352-359.

Hugh-Jones, D.A. and Angel, R.J. (1994) A compressional study of $MgSiO_3$ orthoenstatite to 8.5 GPa. American Mineralogist, 79, 405–410.

Hugh-Jones, D.A., Chopelas, A., and Angel, R.J. (1997) Tetrahedral compression in $(Mg,Fe)SiO_3$ orthopyroxenes. Physics and Chemistry of Minerals, 24, 301–310.

Ibers, J.A. and Hamilton, W.C., Eds. (1974) International Tables for X-ray Crystallography, Vol IV, 366 p. Kynoch Press, Birmingham, U.K.

King, H.E. Jr. and Finger, L.W. (1979) Diffracted beam crystal centering and its application to high-pressure crystallography. Journal of Applied Crystallography, 12, 374-378.

Mao, H.K., Bell, P.M., Shaner, J.W., and Steinberg, D.J. (1978) Specific volume measurements of Cu, Mo, Pd, and Ag and calibration of the ruby R_1 fluorescence pressure gauge from 0.06 to 1 Mbar. Journal of Applied Physics, 49, 3276-3283.

McCarthy, A.C., Downs, R.T., and Thompson, R.M. (2007) Compressibility trends of the clinopyroxenes, and in-situ high-pressure single-crystal X-ray diffraction study of jadeite. American Mineralogist, XX, XXX-XXX.

Nagai, T., Kagi, H., and Yamanaka, T. (2003) Variation of hydrogen bonded O...O distances in goethite at high pressure. American Mineralogist, 88, 1423-1427.

Nestola, F., Ballaran, T.B., Liebske, C., Bruno, M., and Tribaudino, M. (2006) High-pressure behaviour along the jadeite $NaAlSi_2O_6$-aegerine $NaFeSi_2O_6$ solid solution up to 10 GPa. Physics and Chemisty of Minerals, 33, 222-227.

Ohashi, Y. (1982) A program to calculate the strain tensor from two sets of unit-cell

parameters. In: Hazen, R.M. and Finger, L.W. (eds) Comparative crystal chemistry. John Wiley & Sons, New York, New York, 231 pp.

Origlieri, M.J., Downs, R.T., Thompson, R.M., Pommier, C.J.S., Denton, M.B., and Harlow, G.E. (2003) High-pressure crystal structure of kosmochlor, $NaCrSi_2O_6$, and systematics of anisotropic compression in pyroxenes. American Mineralogist, 88, 1025-1032.

Redhammer, G.J., Amthauer, G., Lottermoser, W., and Treutmann, W. (2000) Synthesis and structural properties of clinopyroxenes of the hedenbergite $CaFeSi_2O_6$-aegerine $NaFeSi_2O_6$ solid-solution series. European Journal of Mineralogy, 12, 105-120.

Robinson, K., Gibbs, G.V., and Ribbe, P.H. (1971) Quadratic elongation – quantitative measure of distortion in coordination polyhedra. Science, 172, 567-570.

Sato, Y. and Akimoto, S. (1979) Hydrostatic compression of 4 corundum-type compounds: α-Al_2O_3, V_2O_3, Cr_2O_3, and α-Fe_2O_3. Journal of Applied Physics, 50, 5285-5291.

Shannon, R.D. (1976) Revised effective ionic-radii and systematic studies of interatomic distances in halides and chalcogenides. Acta Crystallographica, A32, 751-767.

Thompson, J.B. (1970) Geometric possibilities for amphibole structures: model biopyriboles. American Mineralogist, 55, 292-293.

Thompson, R.M. and Downs, R.T. (2004) Model pyroxenes II: Structural variation as a function of tetrahedral rotation. American Mineralogist, 89, 614–628.

Thompson, R.M. and Downs, R.T. (accepted) The crystal structure of diopside at pressure to 10 GPa. American Mineralogist, XX, XXX-XXX.

Thompson, R.M., Downs, R.T., and Redhammer, G.J. (2005) Model pyroxenes III: Volume of *C*2/*c* pyroxenes at mantle *P*, *T*, and *x*. American Mineralogist, 90, 1840–1851.

Tribaudino, M., Prencipe, M., Bruno, M., and Levy, D. (2000) High-pressure behaviour of Ca-rich *C*2/*c* clinopyroxenes along the join diopside-enstatite ($CaMgSi_2O_6$-$Mg_2Si_2O_6$). Physics and Chemistry of Minerals, 27, 656–664.

Yang, H., Finger, L.W., Pamela, C.G., Prewitt, C.T., and Hazen, R.T. (1999) A new pyroxene structure at high pressure: Single-crystal X-ray and Raman study of the *Pbcn*-$P2_1cn$ phase transition in protopyroxene. American Mineralogist, 84, 245–256.

Zhang, L., Ahsbahs, H., Hafner, S.S., and Kutoglu, A. (1997) Single-crystal compression and crystal structure of clinopyroxene up to 10 GPa. American Mineralogist, 82, 245–258.

Figure 1. Oriented unit strain ellipsoid superimposed on the aegirine structure viewed down **b**. M2 (Na) is illustrated as a sphere. The most compressible direction in aegirine is 55.9º from **c**.

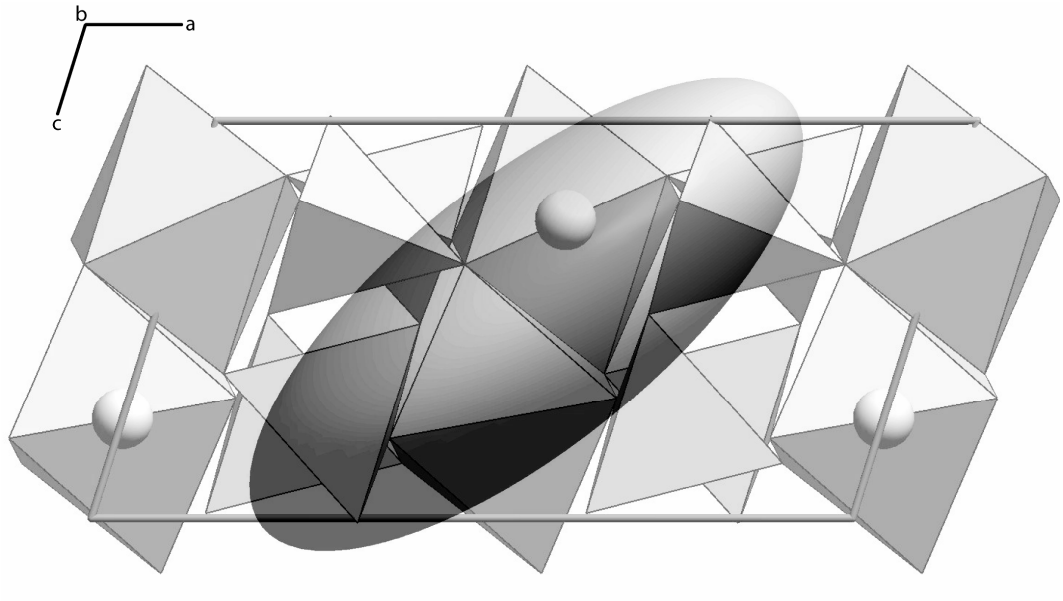

Figure 2. Illustration of the aegirine structure and oxygen atom nomenclature around M2 (Na). The oxygen atoms that bridge the SiO_4 tetrahedra, O3, are numbered 1-4 according to their position relative to M2 (Downs 2003).

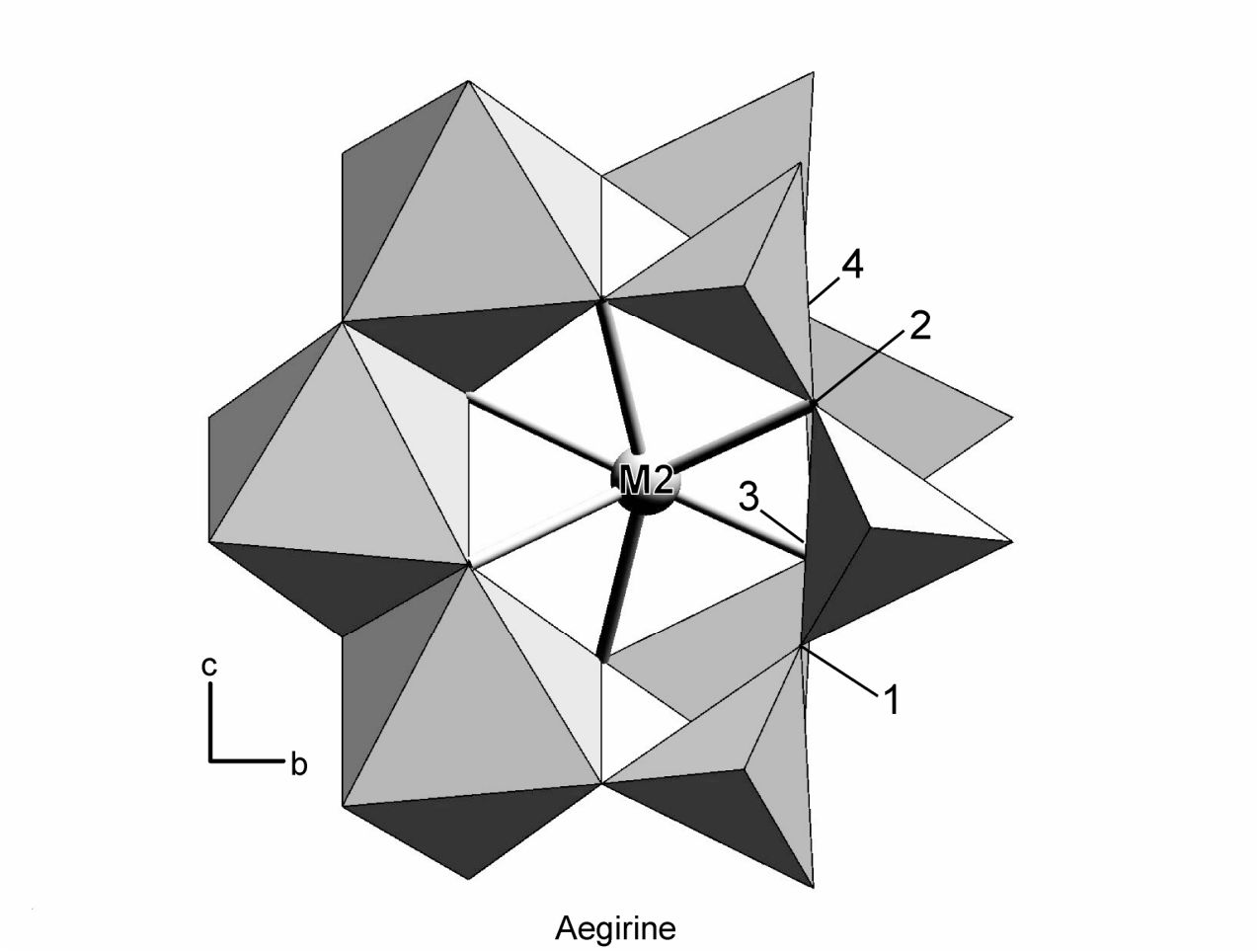

Figure 3. Superimposed images of the aegirine structure around M2 at ambient pressure and at 10.82 GPa. View is along a*. For clarity, only the top T-chain is shown (contrast with Fig. 2). The structure with the more-rotated tetrahedra is at 10.82 GPa. The (unbonded) sympathetic distance M2-$O3_1$ is indicated with the dashed line. Note how this sympathetic distance decreases visibly with pressure, whereas the bonded M2-$O3_2$ distance decreases little. These changes are brought about primarily by the rotation of the SiO_4 tetrahedra.

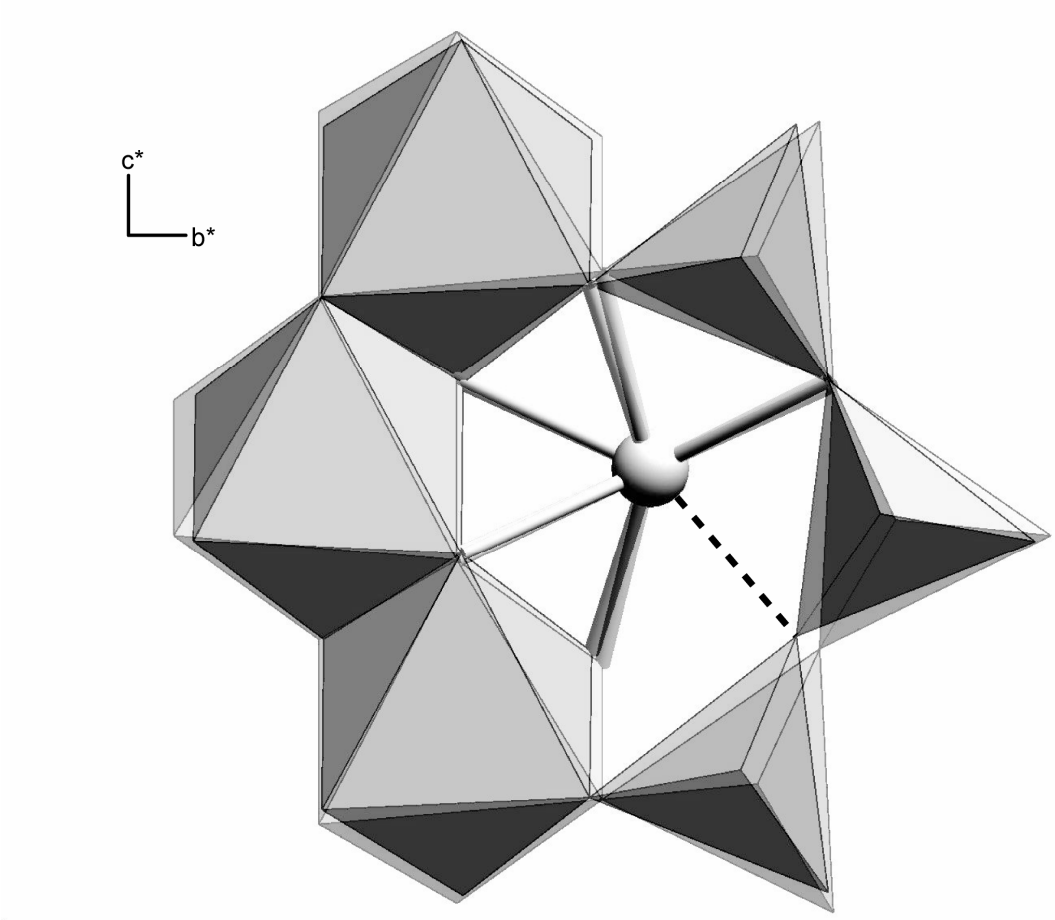

Figure 4. Unit cell volume as a function of pressure for aegirine. Data are fit with a third-order Birch-Murnaghan equation, with V_0 = 429.40(9) Å^3, K_0 = 117(1) GPa, and $K_0^{'}$ = 3.2(2). Errors in *P* and *V* are significantly smaller than the symbols used.

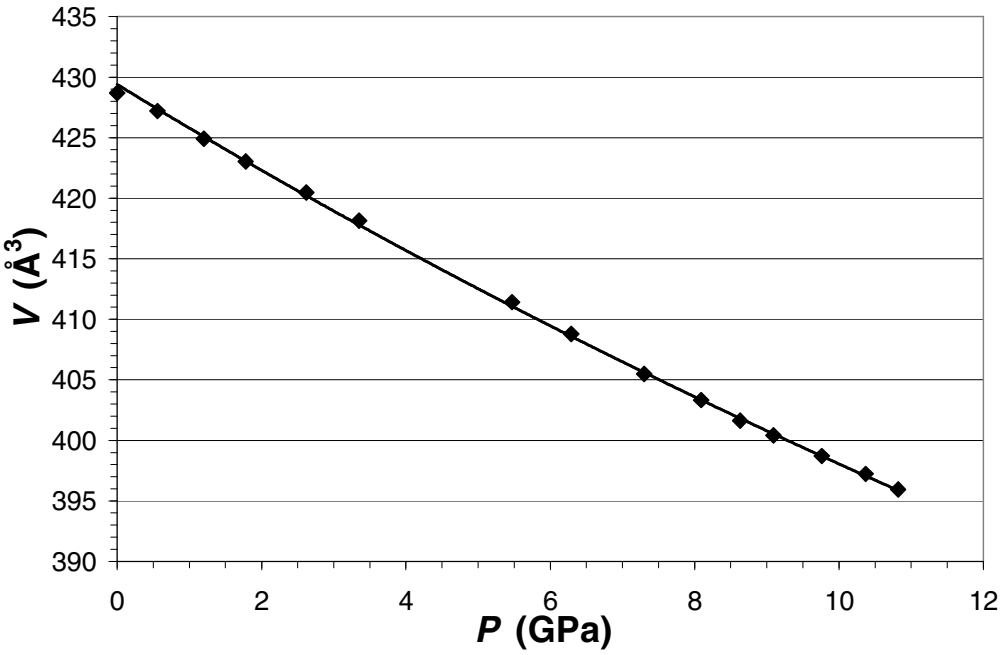

Figure 5. Variation of Na–O distances in aegirine with pressure at room temperature. Na–$O3_{1,4}$ is the only unbonded pair over the pressure range examined in this study. At a pressure of 17.9 GPa, the linearly extrapolated Na–$O3_{1,4}$ distance is the same as the Na–$O3_{2,3}$ distance at ambient pressure. At this or a lesser pressure, Na–$O3_{1,4}$ bonds may form, making Na 8-coordinated and constituting a *C*2/*c* → *C*2/*c* bonding transition.

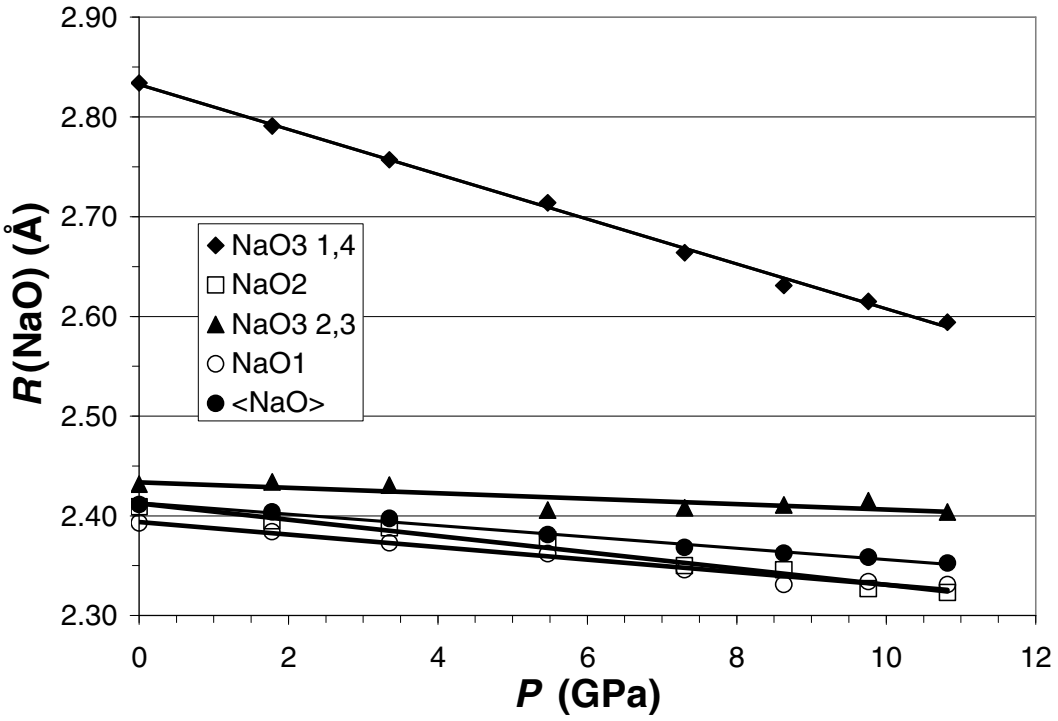

Figure 6. Variation of Fe–O distances in aegirine with pressure at room temperature.

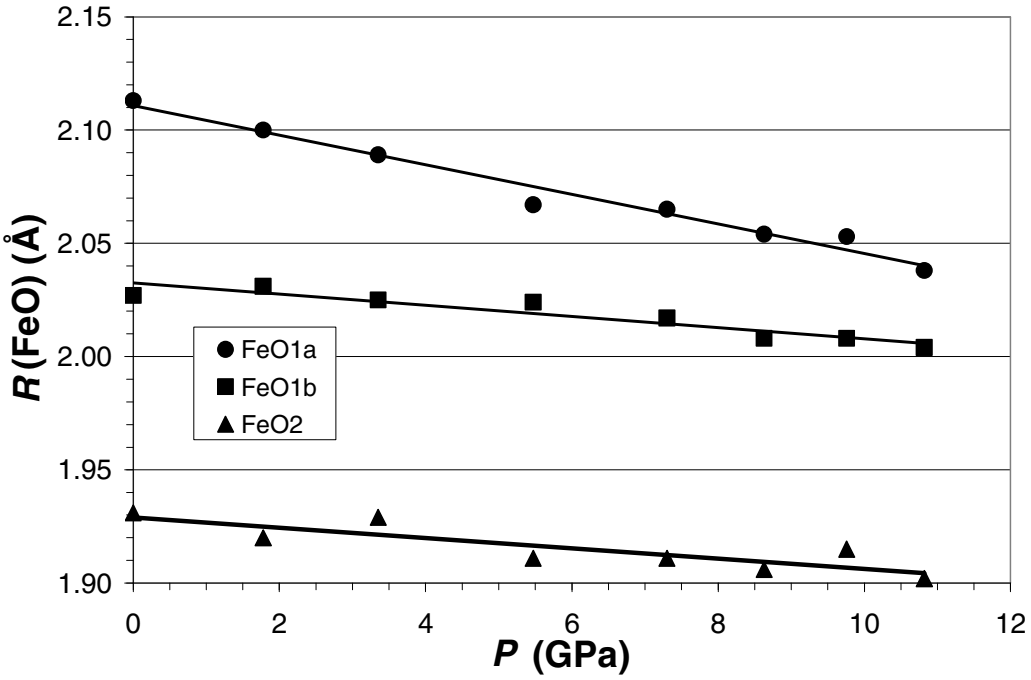

Figure 7. Variation of ∠O3-O3-O3 in the Na-clinopyroxenes aegirine, jadeite and kosmochlor, with pressure at room temperature. Jadeite data from McCarthy et al. (2007); kosmochlor data from Origlieri et al. (2003). Estimated errors in *P* are significantly smaller than the symbols used.

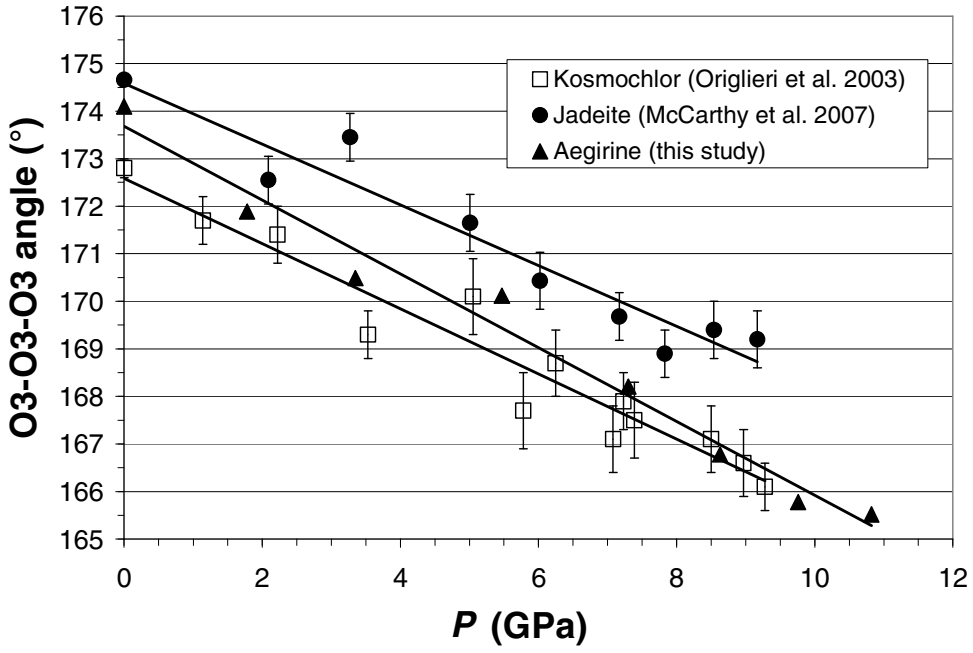

Figure 8. Unit-cell volume plotted against M1 cation radius (Shannon 1976) for 22 ambient condition *C*2/*c* pyroxenes from the literature. Modified after Thompson et al. (2005). A linear fit to all the data yields $R^2 = 0.92$.

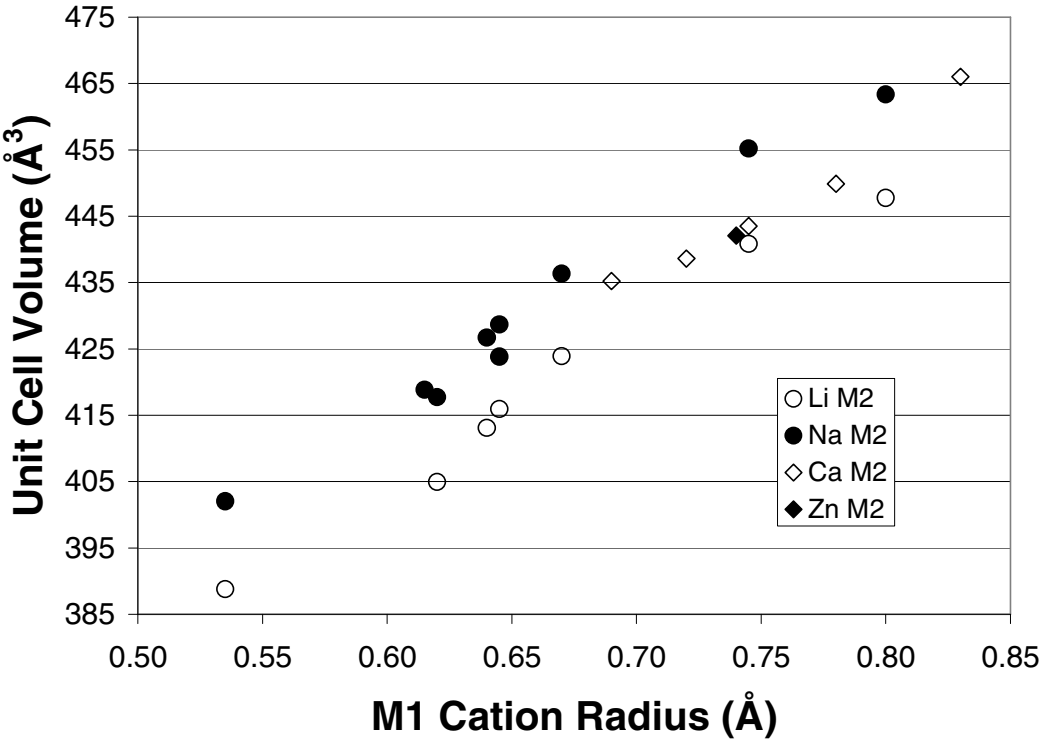

Figure 9. (A) M1 cation radius versus bulk modulus in $C2/c$ and $P2_1/c$ silicate pyroxenes from the literature. The two parameters are poorly correlated, with a linear fit yielding $R^2 = 0.48$. However, the data can be divided into two trends based on M2 bonding geometry. The two trends are identified and labeled in (B). The correlations for each population become much better than the fit to the entire population. The population of "sympathetic" pyroxenes is shifted down in this plot relative to the "antipathetic" pyroxenes due to the stiffening effect of the antipathetic M2-O3 bonds (see McCarthy et al. (2007) for a detailed explanation of antipathetic and sympathetic bonds in pyroxene structures).

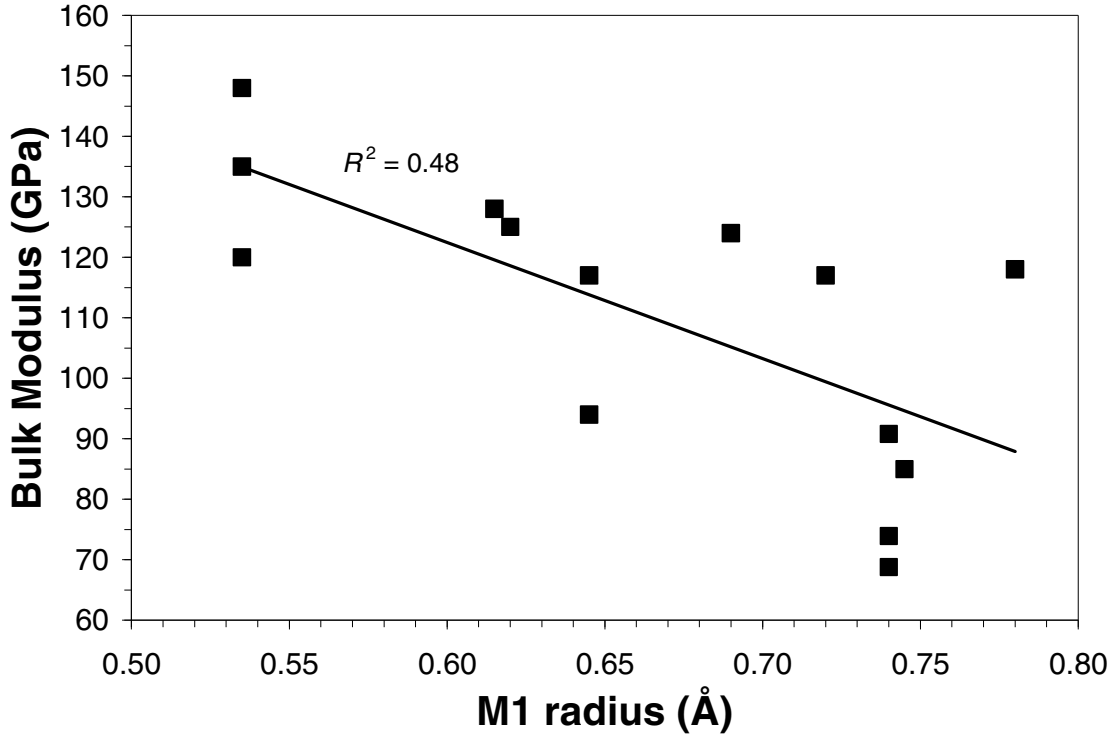

Figure 9A

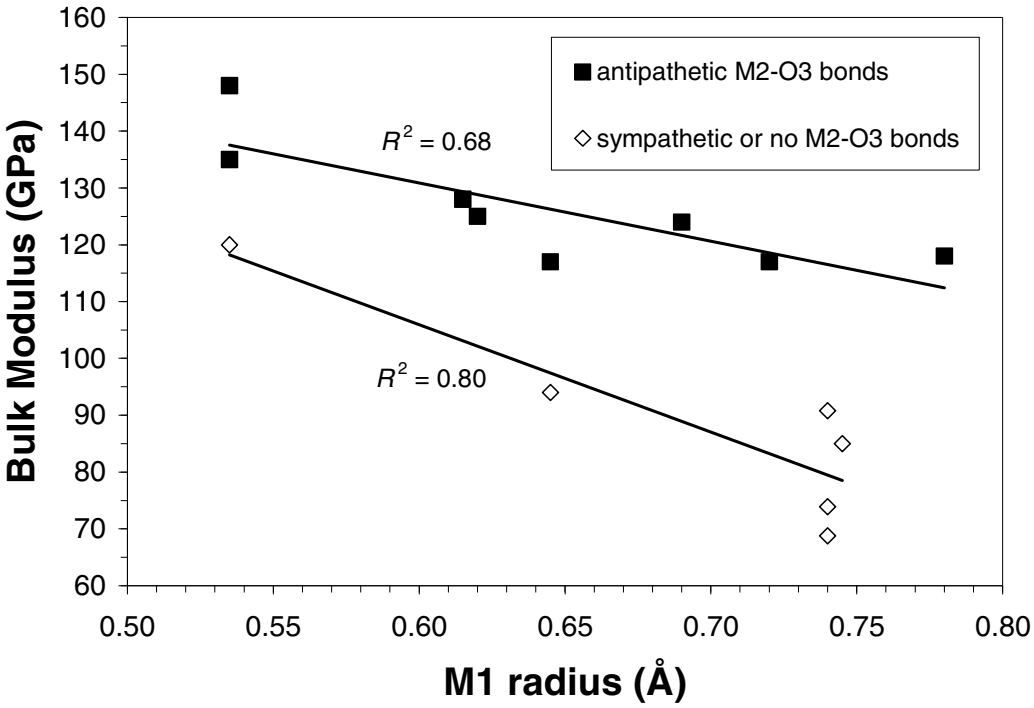
Bulk Modulus (GPa)
M1 radius (Å)
antipathetic M2-O3 bonds
sympathetic or no M2-O3 bonds
R^2 = 0.68
R^2 = 0.80
160
150
140
130
120
110
100
90
80
70
60
0.50
0.55
0.60
0.65
0.70
0.75
0.80

Figure 9B

Figure 10. (A) M1 polyhedral volume versus bulk modulus in $C2/c$ and $P2_1/c$ silicate pyroxenes from the literature. The two parameters are poorly correlated, with a linear fit yielding $R^2 = 0.48$. However, the data can be divided into two trends based on M2 bonding topology. The two trends are identified and labeled in (B). The correlations for each population become much better than the fit to the entire population. The population of "sympathetic" pyroxenes is shifted down in this plot relative to the "antipathetic" pyroxenes due to the stiffening effect of the antipathetic M2-O3 bonds. (C) After correcting sympathetic bulk moduli using the empirical model of McCarthy et al. (2007), all examined pyroxenes fall on a trend with $R^2 = 0.66$.

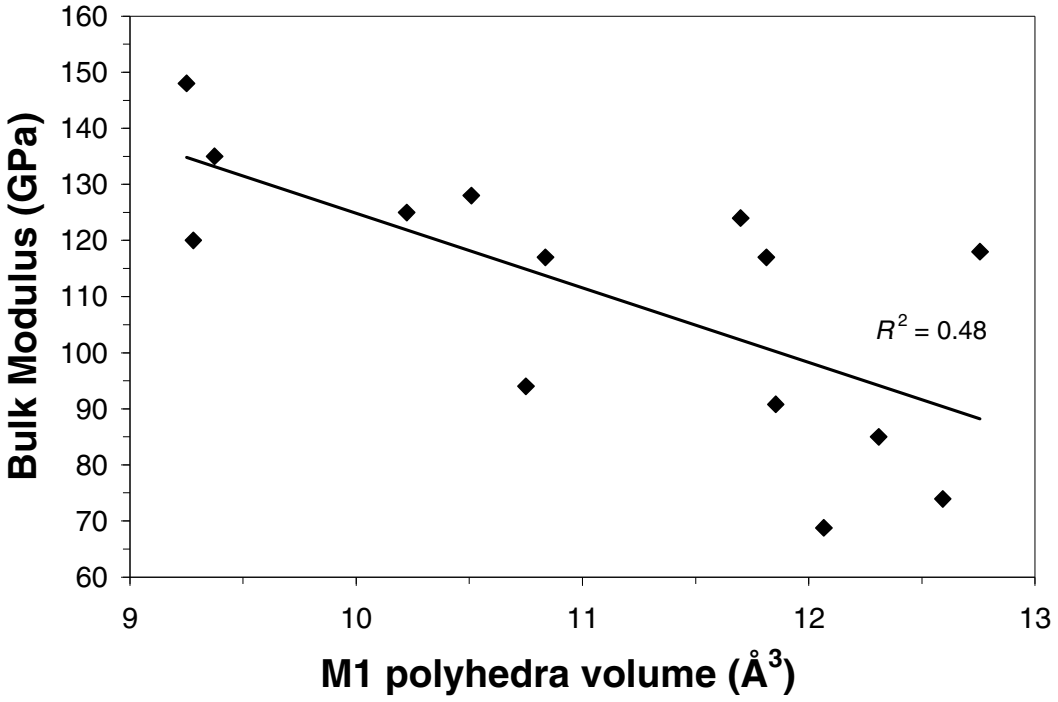

Figure 10A

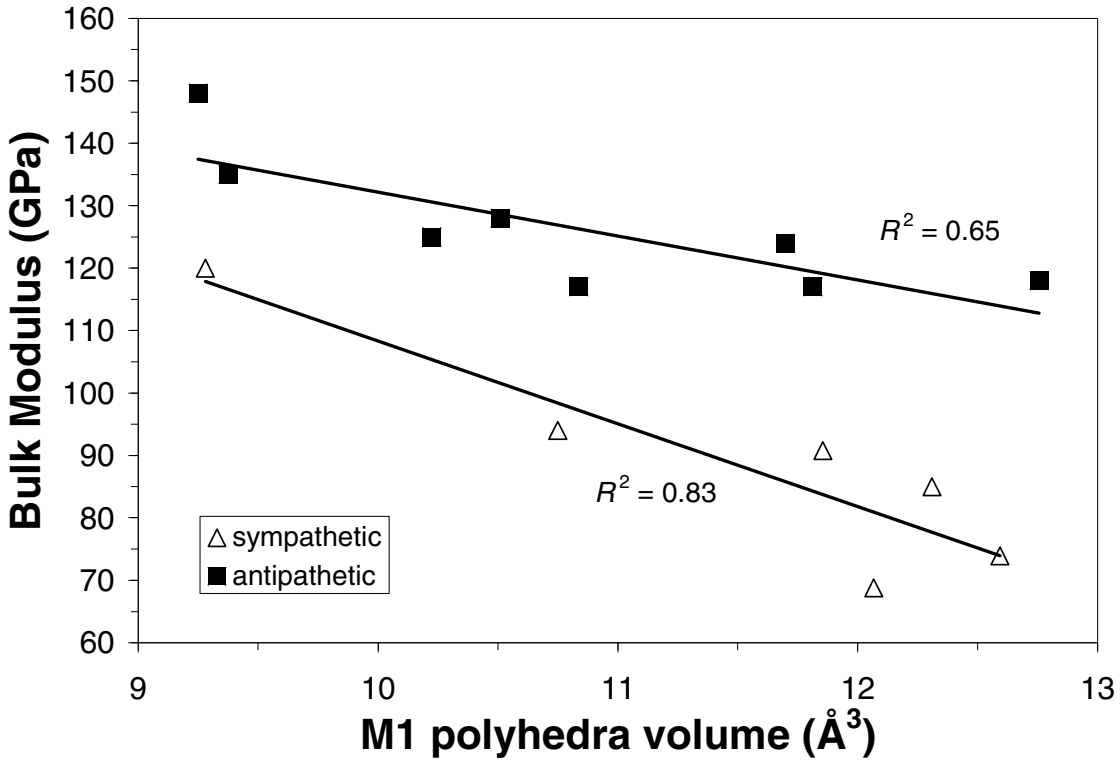
160
150
140
130
120
110
100
90
80
70
60
Bulk Modulus (GPa)
9
10
11
12
13
M1 polyhedra volume (Å3)
R2 = 0.65
R2 = 0.83
sympathetic
antipathetic

Figure 10B

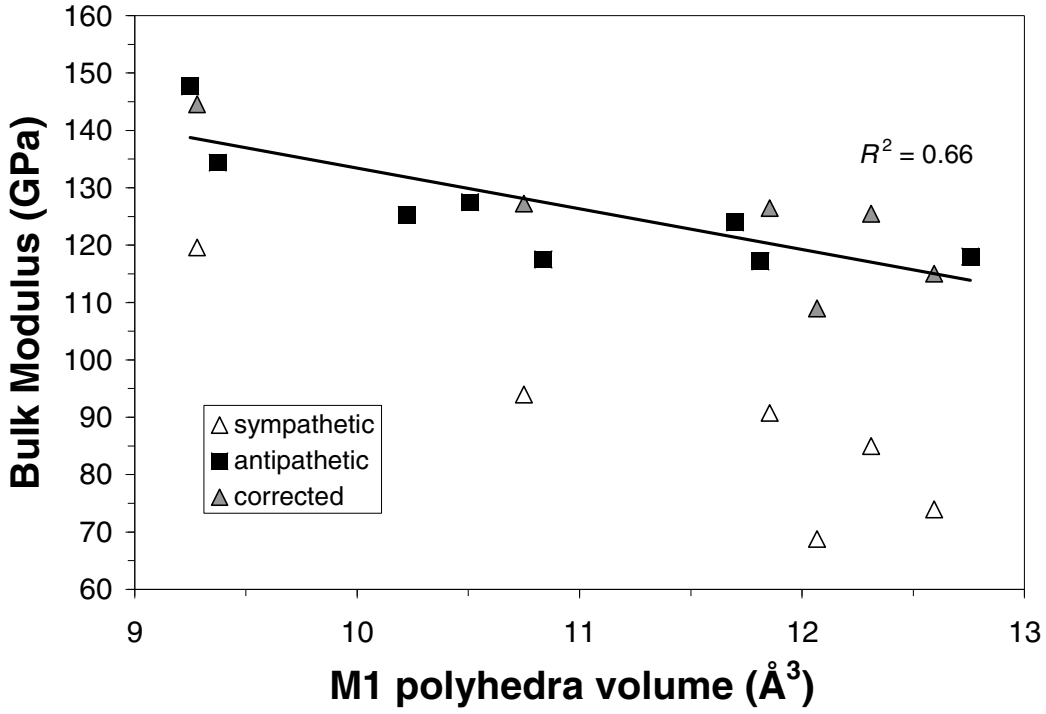
160
150
140
130
120
110
100
90
80
70
60
9
10
11
12
13
Bulk Modulus (GPa)
M1 polyhedra volume (Å3)
R2 = 0.66
sympathetic
antipathetic
corrected

Figure 10C

Figure 11. Normalized unit-cell and M polyhedral volumes from several clinopyroxenes studied at high pressures. (A) aegirine (this study); (B) jadeite (McCarthy et al. 2007); (C) Li-aegirine (Downs et al. in prep); (D) hedenbergite (Zhang et al. 1997); (E) diopside (Thompson et al. submitted).

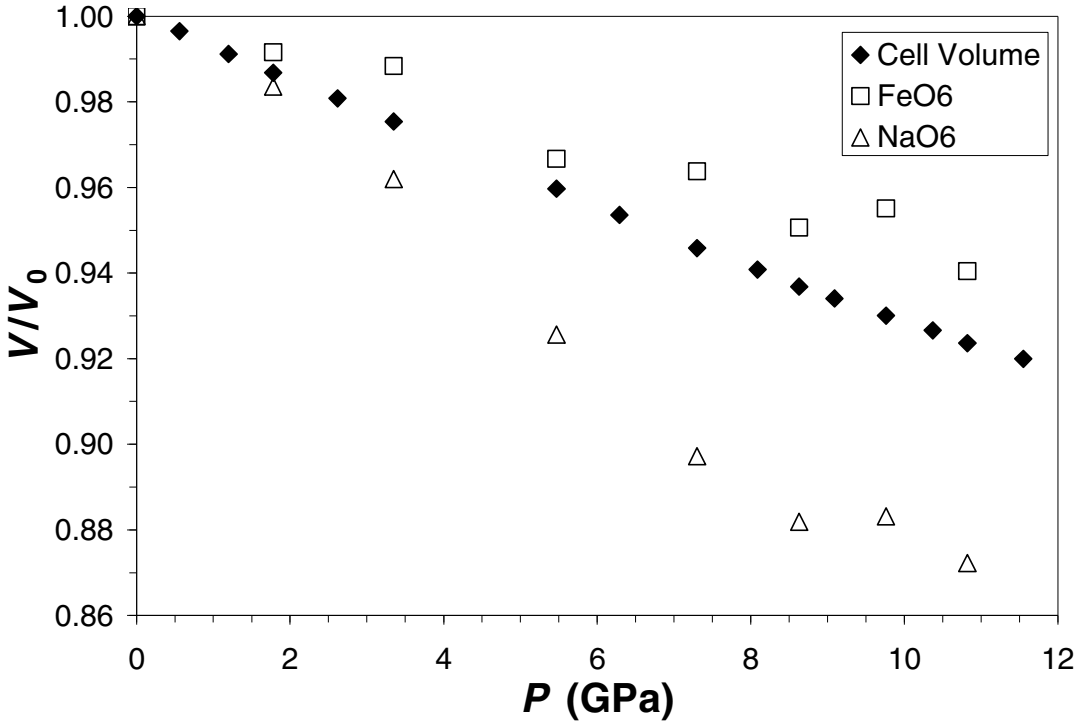

Figure 11A

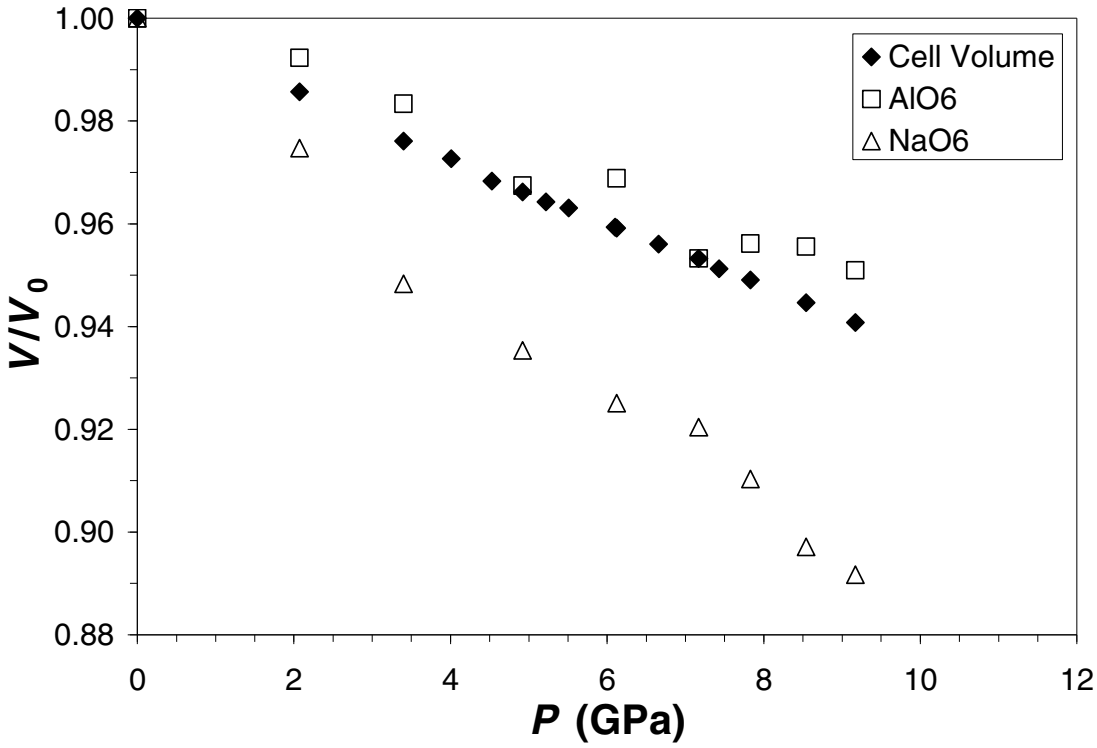
1.00
0.98
0.96
0.94
0.92
0.90
0.88
V/V0
0
2
4
6
8
10
12
P (GPa)
Cell Volume
AlO6
NaO6

Figure 11B

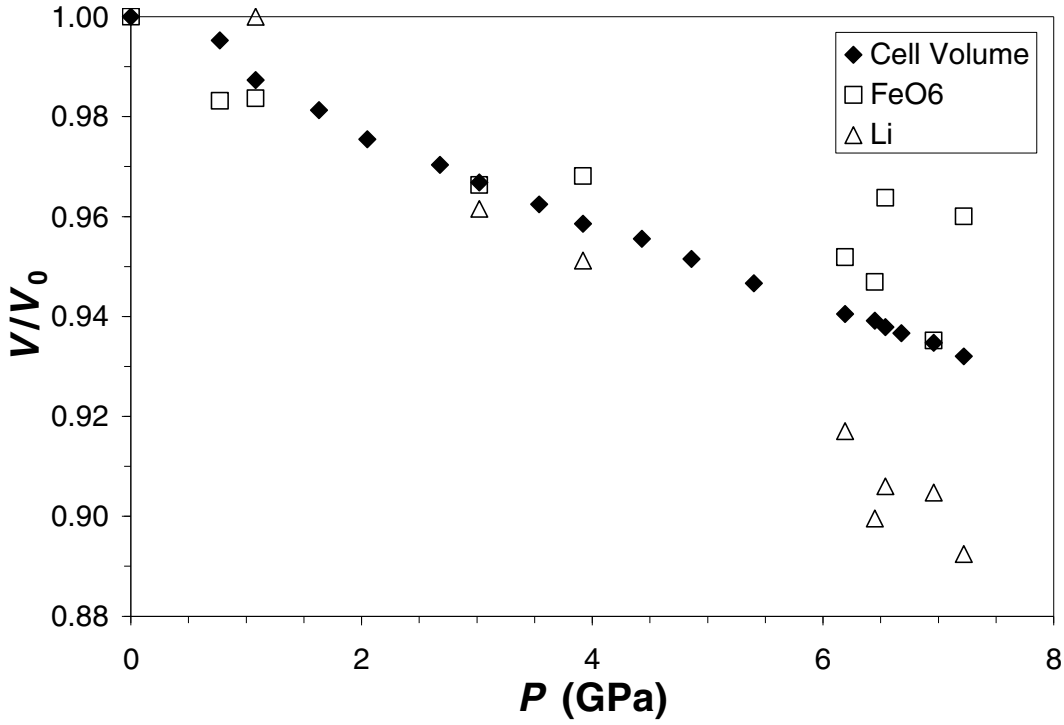

Figure 11C

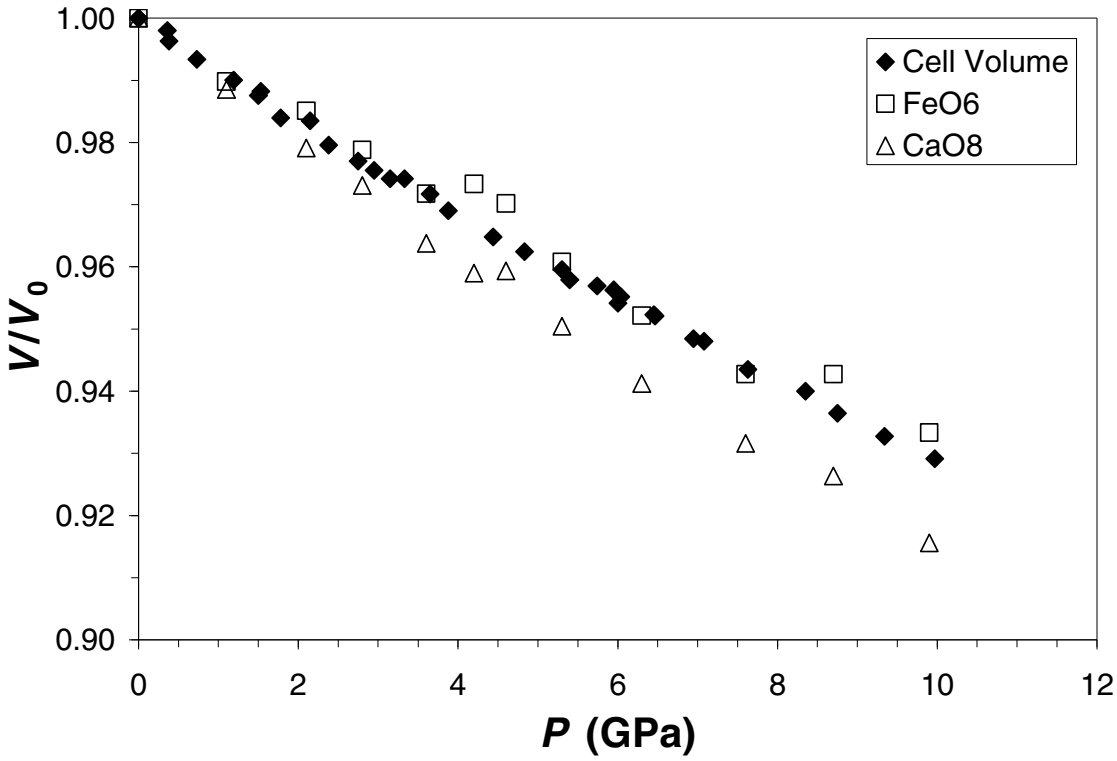
1.00
0.98
0.96
0.94
0.92
0.90
V/V0
0
2
4
6
8
10
12
P (GPa)
Cell Volume
FeO6
CaO8

Figure 11D

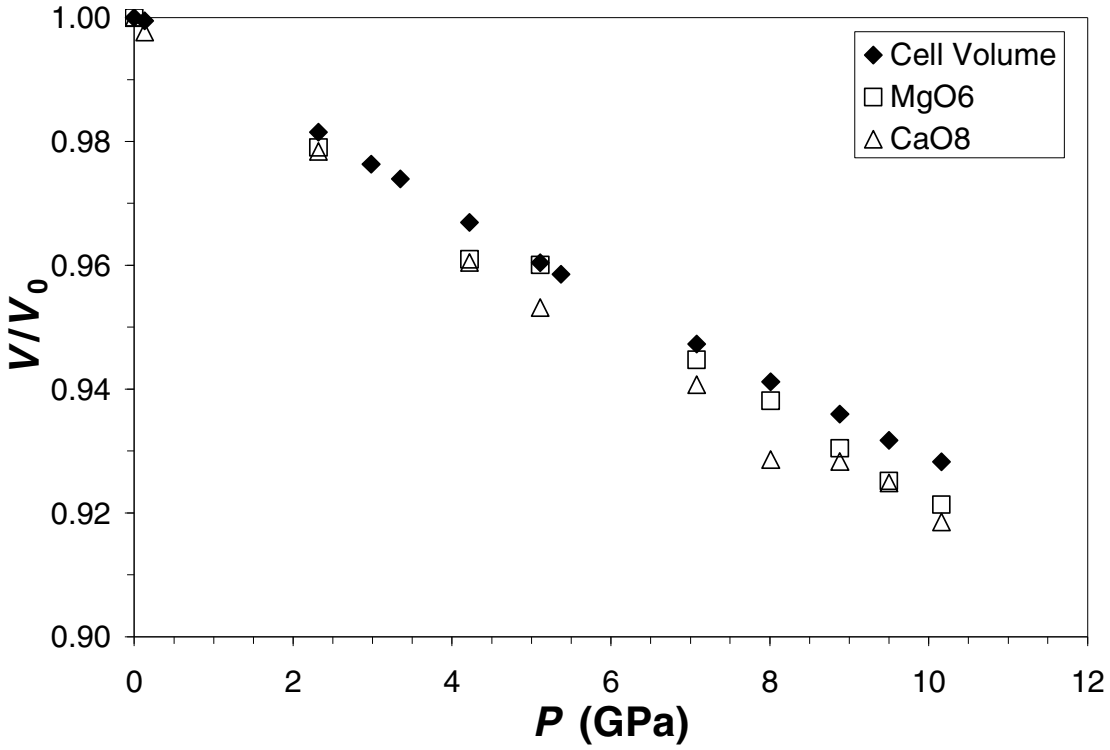
1.00
0.98
0.96
0.94
0.92
0.90
V/V0
0
2
4
6
8
10
12
P (GPa)
Cell Volume
MgO6
CaO8

Figure 11E

Table 1. Aegirine unit-cell data as a function of pressure

Run	*P* (GPa)	*a* (Å)	*b* (Å)	*c* (Å)	*β* (°)	*V* (Å^3)
P0*	0.0001	9.6539(2)	8.7928(2)	5.2935(2)	107.436(2)	428.69(2)
P1	0.56(3)	9.6406(3)	8.7825(5)	5.2871(2)	107.386(3)	427.20(3)
P2	1.20(3)	9.6221(4)	8.7644(4)	5.2778(2)	107.318(3)	424.91(3)
P3*	1.78(3)	9.6067(3)	8.7501(4)	5.2698(2)	107.258(3)	423.03(2)
P4	2.62(3)	9.5858(4)	8.7307(5)	5.2585(2)	107.171(4)	420.47(3)
P5*	3.35(3)	9.5667(4)	8.7128(5)	5.2484(2)	107.095(4)	418.14(3)
P7*	5.47(3)	9.5148(3)	8.6568(3)	5.2188(3)	106.844(4)	411.42(3)
P7a	6.29(3)	9.4948(2)	8.6364(3)	5.2062(2)	106.757(3)	408.79(2)
P9*	7.30(3)	9.4711(2)	8.6068(3)	5.1915(1)	106.633(2)	405.48(2)
P11	8.09(3)	9.4551(3)	8.5885(4)	5.1815(2)	106.551(3)	403.33(2)
P12*	8.63(3)	9.4426(3)	8.5727(4)	5.1740(2)	106.482(3)	401.62(2)
P13	9.09(3)	9.4342(4)	8.5631(6)	5.1677(3)	106.439(4)	400.41(3)
P14*	9.76(3)	9.4220(2)	8.5480(4)	5.1597(2)	106.371(3)	398.71(2)
P15	10.37(3)	9.4125(3)	8.5342(5)	5.1526(3)	106.314(4)	397.23(3)
P17*	10.82(3)	9.4038(3)	8.5221(5)	5.1465(3)	106.256(4)	395.95(3)
P18	11.55(3)	9.3931(4)	8.5065(6)	5.1394(3)	106.187(4)	394.37(4)

Note: Space group = *C*2/*c*

* Intensity data collected at this pressure

Table 2. Structural parameters for aegirine in air at room conditions

atom	*x*	*y*	*z*	B_{eq}(Å^2)	β_{11}	β_{22}	β_{33}	β_{12}	β_{13}	β_{23}
NaM2	0	0.2992(1)	¼	1.022(19)	0.00364(14)	0.00275(14)	0.00714(40)	0	-0.00050(19)	0
FeM1	0	0.89878(5)	¼	0.407(8)	0.00119(5)	0.00128(5)	0.00404(14)	0	0.00057(6)	0
Si	0.29072(5)	0.08945(6)	0.23561(8)	0.370(8)	0.00106(5)	0.00132(6)	0.00344(16)	-0.00012(5)	0.00066(8)	-0.00008(9)
O1	0.1143(1)	0.0786(1)	0.1376(2)	0.508(20)	0.00124(12)	0.00187(16)	0.00508(41)	-0.00018(12)	0.00069(19)	-0.00008(21)
O2	0.3588(1)	0.2558(2)	0.3007(2)	0.674(21)	0.00238(15)	0.00170(16)	0.00722(45)	-0.00059(12)	0.00164(21)	-0.00062(21)
O3	0.3520(1)	0.0078(1)	0.0120(3)	0.585(18)	0.00145(12)	0.00241(14)	0.00510(40)	0.00001(13)	0.00081(18)	-0.00077(24)

Note: Space group = *C*2/*c*

Table 3. Structural parameters for aegirine as a function of pressure

P (GPa)	0.0001	1.78	3.35	5.47	7.3	8.63	9.76	10.82
	P0	P3	P5	P7	P9	P12	P14	P17
obs refl	476	220	214	210	214	217	208	200
total refl	624	320	312	295	294	302	298	292
*p**	0.004	0.035	0.030	0.040	0.030	0.034	0.037	0.035
R_w	0.012	0.047	0.043	0.051	0.041	0.047	0.047	0.046
Fe *y*	0.89878(5)	0.8997(2)	0.9005(2)	0.9006(2)	0.9014(2)	0.9015(2)	0.9018(2)	0.9021(2)
B	0.407(8)	0.64(4)	0.65(4)	0.58(4)	0.64(3)	0.60(4)	0.82(4)	0.74(4)
Na *y*	0.2992(1)	0.3002(5)	0.3011(5)	0.3029(5)	0.3044(4)	0.3048(5)	0.3050(5)	0.3059(5)
B	10.02(2)	10.08(8)	10.08(8)	10.11(8)	10.09(7)	0.98(7)	10.17(8)	10.07(8)
Si *x*	0.29072(5)	0.2904(2)	0.2907(2)	0.2909(3)	0.2911(2)	0.2911(2)	0.2911(2)	0.2916(2)
y	0.08945(6)	0.0901(3)	0.0908(3)	0.0909(2)	0.0917(2)	0.0920(3)	0.0918(3)	0.0922(3)
z	0.23561(8)	0.2355(4)	0.2356(4)	0.2366(5)	0.2365(4)	0.2367(4)	0.2368(4)	0.2377(3)
B	0.370(8)	0.61(4)	0.57(4)	0.54(4)	0.59(3)	0.60(4)	0.77(4)	0.69(4)
O1 *x*	0.1143(1)	0.1150(7)	0.1150(6)	0.1141(7)	0.1146(6)	0.1135(6)	0.1149(6)	0.1141(6)
y	0.0786(1)	0.0792(6)	0.0800(6)	0.0801(6)	0.0821(5)	0.0827(6)	0.0824(7)	0.0822(7)
z	0.1376(2)	0.1397(10)	0.1398(9)	0.1414(12)	0.1416(9)	0.1411(10)	0.1412(9)	0.1414(9)
B	0.51(2)	0.80(9)	0.68(8)	0.67(9)	0.64(7)	0.70(8)	0.78(8)	0.72(8)
O2 *x*	0.3588(1)	0.3595(7)	0.3574(6)	0.3573(7)	0.3574(6)	0.3567(6)	0.3562(6)	0.3573(6)
y	0.2558(1)	0.2567(7)	0.2578(6)	0.2602(6)	0.2607(5)	0.2617(6)	0.2615(7)	0.2619(7)
z	0.3007(2)	0.3028(10)	0.3052(10)	0.3081(1)	0.3135(9)	0.3144(10)	0.3186(9)	0.3186(9)
B	0.67(2)	0.90(9)	0.82(9)	0.77(9)	0.83(8)	0.95(9)	0.94(9)	0.96(9)
O3 *x*	0.3520(1)	0.3527(7)	0.3532(7)	0.3548(7)	0.3549(5)	0.3558(6)	0.3557(6)	0.3564(6)
y	0.0078(1)	0.0107(6)	0.0125(6)	0.0130(6)	0.0156(5)	0.0175(6)	0.0188(7)	0.0192(7)
z	0.0120(3)	0.0110(10)	0.0101(10)	0.0094(1)	0.0058(10)	0.0044(10)	0.0032(9)	0.0032(10)
B	0.59(2)	0.74(9)	0.76(8)	0.72(9)	0.78(7)	0.59(8)	0.98(8)	0.86(9)

Note: $x_{Fe} = x_{Na} = 0$; $z_{Fe} = z_{Na} = ¼$.
* Weights computed by $\omega = [\sigma_F^2 + (pF)^2]^{-1}$

Table 4. Selected bond lengths (Å), volumes (Å^3), and angles (°) from structure refinements

P (GPa)	0.0001$^{\delta}$	1.78	3.35	5.47	7.3	8.63	9.76	10.82
	P0	P3	P5	P7	P9	P12	P14	P17
R(SiO1)	1.628(1)	1.612(6)	1.609(6)	1.612(7)	1.604(5)	1.611(6)	1.596(6)	1.604(6)
R(SiO2)	1.599(1)	1.598(6)	1.588(6)	1.597(6)	1.589(5)	1.588(6)	1.586(6)	1.582(6)
R(SiO3a)	1.639(1)	1.631(6)	1.625(5)	1.628(6)	1.625(5)	1.626(5)	1.620(5)	1.621(5)
R(SiO3b)	1.644(1)	1.652(6)	1.655(6)	1.645(6)	1.640(5)	1.641(5)	1.638(5)	1.635(6)
<*R*(SiO)>	1.627	1.623	1.619	1.620	1.615	1.616	1.610	1.611
V(SiO_4)	2.2013	2.1836	2.1694	2.1748	2.1524	2.1595	2.1337	2.1364
R(NaO1)	2.393(1)	2.384(6)	2.372(6)	2.362(6)	2.346(5)	2.331(6)	2.334(6)	2.331(7)
R(NaO2)	2.409(1)	2.395(5)	2.388(5)	2.376(7)	2.350(5)	2.346(5)	2.327(5)	2.323(5)
R(NaO3c)	2.432(1)	2.434(7)	2.431(7)	2.406(7)	2.408(6)	2.411(7)	2.415(7)	2.404(7)
R(NaO3d)	2.834(1)	2.791(6)	2.757(6)	2.713(6)	2.664(5)	2.631(5)	2.612(6)	2.594(6)
diff	0.402	0.357	0.326	0.307	0.256	0.220	0.197	0.190
<*R*(NaO)>	2.411	2.404	2.397	2.381	2.368	2.363	2.359	2.353
R(FeO1a)	2.113(1)	2.100(6)	2.089(5)	2.067(5)	2.065(4)	2.054(5)	2.053(5)	2.038(6)
R(FeO1b)	2.027(1)	2.031(5)	2.025(5)	2.024(7)	2.017(5)	2.008(5)	2.008(5)	2.004(5)
R(FeO2)	1.931(1)	1.920(6)	1.929(5)	1.911(6)	1.911(4)	1.906(5)	1.915(5)	1.902(6)
<*R*(FeO)>	2.024	2.017	2.015	2.001	1.998	1.989	1.992	1.982
V(FeO_6)	10.8534	10.7621	10.7272	10.4915	10.4607	10.3173	10.3665	10.2074
Si-O3-Si	139.37(9)	139.6(5)	138.3(4)	137.3(4)	137.0(3)	136.1(4)	135.9(4)	135.6(4)
O3-O3-O3	174.1(1)	171.9(5)	170.5(4)	170.1(4)	168.2(4)	166.8(5)	165.8(5)	165.5(5)

Notes: $^{\delta}$Structure at 0.0001 GPa was refined with anisotropic temperature factors

The O3a in SiO3a is at [0.352,0.008,0.012]

The O3c in NaO3c is at [0.148,0.508,0.488]

The O1a in FeO1a is at [0.114,1.079,0.138]

diff: length difference between the shortest and longest reported Na-O bonds

Table 5. Bulk modulus, cation radius and polyhedral volume data used to construct Figures 9 and 10.

Material	S.G.	K_0* (GPa)	M1	M1 rad (Å)	M1 poly vol (Å^3)	*P*** (GPa)
$LiAlSi_2O_6$	*C*2/*c*	148(3)	Al	0.535	9.250	0.0001
$NaAlSi_2O_6$	*C*2/*c*	134.4(3)	Al	0.535	9.374	0.0001
$NaGaSi_2O_6$	*C*2/*c*	125(1)	Ga	0.620	10.224	0.0001
$NaCrSi_2O_6$	*C*2/*c*	127.5(3)	Cr	0.615	10.509	0.0001
$NaFeSi_2O_6$	*C*2/*c*	117.5(7)	Fe	0.645	10.837	0.0001
$CaMgSi_2O_6$	*C*2/*c*	117.2(3)	Mg	0.720	11.813	0.0001
$CaFeSi_2O_6$	*C*2/*c*	118.0(4)	Fe	0.780	12.757	0.0001
$CaNiSi_2O_6$	*C*2/*c*	124.0(4)	Ni	0.690	11.700	0.0001
$ZnSiO_3$	*C*2/*c*	74(1)	Zn	0.740	12.593	0.0001
$ZnSiO_3$	HP *C*2/*c*	91(3)	Zn	0.740	11.855	0.0001
$LiAlSi_2O_6$	*P*2$_1$/*c*	120(1)	Al	0.535	9.280	0.0001
$LiFeSi_2O_6$	*P*2$_1$/*c*	94(1)	Fe	0.645	10.750	3.34
$LiScSi_2O_6$	*P*2$_1$/*c*	85(2)	Sc	0.745	12.310	1.08
$ZnSiO_3$	*P*2$_1$/*c*	69(1)	Zn	0.740	12.067	0.66

Notes: *K'_0 constrained to 4.0. ** minimum pressure of stability of the phase

Table 6. Compressibilities of $Fe^{2+}O_6$ and $Fe^{3+}O_6$ octahedra in various structures

Material	Ideal Formula	FeO_6 K_0 (GPa)	M	V_0	<M1-O>	Bulk K_0 (GPa)	Reference
Andradite	$Ca_3Fe^{3+}_2(SiO_4)_3$	154(4)	Fe^{3+}	11.287	52.038	159(2)	Hazen and Finger (1989)
Aegirine	$NaFe^{3+}Si_2O_6$	152(3)	Fe^{3+}	10.853	42.024	117(1)	This study
Li-Aegirine	$LiFe^{3+}Si_2O_6$	139(12)	Fe^{3+}	10.874	02.025	94(1)	Downs et al., in prep
Magnetite	$Fe^{2+}Fe^{3+}_2O_4$	214(4)	$Fe^{3+/2+}$	11.607	82.059	217(2)	Haavik et al. (2000)
Goethite	$Fe^{3+}O(OH)$	210(24)	Fe^{3+}	10.847	02.032	111(2)	Nagai et al. (2003)
Fe_2O_3 (corundum)	$Fe^{3+}_2O_3$	231(10)	Fe^{3+}	n/r	n/r	231(10)	Sato and Akimoto (1979)
Hedenbergite	$CaFe^{2+}Si_2O_6$	123(3)	Fe^{2+}	12.766	12.128	118(1)	Zhang et al. (1997)
FeO (NaCl)	$Fe^{2+}O$	153(8)	Fe^{2+}	n/r	n/r	153(8)	Hazen and Finger (1982)
$FeGeO_3$	$Fe^{2+}Ge^{4+}O_3$	98(5)	Fe^{2+}	12.787	22.134	107(2)	Hattori et al. (2000)
Ferrosilite	$Fe^{2+}SiO_3$	79(33)	Fe^{2+}	12.722	62.130	109(1)	Hugh-Jones et al. (1997)

Notes: $K'_0 \equiv 4.0$. n/r: values not reported in reference.

APPENDIX C

$NaGaSi_2O_6$ CLINOPYROXENE AT HIGH-PRESSURE: A RAMAN AND X-RAY SINGLE-CRYSTAL INVESTIGATION

$NaGaSi_2O_6$ clinopyroxene at high-pressure: a Raman and X-ray single-crystal investigation

Andrew C. McCarthy[1]*, Robert T. Downs[1], Richard M. Thompson[1],

Ren Lu[1], Hexiong Yang[1] and Haruo Ohashi[2]

[1]*Department of Geosciences, University of Arizona, Tucson, Arizona 85721-0077, U.S.A.*

[2]*HASHI Institute for Silicate Science, Nishinakanobu, 1-9-25, Shinagawa, Tokyo 142-0054, Japan*

* E-mail: mccarthy@geo.arizona.edu

Abstract

The crystal structure of synthetic *C*2/*c* pyroxene $NaGaSi_2O_6$ was studied at room temperature and high-pressures using Raman spectroscopy and single-crystal X-ray diffraction. Raman spectra were collected at twenty-four pressures over the range 0-16.5 GPa, with nine collections during compression and fourteen during decompression. Two Raman peaks, initially at 510 cm^{-1} and 969 cm^{-1}, disappear with increasing pressure. X-ray diffraction was used to collect unit cell data at 20 pressures over the range 0-11.1 GPa and intensity data at 8 of these pressures. A third-order Birch-Murnaghan equation of state fit to the *P*-*V* data yields V_0 = 416.9(2) $Å^3$, K_0 = 134(4) GPa, and $K_0^{'}$ = 2.5(7). With $K_0^{'}$ constrained to 4.0, the bulk modulus of 125(1) is close to the value of 128 GPa (with $K_0^{'} \equiv 4.0$) predicted by the empirical model of McCarthy et al. (accepted).

$NaGaSi_2O_6$ exhibits strongly anisotropic compression with unit strain axial ratios $\varepsilon_1:\varepsilon_2:\varepsilon_3$ of 1.00:2.12:2.46. Silicate chains undergo an O-type rotation with pressure, reducing ∠O3-O3-O3 from 172.8(2)º at ambient conditions to 167.5(7)º at 9.69 GPa. Four isostructural Na-clinopyroxenes have recently been subjected to high-pressure *in-situ* structural X-ray diffraction studies: jadeite, $NaAlSi_2O_6$ (McCarthy et al. in press); aegirine, $NaFeSi_2O_6$ (McCarthy et al. submitted); kosmochlor, $NaCrSi_2O_6$ (Origlieri et al. 2003); and $NaGaSi_2O_6$ (this study). We compare the compression behavior of $NaGaSi_2O_6$ to the behavior of other *C*2/*c* Na-pyroxene structures.

Introduction

$NaGaSi_2O_6$ is a monoclinic pyroxene (space group *C*2/*c*) first synthesized and identified by Ohashi et al. (1983). It is part of the clinopyroxene series $NaM^{3+}Si_2O_6$ where M^{3+} = Al, Mn, Fe, Ti, Sc, V, Cr, Ga or In, herein called the jadeite series. This series has a general formula $M2M1Si_2O_6$, with trivalent cations occupying M1 and Na at M2. Cations larger than In^{3+} (e.g., Y^{3+}) are unable to fit in the structure at the octahedrally coordinated M1 due to size constraints imposed by the silicate chain (Redhammer and Roth 2004). Most members of the series are known to occur as minerals, including: jadeite (Al), namansilite (Mn), aegirine (Fe), jervisite (Sc), natalyite (V) and kosmochlor (Cr). However, only jadeite and aegirine can be considered common minerals on Earth. Three jadeite-series minerals have previously been subjected to high-pressure single-crystal X-ray diffraction structural studies: jadeite to 9.2 GPa (McCarthy

et al. 2007), aegirine to 10.8 GPa (McCarthy et al. submitted) and kosmochlor to 9.3 GPa (Origlieri et al. 2003). The structure of $NaGaSi_2O_6$ at pressure is examined in the current study.

$NaGaSi_2O_6$ is isostructural with the other members of the jadeite series. Each of these structures exhibits several identical and characteristic topological elements: 1) an M1 cation in nearly regular octahedral coordination with oxygen; 2) chains of edge-sharing $M1O_6$ octahedra parallel to **c**; 3) Na at M2 coordinated with six oxygen atoms in an irregular polyhedron; 4) chains of corner-linked SiO_4 tetrahedra parallel to **c**. The structure of $NaGaSi_2O_6$ is illustrated in Figure 1. Oxygen atom positions are labeled according to the nomenclature suggested by Downs (2003).

Although topologically identical, the various $NaM1^{3+}Si_2O_6$ structures do exhibit geometric differences, which should be entirely related to variations in M1 cations. The radii of the M1 cations in the series vary widely: 0.535 Å (Al), 0.645 Å (Mn), 0.645 Å (Fe), 0.615 Å (Cr), 0.620 Å (Ga), and 0.800 Å (In) (Shannon 1976), as do their electronic configurations. Redhammer et al. (2003) review structural data from the jadeite series and show many interatomic distances to be correlated with the size of the M1 cation. The size of the M1 cation has also been shown to control clinopyroxene unit cell volumes. Thompson et al. (2005) showed an even stronger correlation between M1 size and unit cell volume among populations of pyroxenes with constant M2 cation (e.g., the jadeite series).

Several studies have suggested the possibility of a pressure-induced $C2/c \rightarrow C2/c$ transition in jadeite series minerals. Downs (2003) reported procrystal electron density

analysis of Na-clinopyroxenes indicating that Na at M2 in these minerals is bonded to six coordinating oxygen atoms. He also suggested that a change from 6- to 8-coordinated Na could occur with pressure. In jadeite-series structures, two non-bonded oxygen atoms ($O3_{1,4}$) reside slightly outside of the Na coordination sphere but are observed to move closer to the M2 site with pressure (Origlieri et al. 2003; McCarthy et al. 2007). Linear extrapolation of decreasing Na-$O3_{1,4}$ bond lengths suggests that two additional Na-O bonds could form in jadeite series minerals, including $NaGaSi_2O_6$, at pressures near 20 GPa (McCarthy et al. 2007). This transition has yet to be observed, and only awaits a high-pressure Raman spectroscopy or X-ray diffraction experiment on a mineral of the jadeite series utilizing a hydrostatic pressure medium such as a gas-loaded diamond anvil cell. The transition should occur in the mantle where jadeite series minerals are able to reach the pressure-equivalent depth. However, at the low concentrations (< 5%) expected in the upper mantle, jadeite-series minerals are soluble components in other pyroxenes. In such non-end-member structures, the postulated Na-O bonding transition might not occur.

Chopelas and Serghiou (2002) presented spectroscopic evidence suggesting that diopside may undergo a $C2/c \rightarrow C2/c$ bonding transition at high pressure. They suggested that changes observed in the Raman spectrum of diopside at 10 GPa may be due to a change from an 8- to a 6-coordinated M2 cation (Ca), which in some sense is opposite of the expected transition in jadeite series clinopyroxenes. The transition in diopside went unconfirmed by a recent high pressure X-ray diffraction study on diopside to 10.2 GPa by Thompson and Downs (accepted).

Previous work

The structure of $NaGaSi_2O_6$ was first reported by Ohashi et al. (1983), who found the material to be isostructural with jadeite. Further studies of $NaGaSi_2O_6$ by Ohashi et al. (1995) found that Ga^{3+} may be present in two different electronic states, creating two slightly different structures with different unit cell parameters. A subsequent study on $NaGaSi_2O_6$ has been unable to confirm the existence of the two different structures (Nestola et al. 2007).

Nestola et al. (2007) examined a $NaGaSi_2O_6$ crystal with X-ray diffraction at temperatures from 295 to 110 K. One aim of their study was to attempt to identify the *C*2/*c*→*P*bar1 phase transition observed in $NaTiSi_2O_6$ by Redhammer et al. (2003). A similar transition was not observed in $NaGaSi_2O_6$. Nestola et al. (2007) did observe, however, a steady decrease in *a*, *b*, *c*, and *V* with decreasing temperature, while *β* was found to remain constant within error. Some anomalies in <*R*(Ga-O)> and, thus, the volume of the M1 polyhedron were noted at ~180 K.

Redhammer et al. (2003) examined a $NaTiSi_2O_6$ crystal with X-ray diffraction at temperatures from 298 to 100 K and identified a *C*2/*c* to *P*bar1 phase transition near 197 K. These authors also briefly review structural parameters for the jadeite series $NaM^{3+}Si_2O_6$ structures and point out that the size of the M1 cations controls many of the variations in structure across the series.

X-ray diffraction data from $NaGaSi_2O_6$ at high pressure has not been previously reported. However, many other $NaM^{3+}Si_2O_6$ materials have been examined at pressure with X-ray diffraction. Those studies which reported atomic positions were mentioned previously. Other high-*P* work on members of this series includes Nestola et al. (2006) and Downs and Singh (2006). Nestola et al. (2006) examined four crystals from the jadeite-aegirine solid solution at pressures up to 9.74 GPa and reported unit cell parameters. Their study included end-member jadeite and aegirine crystals. Downs and Singh (2006) examined aegirine under non-hydrostatic conditions above 11.1 GPa, and reported unit cell parameters from ambient pressure to 13.52 GPa.

Several clinopyroxenes have been subjected to high-pressure Raman spectroscopic studies, but no such studies are known to have been reported on jadeite-series minerals.

Experimental Methods

All experiments used $NaGaSi_2O_6$ single crystals synthesized by Ohashi et al. (1983). Crystals were produced from the starting materials $Na_2Si_2O_5$, Ga_2O_3 and SiO_2 in a solid state reaction. Synthesis was carried out using a belt-type high-pressure oven described by Fukunaga et al. (1979), with conditions of 1500ºC and 60kb applied for five hours. Two separate crystals from the same synthesis batch were used: one for Raman and one for X-ray diffraction high pressure experiments.

High-pressure Raman spectroscopy

A $NaGaSi_2O_6$ crystal with dimensions of 40 × 60 × 120 μm was selected from a batch of a few dozen based on the quality of its Raman spectrum in air at room conditions. The crystal was loaded into a four-pin Merrill-Bassett type diamond anvil cell (DAC) along with several small (< 5 μm) ruby chips and a mix of 4:1 methanol-ethanol as a pressure-transmitting medium. The DAC used steel seats and wide apertures to maximize the signal collected from the cell. The diamond culets were ~600 μm in diameter. The (110) direction of the crystal was parallel to the diamond cell axis, while the (001) direction was roughly parallel to the polarization direction of the excitation laser. Steel gaskets with a thickness of 250 μm were used, pre-indented to 70-90 μm, with a 250 μm diameter sample chamber. Sample chamber pressures were determined from the fitted positions of the R_1 and R_2 ruby fluorescence lines using the calibration of Mao et al. (1978). Estimated error in pressure measurements is ±0.05 GPa. Pressure measurements were taken before and after each spectrum acquisition and the reported value is the mean of these two. Raman spectra were collected in the region between ~85 and 1300 cm^{-1}, with a resolution of ~4 cm^{-1}, while ruby fluorescence was collected in the ~694 nm region, both with a 532 nm solid state laser. All acquisitions were made using a Thermo Almega XR Raman system equipped with both 532 and 785 nm lasers, a thermoelectric cooled CCD detector, and a 20x Mitutoyo M Plan Apo long working distance objective interfacing with the DAC. Pressure was increased to 16.5 GPa, at which the ruby doublet peaks displayed significant increases in peak widths and poorly resolved separation, indicating severe non-hydrostatic conditions. The pressure was then

decreased back down to 0.7 GPa, with Raman spectra collected during both compression and decompression.

At ~15 GPa, an additional test was carried out to determine the extent to which conditions in the DAC were non-hydrostatic. Fluorescence spectra were collected from five different ruby crystals scattered throughout the cell. Pressure in the central part of the DAC sample chamber was found to deviate from 15 GPa by up to 1 GPa, well outside the expected measurement error of ±0.05 GPa. Also, a single ruby crystal adjacent to the sample chamber wall yielded a fluorescence spectrum indicating a pressure of 13.6 GPa. Therefore, at this pressure (~15 GPa), the various rubies gave inconsistent fluorescence peak positions, resulting in a pressure variation of about 1 GPa.

High-pressure X-ray diffraction

Several $NaGaSi_2O_6$ crystals were examined using a Bruker X8 to find a high-quality crystal exhibiting sharp, isolated diffraction spots. The size of the selected crystal was 80 × 70 × 40 μm. A full data collection was performed and refined, which confirmed the structure determined by Ohashi et al. (1983) within error.

Next, diffraction data were collected with an automated Picker four-circle diffractometer using unfiltered MoKα radiation and operating at 45 kV and 40 mA. Before loading in the DAC, the crystal was examined in air. The positions of 28 high-intensity peaks ($9^\circ < 2\theta < 33^\circ$) were determined using a modification of the eight-peak centering technique of King and Finger (1979). Specifically, the positions were determined by fitting both $K\alpha_1$ and $K\alpha_2$ profiles with Gaussian functions. Typical peak

widths were 0.10º in ω. Refined cell parameters constrained to monoclinic symmetry are given in Table 1. A half-sphere of intensity data was collected to $2\theta \leq 60º$, using ω scans of 1º width, step size 0.025º, and 3 s per step counting times. The structure was refined on *F* with anisotropic displacement parameters using a modification of RFINE (Finger and Prince, 1975) to $R_w = 0.025$. Structural data at room conditions are summarized in Table 2. These data have smaller errors than Ohashi et al. (1995) ($R_w = 0.029$) but otherwise are similar within error.

The $NaGaSi_2O_6$ crystal was loaded into a four-pin Merrill-Bassett type DAC with beryllium seats. The vector perpendicular to the (110) plane was oriented parallel to the DAC axis. The diamond anvil culet size was 600 μm. A 250 μm thick stainless steel gasket pre-indented to 120 μm, with a 350 μm diameter hole, was used. Along with the $NaGaSi_2O_6$ crystal, the sample chamber was loaded with a small ruby fragment and a 4:1 mixture of methanol:ethanol as pressure medium. Ruby fluorescence spectra were collected before and after each collection of intensity data, and the positions of the R_1 and R_2 peaks were determined by fitting with Lorentzian functions. Using the method of Mao et al. (1978), pressure was calculated from the fitted R_1 and R_2 peak positions with an estimated error of ±0.05 GPa.

The experiment was carried out to a pressure of 11.1 GPa. Upon further increasing the pressure in the DAC, the gasket failed. Unit-cell data were collected at 20 pressures, and intensity data were collected at 8 of these pressures.

Every accessible reflection allowed by *C*2/*c* symmetry, up to 672 intensity data ($2\theta \leq 60º$), were collected at pressure, with ω scans of 1º width, in steps of 0.025º and

counting times of 10 s per step. These data reduced to 222 symmetry-equivalent reflections. Reflections violating *C*2/*c* were examined, but none with significant intensities was found throughout the experiment. Absorption corrections for the beryllium seats and diamond anvils were made from an absorption correction profile of the DAC before loading. Structure factors were weighted by $\omega = [\sigma_F^2 + (pF)^2]^{-1}$, where σ_F was obtained from counting statistics and *p* chosen to insure normally distributed errors (Ibers and Hamilton, 1974). Structural data were refined with isotropic displacement factors using a modified version of RFINE (Finger and Prince, 1975) and are summarized in Table 3. R_w ranged from 0.025 to 0.095.

Bond lengths and angles were calculated using BOND91 software, modified after Finger and Prince (1975). Polyhedral volumes and quadratic elongations were obtained with XTALDRAW (Downs and Hall-Wallace, 2003). Selected bond lengths, angles, and polyhedral volumes are presented in Table 4.

Results and Discussion

Raman spectroscopy

High-pressure Raman spectroscopy to 16.5 GPa was undertaken in an attempt to identify the *C*2/*c*→*C*2/*c* phase transition expected in $NaGaSi_2O_6$. For comparison with spectra collected at high pressures in the DAC, a Raman spectrum was collected from a $NaGaSi_2O_6$ crystal in air at ambient pressure. Figure 2 illustrates this spectrum, which reveals 18 identifiable Raman peaks, labeled v_1-v_{18}, in the range 100-1300 cm^{-1}. This spectrum was collected on the same instrument used to collect spectra at high pressures,

and the crystal was oriented the same within ~5º. Factor group analysis indicates that materials with in *C*2/*c* space group should exhibit 14 A_g and 16 B_g Raman-active modes (Pommier et al. 2003). This number of modes is rarely observed in experimental studies of *C*2/*c* materials for reasons such as degeneracy, lack of resolution, and low signal-to-noise ratios (Pommier et al. 2003). Chopelas and Serghiou (2002) also calculated the expected Raman modes for *C*2/*c* diopside and found 20 related to internal motions of the SiO_4 chain, four related to external chain motions, and six due to cation translations.

Figure 3 illustrates the 24 Raman spectra (100-1300 cm^{-1}) collected at all pressures in this experiment, from ambient to 16.45(5) GPa. No clear evidence of a phase transition was observed in the Raman spectra, although significant changes in the spectra did occur with increasing pressure. Peak positions for v_1-v_{18} are listed in Table 5. All peaks displayed a gradual, approximately linear increase in wavenumber with pressure (Fig. 4). Such behavior is characteristic of Raman peaks as interatomic distances decrease (Huang et al. 2000). Additionally, two peaks disappeared with increasing pressure, indicating some possible structural changes. These are discussed in more detail below.

The Raman peaks in pyroxenes generally have not been rigorously assigned to specific atomic interactions. However, some peaks and wavenumber ranges have been associated with specific parts of the pyroxene structure. Zhang et al. (2002) assigned the following ranges to particular atomic interactions in pyroxenes: 50-425 cm^{-1}, complex lattice vibrations; 425-650 cm^{-1}, O-Si-O bending; 650-800 cm^{-1}, Si-O_b stretch; and 800-1200 cm^{-1}, Si-O_{nb} stretch. Huang et al. (2000) examined a series of ortho- and

clinopyroxenes at room conditions and assigned more specific wavenumber ranges to particular atomic interactions. Non-bridging and bridging Si-O modes were assigned to 1020 ± 50 cm^{-1} and 900 ± 50 cm^{-1}, respectively. The corresponding peaks in the $NaGaSi_2O_6$ spectrum are v_{17} (1034 cm^{-1}) and v_{15} (874 cm^{-1}).

The prominent peak or peaks in the 600-800 cm^{-1} range have been attributed to interactions involving the SiO_4 chain in pyroxenes (Huang et al. 2000). The *C*2/*c* pyroxenes, with one unique chain, exhibit a singlet in this region, whereas $P2_1/c$ pyroxene structures, which have two unique SiO_4 chains, typically show a distinct doublet. In a high-pressure Raman study of $LiFeSi_2O_6$, Pommier et al. (2005) observed a doublet in the 600-800 cm^{-1} range while the material was still in *C*2/*c*, below the transition pressure to $P2_1/c$. Raman spectra of $NaGaSi_2O_6$ show a strong singlet (v_{13}) in the Si-O_b stretching range, thought to be indicative of a single T-chain geometry and *C*2/*c* symmetry. This peak is not observed to split with pressure.

All 18 peaks identified in the $NaGaSi_2O_6$ Raman spectrum at ambient conditions can be identified in the spectra collected at the lowest pressures, although additional features and increased background noise are also present (Fig. 3). Comparison with the spectrum collected outside the DAC shows that several peaks are related to either the diamonds or the pressure medium. Specifically, features seen in the Raman spectra below 150 cm^{-1} and above 1075 cm^{-1} appear to be related to Raman excitation of materials other than $NaGaSi_2O_6$. The high-*P* spectra display many features in these ranges. Within the range 150-1075 cm^{-1}, all of the major features present in the high-*P* Raman spectra appear to be related to the $NaGaSi_2O_6$ structure, possibly with the

exception of the major peak at ~880 cm^{-1} (v_{15}), which displays a very low intensity at ambient *P* outside the DAC. Both this peak and the peak near 1020 cm^{-1} have been observed in methanol:ethanol pressure medium by previous workers (cf. Pommier et al. 2005). The major peak at ~1020 cm^{-1} (v_{17}) shows significant broadening and a much higher intensity in the high-pressure spectra, because of interference from the pressure medium peak at approximately the same wavenumber. This makes it impossible to examine the true pressure-induced behavior of the Raman peak in $NaGaSi_2O_6$ near the same wavenumber.

Two significant changes in the spectra are observed with increasing pressure. First, the doublet at 500-550 cm^{-1} (assigned v_{11} and v_{12}) becomes a singlet centered at 550 cm^{-1} as v_{11} decreases in intensity and disappears above 12.5 GPa (Fig. 5). Second, the peak near 970 cm^{-1}, v_{16}, decreases in intensity with pressure then suddenly disappears above 7.5 GPa (Fig. 3).

The behavior of the apparent doublet (v_{11} and v_{12}) at 500-550 cm^{-1} with increasing pressure is unusual. The intensity of the v_{11} portion of the doublet gradually reduces between 7.5 and 10.2 GPa, but a slight shoulder is still visible on the singlet (v_{12}) above 10.2 GPa, which is only gone above 12.5 GPa. The wavenumbers of these peaks indicate that they are related either to M-O interactions (Pommier et al. 2003) or Si-O bending (Zhang et al. 2002; Huang et al. 2000). However, no changes in M1-O or M2-O bond topology are expected through 13 GPa in $NaGaSi_2O_6$, and none is observed up to 9.69 GPa in our X-ray diffraction experiment on this material. The expected bonding change with M2, at ≥19 GPa, involves the formation of M2-$O3_{1,4}$ bonds during a postulated *C*2/*c*

→ *C*2/*c* transition, which should occur over a very small *P* interval. Instead, we observe a gradual diminishing of the intensity of the v_{11} peak over a ~13 GPa pressure interval. If v_{11} and v_{12} are related to M-O bonding, one possible explanation for the observed behavior is a M-O bond length crossover. Linear extrapolation of Ga-O bond lengths (Fig. 6) indicates a potential bond length crossover at ~17 GPa, at which point the Ga-O1a separation would equal the Ga-O1b separation. If the changes in v_{11} and v_{12} are caused by the converging Ga-O separations, however, the v_{11} peak would be expected to merge with the v_{12} peak rather than remaining separated while diminishing in intensity. Na-O separation trends with pressure (Fig. 7) show no indications of separation distance crossovers unless extrapolated to >20 GPa. Zhang et al. (2002) indicate that Raman peaks in pyroxenes in the range 425-650 cm^{-1} may be related to O-Si-O bending. No significant changes in Si-O bonding were observed in the structures determined with X-ray diffraction, and no M-O bonds to Si-bonded oxygens were observed to form or break. However, the highest-pressure structure determination was at 9.69 GPa, and the v_{11} Raman peak does not fully disappear until >12.5 GPa. Therefore, a high-pressure X-ray diffraction study to ~20 GPa on $NaGaSi_2O_6$ is warranted, not only in an attempt to observe the postulated *C*2/*c* → *C*2/*c* phase transition but also to determine the structural causes of the changes observed in the high-pressure Raman spectra.

The second significant change in the Raman spectra of $NaGaSi_2O_6$ with pressure is the disappearance of v_{16} above 7.5 GPa (Fig. 3). This peak, centered at 969 cm^{-1} at ambient conditions, is broad but well defined at ambient conditions outside the cell (Fig. 2). In the DAC, the intensity of the peak diminishes with increasing pressure, but the

peak is still well defined (i.e., with an intensity several times the magnitude of noise) in the spectrum collected at 7.5 GPa. Raman peaks in pyroxenes in this range are thought to be related to Si-O_{nb} stretch (Zhang et al. 2002). However, as stated previously, no significant changes were observed in Si-O bonding in the X-ray diffraction experiment on $NaGaSi_2O_6$ to 9.69 GPa.

X-ray diffraction

A third-order Birch-Murnaghan equation was fit to the data in Table 1 to determine a *P*-*V* equation of state for $NaGaSi_2O_6$, resulting in $V_0 = 416.9(2)$ Å^3, $K_0 =$ 134(4) GPa, and $K_0^{'} = 2.5(7)$. The data and fitted curve from our diffraction experiment are plotted in Figure 8. Setting $K_0^{'} \equiv 4.0$ results in values of: $V_0 = 417.2(1)$ Å^3 and $K_0 =$ 125(1) GPa. The constrained bulk modulus for $NaGaSi_2O_6$ compares with the constrained ($K_0^{'} \equiv 4.0$) bulk moduli of jadeite (134(1) GPa), aegirine (117(1) GPa), and kosmochlor (128(1) GPa) as reported in McCarthy et al. (2007). The hierarchy of stiffness, jadeite > kosmochlor > $NaGaSi_2O_6$ > aegirine, does not follow the ambient unit cell volumes of the materials from smallest to largest: kosmochlor is anomalously stiff based on its ambient unit cell volume. McCarthy et al. (2007) examined compressibility trends of *C*2/*c* and *P*2_1/*c* silicate clinopyroxenes. Based on an empirical model which related bulk modulus to 1) ambient unit cell volume, and 2) M2-O3 bond topology relative to bending of the O3-O3-O3 angle in the tetrahedra chains, they predicted a bulk

modulus for $NaGaSi_2O_6$ of 128.4 GPa, with $K_0^{'}$ fixed to 4.0. Our fitted bulk modulus for $NaGaSi_2O_6$ with $K_0^{'} \equiv 4.0$ was calculated to be 125(1) GPa.

Figure 9 shows the normalized unit cell volumes of the four jadeite-series structures examined at high pressures. A divergence of the trend with pressure is noted, with aegirine compressing the most with *P*, and jadeite the least. This behavior is expected considering the ambient-pressure unit cell volumes for the four structures. Aegirine exhibits the largest ambient unit cell volume, 429.40(9) $Å^3$ (McCarthy et al. submitted), whereas jadeite exhibits the smallest ambient unit cell volume, 402.03(2) $Å^3$ (McCarthy et al. 2007). The variation in ambient unit cell volumes is also reflected in the calculated bulk moduli for these materials.

Average M1-O bond lengths (Fig. 10) reflect the changing size of the M1 cations and/or oxygen atoms with pressure. The <*R*(M1-O)> in all four structures decreases with pressure as the $M1O_6$ octahedra compress. The Ga-O bond length changes with *P* in $NaGaSi_2O_6$ are illustrated in Figure 6. Of all Ga-O bond pairs, the Ga-O2 bond distances decrease the most with pressure. Linear extrapolation of the bond lengths shown in Figure 6 suggests that a GaO2 bond length crossover with GaO1b bonds may occur near 17 GPa.

The composition of M2 (Na) is constant for all structures in the jadeite series. Also, M2-O bond topology is the same in each structure: Na is bonded to six nearest-neighbor oxygens (two O1, two O2, $O3_2$ and $O3_3$) (Fig. 1) (Downs 2003). Despite these similarities, average Na-O separations are observed to vary among structures in the series. Figure 11 shows the average Na-O separations (including the unbonded pair Na-

$O3_{1,4}$) versus pressure for the jadeite, aegirine, kosmochlor, and $NaGaSi_2O_6$ structures. Average Na-O separations are correlated with M1 size and thus with unit cell volume, which is controlled by M1 size. Redhammer et al. (2003) observed a similar phenomenon for Na-O bond lengths in ambient-condition jadeite-series structures. The Na-O bond lengths in $NaGaSi_2O_6$ as a function of pressure are shown in Figure 7. As in other studied jadeite-series structures, the non-bonded Na-$O3_{1,4}$ distances decrease much more as a function of pressure than the bonded Na-O distances. This behavior should lead to a Na-O separation distance "crossover" which likely marks the $C2/c \rightarrow C2/c$ transition in $NaGaSi_2O_6$.

No evidence of a phase transition in $NaGaSi_2O_6$ was observed over the studied pressure range in the X-ray diffraction experiment. The Na in M2 in all four clinopyroxenes considered in this study is bonded to six oxygen atoms (Downs 2003). A second pair of symmetrically equivalent oxygen atoms resides at a distance from Na between 2.741 Å (jadeite) and 2.834 Å (aegirine). With pressure, these distances decrease in all the Na-clinopyroxene structures. The rate of decrease (dR(M2-O3)/dP) of these non-bonded distances varies among the materials studied as follows: kosmochlor, 0.0082 Å/GPa; jadeite, 0.0085 Å/GPa; $NaGaSi_2O_6$, 0.0093 Å/GPa; and aegirine, 0.0096 Å/GPa. Assuming an initial Na-O bonding separation of 2.46 Å (as observed in $NaScSi_2O_6$ at ambient conditions), and an extrapolated linear decrease in this separation with pressure, Na-$O3_{1,4}$ bonds should equal ambient condition Na-$O3_{2,3}$ bond lengths first in jadeite, at ~15.6 GPa. According to this model, the other Na-clinopyroxenes would follow at 16.0 GPa (kosmochlor), 16.9 GPa (aegirine), and 17.0 GPa ($NaGaSi_2O_6$), based

on their measured decreases in M2-O3. Actual bond formation separations, however, likely vary between structures due to differences in electron density distributions. Also, Na-O bond formation in these structures may occur at distances differing from the suggested 2.46 Å. It must be stressed that the transition pressures we suggest are likely maximum pressures; the bonding transitions may occur at lower pressures. The Raman study on $NaGaSi_2O_6$ did not see any evidence of a phase transition to 16.5 GPa, just below the predicted minimum transition pressure.

All observed $NaGaSi_2O_6$ cell parameters decrease continuously with increasing pressure. Cell-parameter data were used to construct unit strain ellipsoids with STRAIN (Ohashi 1982). The unit strain ellipsoid is highly anisotropic, with axial ratios of 1.00:2.12:2.46 in the range 0-9.69 GPa, and is illustrated in Figure 12. The axial values of the unit strain ellipsoid are: ε_1, –0.001326 GPa^{-1}; ε_2, –0.002806 GPa^{-1}; and ε_3, –0.003256 GPa^{-1}. The ε_3 axis is 53.1º from **c**, and in the clinopyroxene structures, ε_2 is constrained to be parallel to **b**, with ε_1 90º from the $\varepsilon_2\varepsilon_3$ plane. Table 6 lists properties of the strain ellipsoids from $NaGaSi_2O_6$, jadeite, aegirine, kosmochlor, and a selection of other clinopyroxenes from the literature.

The magnitudes of the ellipsoid axes (ε_1,ε_2,ε_3) for the four aforementioned structures are generally similar. This is notable due to the wide variation in magnitudes observed in other pyroxene structures by Origlieri et al. (2003) and shown in Table 6. The orientations of the strain ellipsoids of the jadeite-series structures are remarkably similar, with $\varepsilon_3 \wedge \mathbf{c}$ angles in the range 32-37º. Origlieri et al. (2003) suggested a dichotomy in strain ellipsoid orientations, with the two groups exhibiting $\varepsilon_3 \wedge \mathbf{c}$ angles of

~20º and ~40º. They argued that anion packing arrangements may control strain ellipsoid orientations in the clinopyroxenes. Under their model, structures with straight T-chains (e.g. spodumene) exhibit the smaller $\varepsilon_3 \wedge \mathbf{c}$ angle due to an anion stacking direction parallel to **a***. Our more comprehensive examination of clinopyroxene structures shows no such simple dichotomy. Instead, we find $\varepsilon_3 \wedge \mathbf{c}$ angles ranging from 16.3º ($P2_1/c$ spodumene) to 49.6º ($C2/c$ spodumene) (Table 6). The $P2_1/c$ structures show the lowest $\varepsilon_3 \wedge \mathbf{c}$ angles, but $P2_1/c$ $LiScSi_2O_6$ and $P2_1/c$ $ZnSiO_3$ exhibit $\varepsilon_3 \wedge \mathbf{c}$ angles of 30.3º and 31.7º respectively, near the 32.1º angle exhibited by kosmochlor. No obvious groupings of structures can be made based on $\varepsilon_3 \wedge \mathbf{c}$ angles. The only significant outliers are the $C2/c$ and $P2_1/c$ spodumene structures at either end of the spectrum. The $\varepsilon_3 \wedge \mathbf{c}$ angle is not well-correlated with ambient unit cell volumes or calculated bulk moduli. The question remains, then, as to what controls the $\varepsilon_3 \wedge \mathbf{c}$ angle of the unit strain ellipsoids in clinopyroxene structures.

In an attempt to understand anisotropic structural control on the bulk moduli of clinopyroxenes, an examination of the magnitudes of unit strain ellipsoid axes was undertaken. The magnitudes of the short (ε_1) and intermediate (ε_2) axes of the ellipsoids do not correlate well with bulk moduli. The axis that generally is the longest (softest) axis, ε_3, was found, however, to correlate with bulk moduli with an exponential relationship (Fig. 13). The compressibility of the structures considered appears to depend strongly on the compressibility of the most compressible direction in the structure.

References

Arlt, T. and Angel, R.J. (2000) Displacive phase transitions in *C*-centred clinopyroxenes: spodumene, $LiScSi_2O_6$ and $ZnSiO_3$. Physics and Chemistry of Minerals, 27, 719–731.

Chopelas, A. and Serghiou, G. (2002) Spectroscopic evidence for pressure-induced phase transitions in diopside. Physics and Chemistry of Minerals, 29, 403–408.

Downs, R.T. (2003) Topology of the pyroxenes as a function of temperature, pressure and composition determined from the procrystal electron density. American Mineralogist, 88, 556–566.

Downs, R.T. and Hall-Wallace, M. (2003) The American Mineralogist crystal structure database. American Mineralogist, 88, 247–250.

Downs, R.T. and Singh, A.K. (2006) Analysis of deviatoric stress from nonhydrostatic pressure on a single crystal in a diamond anvil cell: The case of monoclinic aegirine, $NaFeSi_2O_6$. Journal of Physics and Chemistry of Solids, 67, 1995–2000.

Finger, L.W. and Prince, E. (1975) A system of Fortran IV computer programs for crystal structure computations. US Bureau of National Standards Technical Note 854, 128 p.

Gatta, G.D., Ballaran, T.B., and Iezzi, G. (2005) High-pressure X-ray and Raman study of a ferrian magnesian spodumene. Physics and Chemistry of Minerals, 32, 132–139.

Huang, E., Chen, C.H., Huang, T., Lin, E.H., and Xu, J.A. (2000) Raman spectroscopic characteristics of Mg-Fe-Ca pyroxenes. American Mineralogist, 85, 473-479.

Ibers, J.A. and Hamilton, W.C., Eds. (1974) International Tables for X-ray Crystallography, Volume IV, 366 p. Kynoch Press, Birmingham, U.K.

King, H.E. Jr. and Finger, L.W. (1979) Diffracted beam crystal centering and its application to high-pressure crystallography. Journal of Applied Crystallography, 12, 374–378.

Mao, H.K., Bell, P.M., Shaner, J.W., and Steinberg, D.J. (1978) Specific volume measurements of Cu, Mo, Pd, and Ag and calibration of the ruby R_1 fluorescence pressure gauge from 0.06 to 1 Mbar. Journal of Applied Physics, 49, 3276-3283.

McCarthy, A.C., Downs, R.T., and Thompson, R.M. (2007) Compressibility trends of the clinopyroxenes, and in-situ high-pressure single-crystal X-ray diffraction study of jadeite. American Mineralogist, XX, XXX-XXX.

McCarthy, A.C., Downs, R.T., and Thompson, R.M. (submitted) In-situ high-pressure single crystal X-ray study of aegirine, $NaFe^{3+}Si_2O_6$, and the role of M1 size in clinopyroxene compressibility. American Mineralogist, XX, XXX-XXX.

Nestola, F., Ballaran, T.B., Liebske, C., Bruno, M., and Tribaudino, M. (2006) High-pressure behaviour along the jadeite $NaAlSi_2O_6$-aegerine $NaFeSi_2O_6$ solid solution up to 10 GPa. Physics and Chemistry of Minerals, 33, 222–227.

Nestola, F., Rotiroti, N., Bruno, M., Tribaudino, M., Van Smaalen, S., Ohashi, H., and Redhammer, G.J. (2007) Low-temperature behavior of $NaGaSi_2O_6$. American Mineralogist, 92, 560-569.

Ohashi, Y. (1982) A program to calculate the strain tensor from two sets of unit-cell parameters. In: Hazen, R.M. and Finger, L.W. (eds) Comparative crystal chemistry. John Wiley & Sons, New York, New York, 231 pp.

Ohashi, H., Fujita, T., and Osawa, T. (1983) The crystal structure of $NaGaSi_2O_6$

pyroxene. Journal of the Japanese Association of Mineralogy, 78, 159-163.

Ohashi, H., Osawa, T., and Sato, A. (1995) Low-density form of $NaGaSi_2O_6$. Acta Crystallographica, C51, 2476–2477.

Origlieri, M.J., Downs, R.T., Thompson, R.M., Pommier, C.J.S., Denton, M.B., and Harlow, G.E. (2003) High-pressure crystal structure of kosmochlor, $NaCrSi_2O_6$, and systematics of anisotropic compression in pyroxenes. American Mineralogist, 88, 1025–1032.

Pommier, C.J.S., Denton, M.B., and Downs, R.T. (2003) Raman spectroscopic study of spodumene ($LiAlSi_2O_6$) through the pressure-induced phase change from $C2/c$ to $P2_1/c$. Journal of Raman Spectroscopy 34, 769-775.

Pommier, C.J.S., Downs, R.T., Stimpfl, M., Redhammer, G.J., and Denton, M.B. (2005) Raman and X-ray investigations of $LiFeSi_2O_6$ pyroxene under pressure. Journal of Raman Spectroscopy 36, 864–871.

Redhammer, G.J. and Roth, G. (2004) Structural variation and crystal chemistry of $LiMe^{3+}Si_2O_6$ clinopyroxenes, Me^{3+} = Al, Ga, Cr, V, Fe, Sc and In. Zeitschrift fur Kristallographie, 219, 278–294.

Redhammer, G.J., Ohashi, H., and Roth, G. (2003) Single-crystal structure refinement of $NaTiSi_2O_6$ clinopyroxene at low temperatures ($298 < T < 100$ K). Acta Crystallographica, B59, 730–746.

Shannon, R.D. (1976) Revised effective ionic-radii and systematic studies of interatomic distances in halides and chalcogenides. Acta Crystallographica, A32, 751-767.

Thompson, R.M. and Downs, R.T. (accepted) The crystal structure of diopside at

pressure to 10 GPa. American Mineralogist, XX, XXX-XXX.

Thompson, R.M., Downs, R.T., and Redhammer, G.J. (2005) Model pyroxenes III: Volume of *C*2/*c* pyroxenes at mantle *P*, *T*, and *x*. American Mineralogist, 90, 1840–1851.

Zhang, L., Ahsbahs, H., Hafner, S.S., and Kutoglu, A. (1997) Single-crystal compression and crystal structure of clinopyroxene up to 10 GPa. American Mineralogist, 82, 245–258.

Zhang, M., Redhammer, G.J., Salje, E.K.H., and Mookherjee, M. (2002) $LiFeSi_2O_6$ and $NaFeSi_2O_6$ at low temperatures: an infrared spectroscopic study. Physics and Chemistry of Minerals, 29, 609-616.

Figure 1. The structure of $NaGaSi_2O_6$ at ambient pressure and temperature. View is along a*. Na at M2 is illustrated as a sphere with six bonds to oxygens. Oxygen positions are labeled following the nomenclature of Downs (2003). Octahedra are GaO_6; tetrahedra are SiO_4.

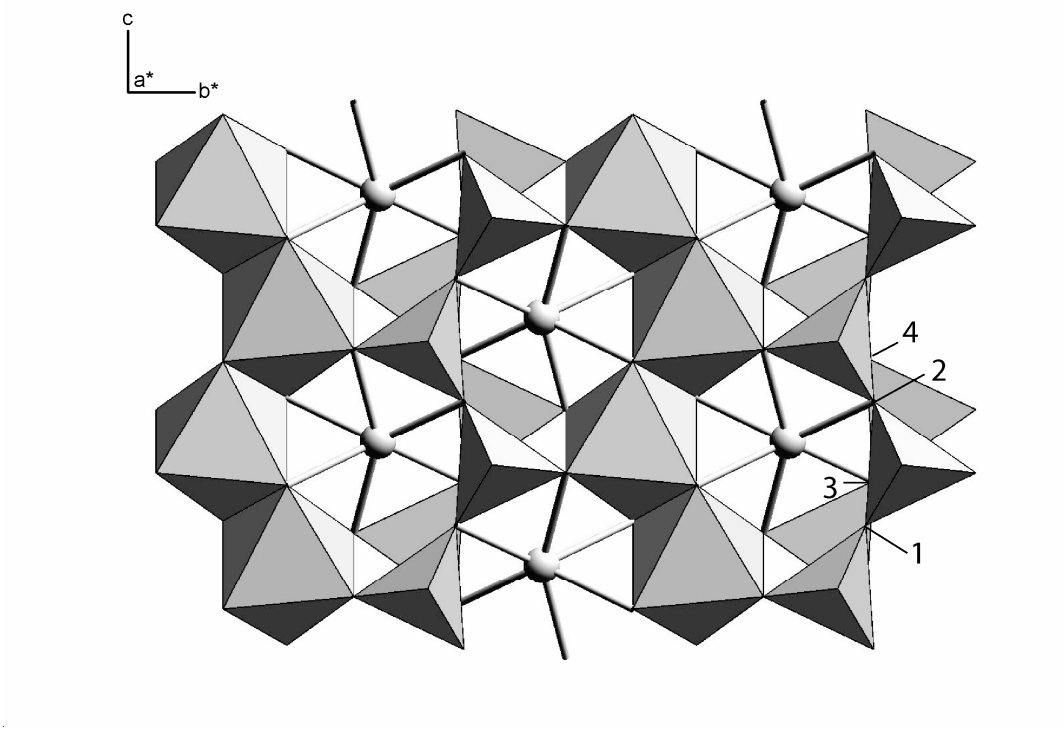

Figure 2. Raman spectra of $NaGaSi_2O_6$ in air at ambient conditions, collected from the same crystal used in the high-pressure Raman experiment. Suspected Raman peaks are labelled ν_1-ν_{18}. Crystal oriented approximately (within 5º) the same as in the high-pressure experiments.

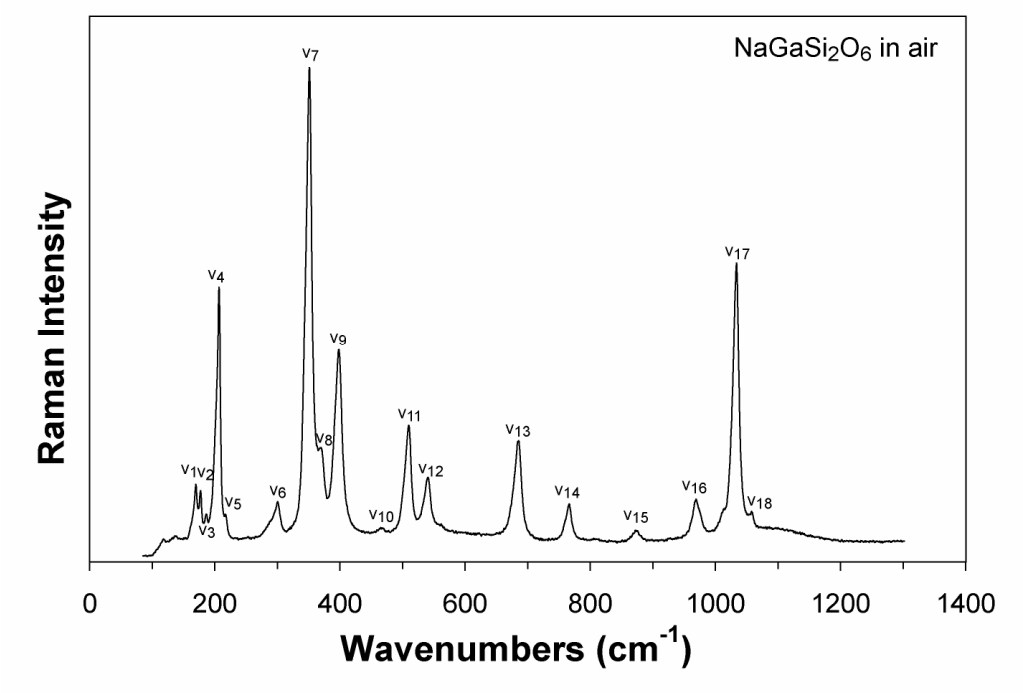

Figure 3. Raman spectra of $NaGaSi_2O_6$ collected at 24 pressures including ambient and 1.7 to 16.4 GPa. Vertical axis is arbitrary Raman intensity; spectra have been offset vertically in proportion to the pressure at which the spectrum was collected. See text for

a description of the observed changes with *P*. Errors in pressure are estimated to be ± 0.05 GPa; errors in peak positions are ± 4 cm^{-1}.

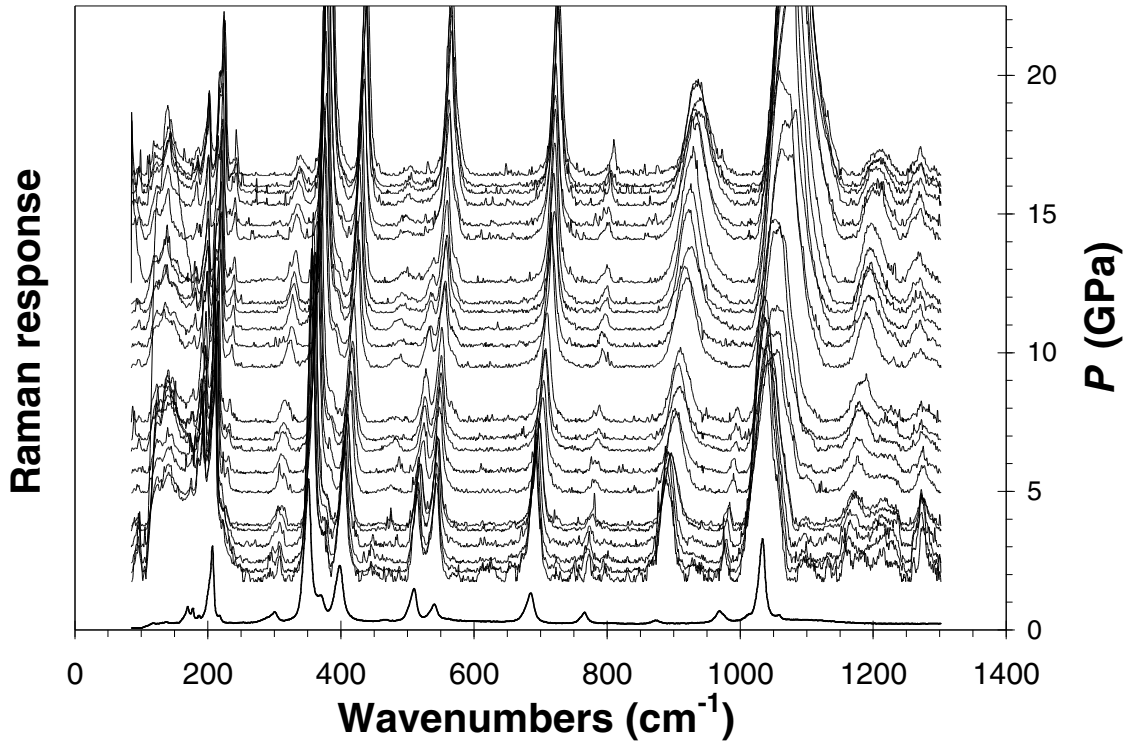

Figure 4. Variation of peak positions (ν_1-ν_{18}) with pressure in $NaGaSi_2O_6$ from amibent conditions to 16.5 GPa.

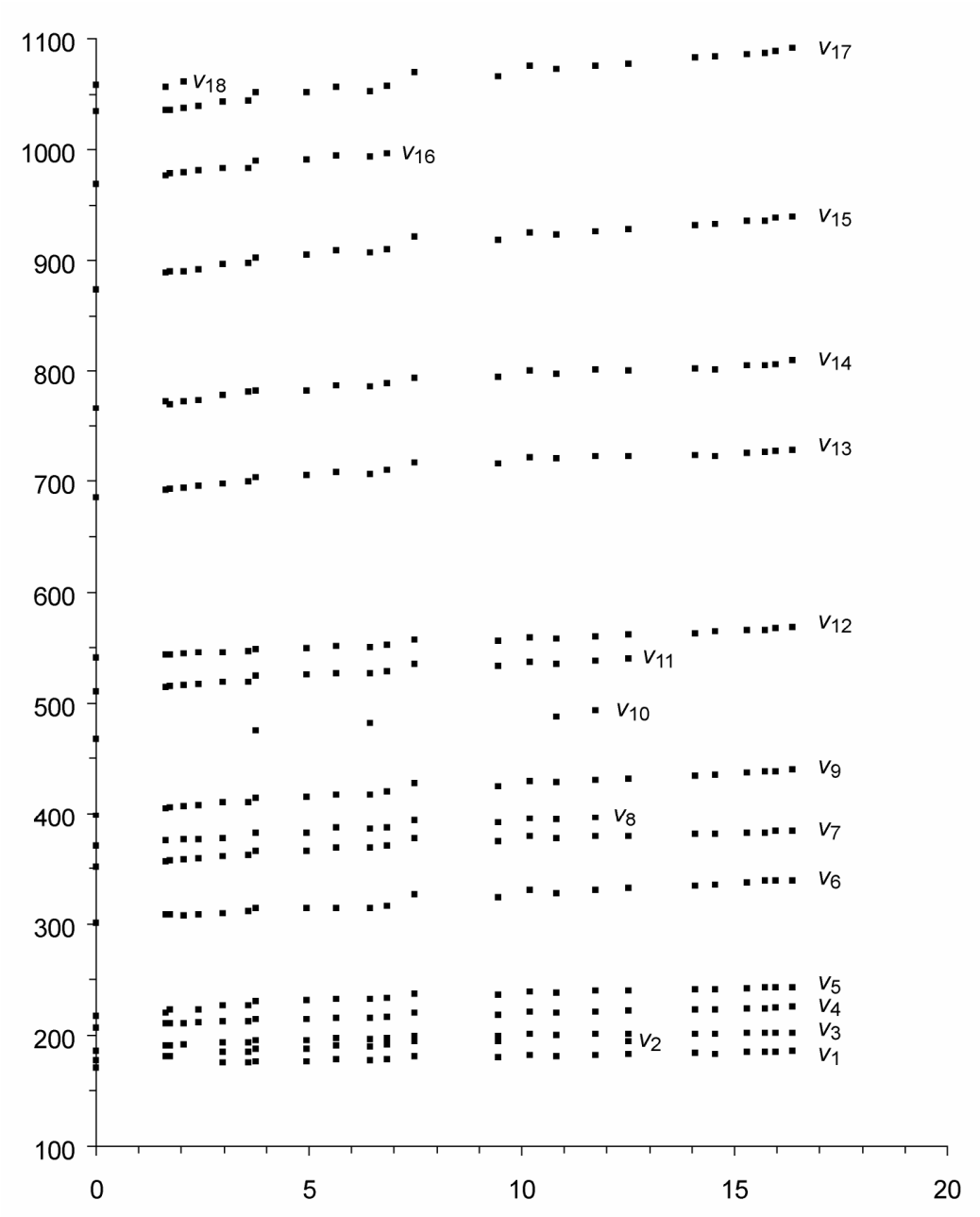

Figure 5. Peak shifts of v_{11} and v_{12} with pressure.

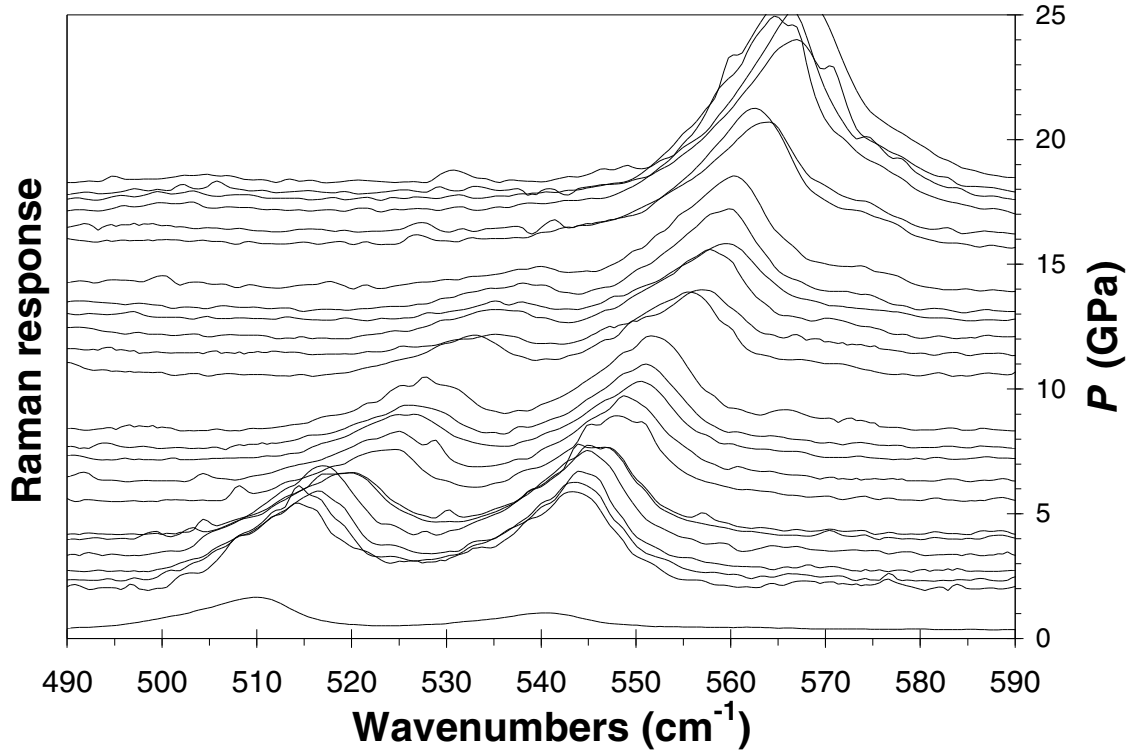

Figure 6. Variation of Ga–O distances in $NaGaSi_2O_6$ with pressure at room temperature. Solid lines are linear fits to the data.

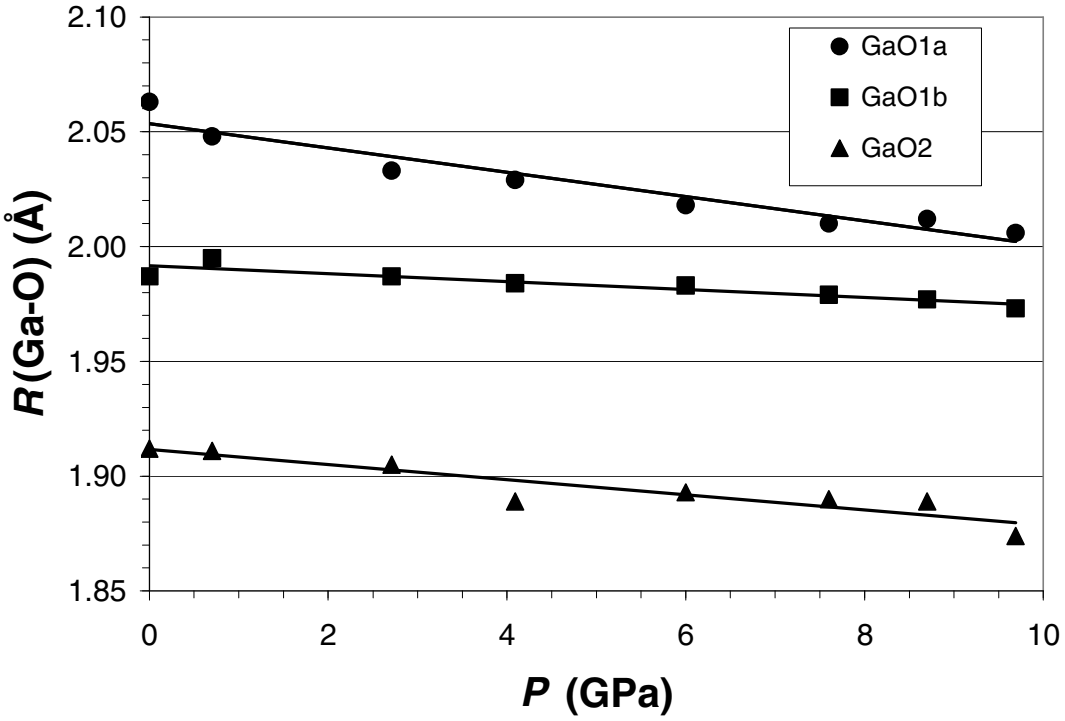

Figure 7. Variation of Na–O distances in $NaGaSi_2O_6$ with pressure at room temperature. All distances decrease approximately linearly with pressure. Solid lines are linear fits to the data. At a pressure of 19.4 GPa, the linearly extrapolated Na–$O3_{1,4}$ distance is the same as the Na–$O3_{2,3}$ distance at ambient pressure. At near this pressure, Na–$O3_{1,4}$ bonds may form, making Na 8-coordinated and constituting a *C*2/*c* → *C*2/*c* bonding transition.

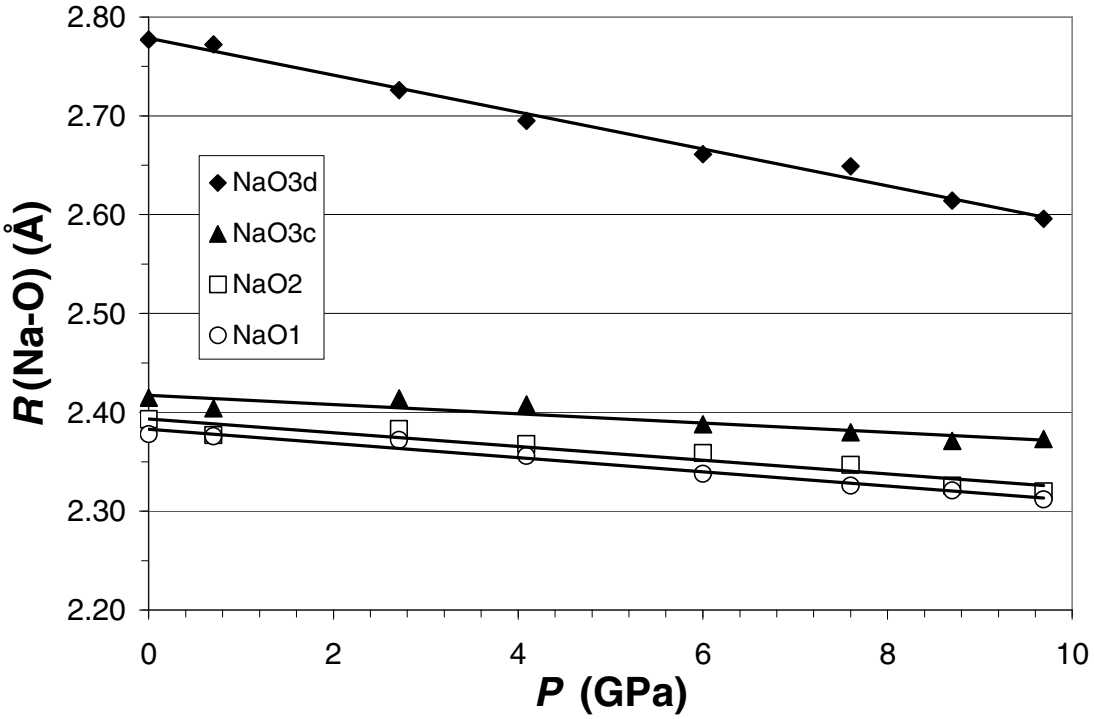

Figure 8. Unit cell volume as a function of pressure for $NaGaSi_2O_6$. Data are fit with a third-order Birch-Murnaghan equation, with V_0 = 416.9(2) Å^3, K_0 = 134(4) GPa, and $K_0^{'}$ = 2.5(7). Errors in *P* and *V* are significantly smaller than the symbols used.

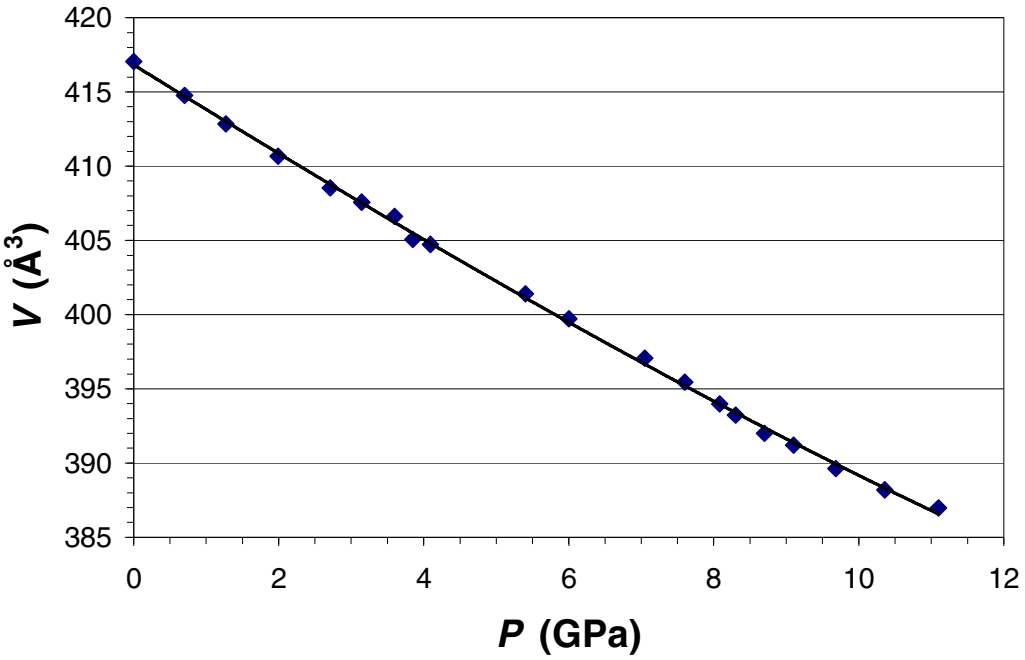

Figure 9. Normalized unit-cell volumes versus pressure for $NaGaSi_2O_6$, jadeite, aegirine and kosmochlor. Errors in *P* and *V* are significantly smaller than the symbols used.

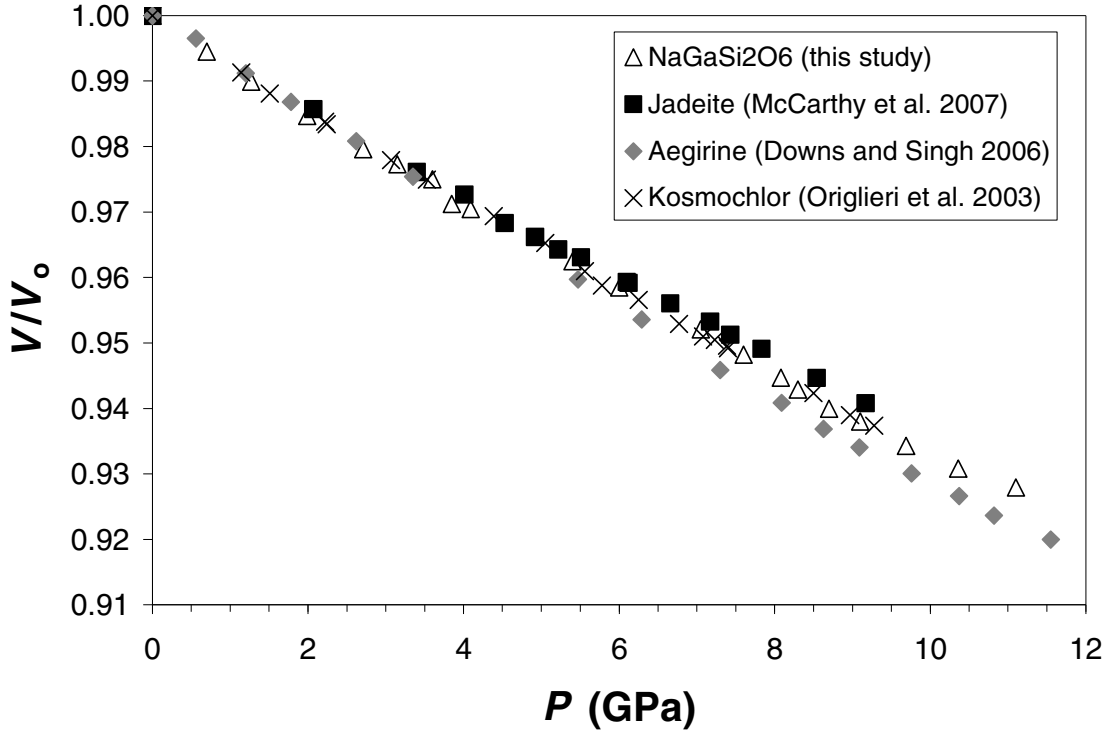

Figure 10. Variation of average M1-O bond lengths with pressure in $NaGaSi_2O_6$, jadeite, aegirine and kosmochlor.

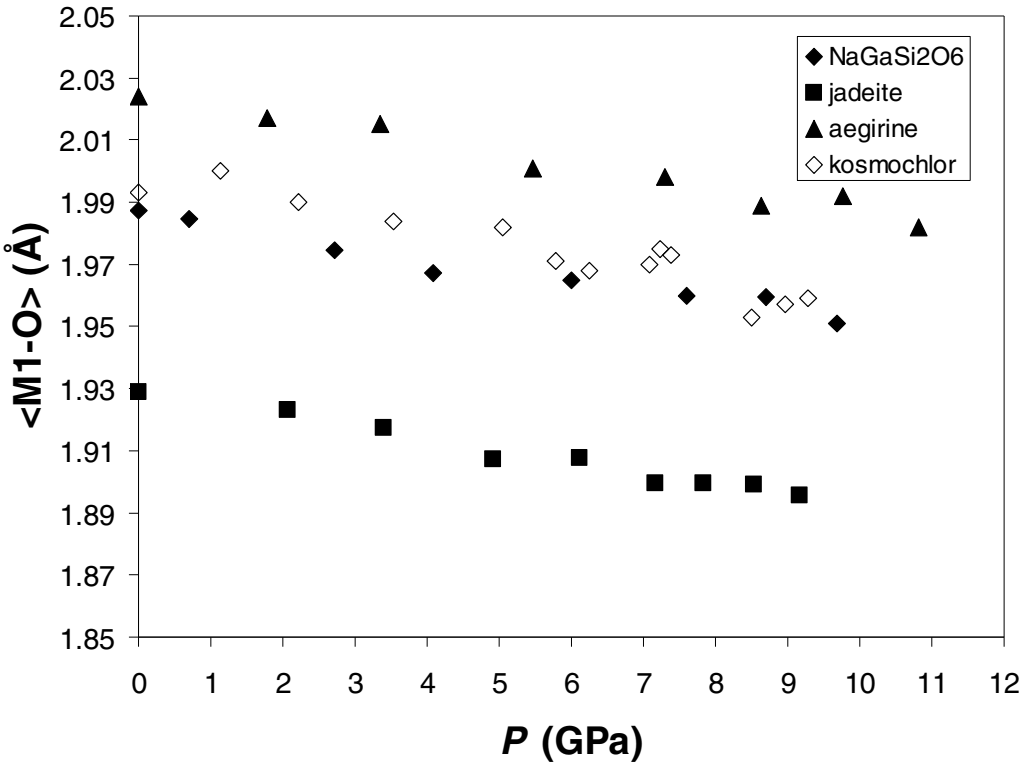

Figure 11. Average Na-O separation distances with pressure in $NaGaSi_2O_6$, jadeite, aegirine and kosmochlor. The slight convergence with pressure reflects the fact that the longer Na-O distances compress more readily with pressure.

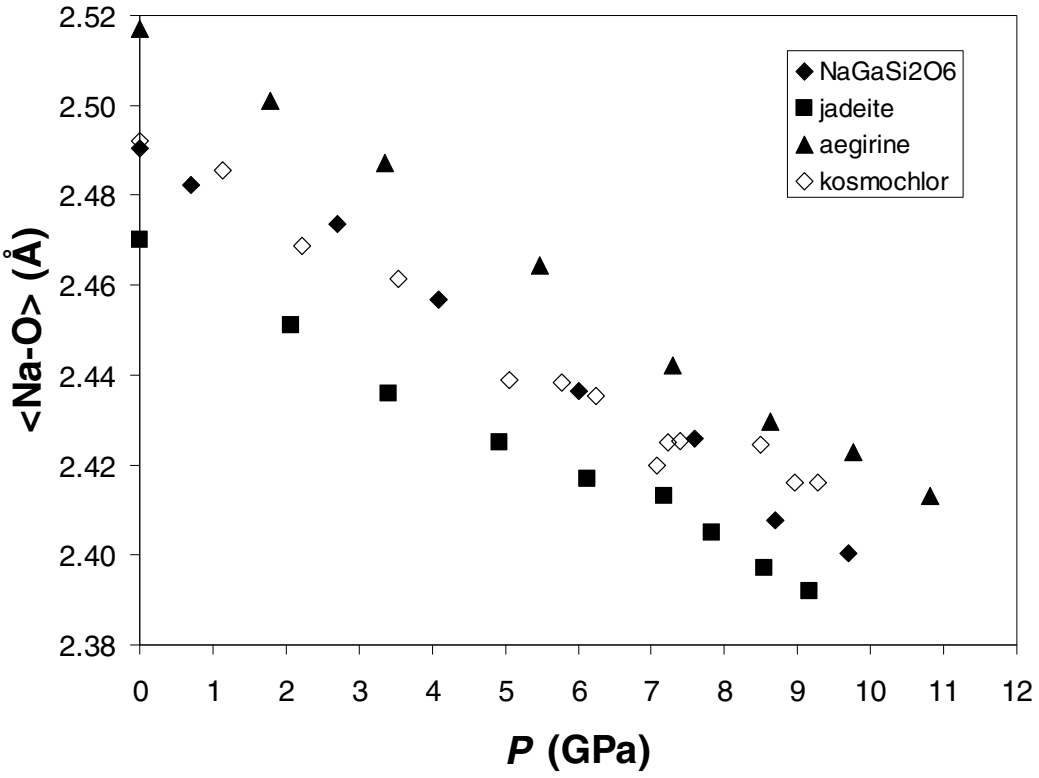

Figure 12. Oriented unit strain ellipsoid superimposed on the $NaGaSi_2O_6$ structure viewed down **b**. M2 (Na) is illustrated as a sphere. The most compressible direction in jadeite is 53º from **c**.

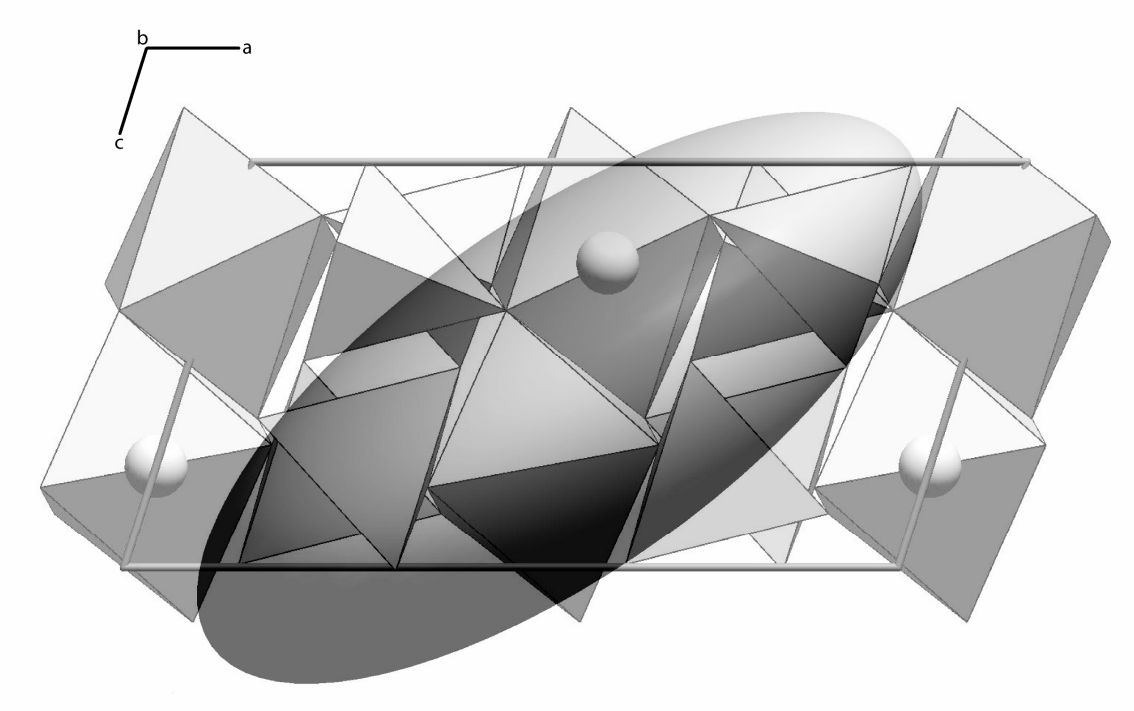

Figure 13. Bulk moduli versus magnitude of the ε_3 axis of the strain ellipse for 17 clinopyroxene structures from the literature. The overall trend suggests that clinopyroxene bulk compressibility is an exponential function of the compressibility of the most compressible direction in the structure.

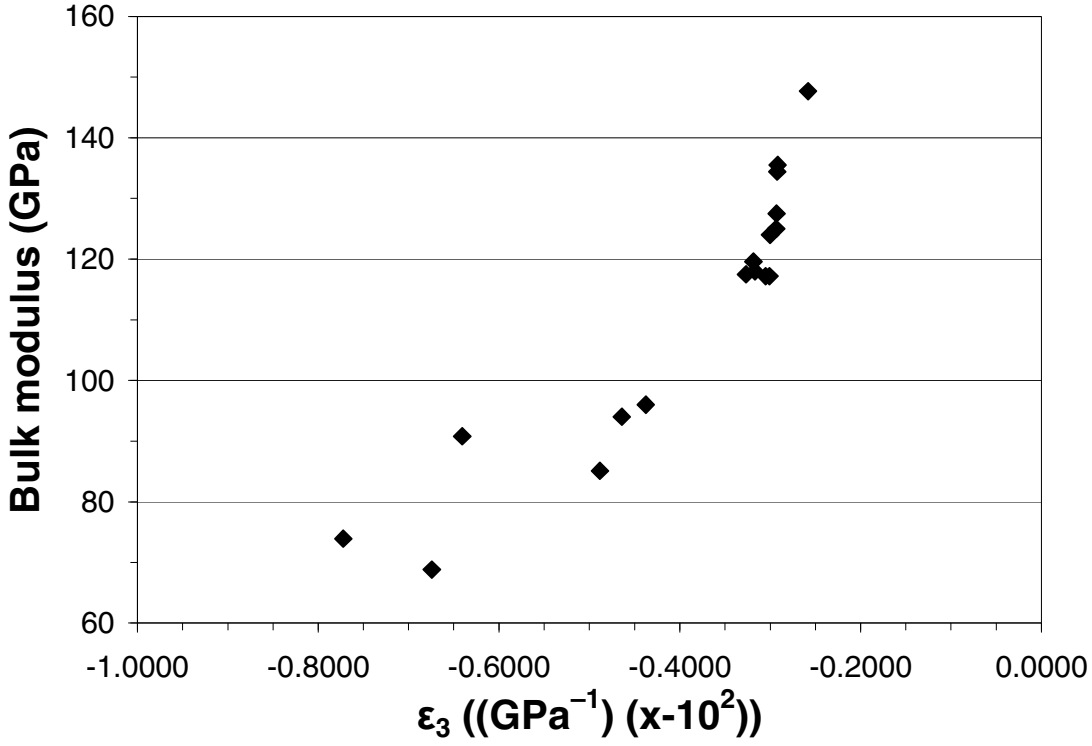

Table 1. $NaGaSi_2O_6$ unit-cell data as a function of pressure

run	aka	*P* (GPa)	*a* (Å)	*b* (Å)	*c* (Å)	β (°)	*V* (Å^3)
P0	post P8	0.0001*	9.5531(6)	8.6971(8)	5.2669(5)	107.627(6)	417.049
P1	1	0.70*	9.5328(5)	8.6783(5)	5.2591(3)	107.576(4)	414.760
P2	2	1.27	9.5154(6)	8.6642(5)	5.2508(4)	107.505(5)	412.839
P3	3	1.99	9.4966(5)	8.6459(5)	5.2420(4)	107.418(4)	410.663
P4	4	2.71*	9.4776(7)	8.630(1)	5.2326(5)	107.341(5)	408.536
P5	5	3.15	9.4697(6)	8.6231(9)	5.2282(5)	107.316(5)	407.578
P6$^{\delta}$	4*	3.60	9.4603(5)	8.6176(7)	5.2233(3)	107.272(5)	406.622
P7$^{\delta}$	6	3.85	9.4493(7)	8.6020(9)	5.2174(5)	107.226(6)	405.060
P8	6_2	4.09*	9.4472(6)	8.5990(9)	5.2156(5)	107.210(6)	404.723
P9	6*	5.40	9.4189(5)	8.5744(7)	5.1996(4)	107.083(5)	401.399
P10	7a	6.00*	9.4060(6)	8.5592(9)	5.1927(5)	107.029(6)	399.719
P11$^{\delta}$	9*	7.05	9.3833(5)	8.5403(7)	5.1794(4)	106.933(5)	397.062
P12$^{\delta}$	10*	7.60*	9.3720(6)	8.5248(8)	5.1723(4)	106.879(6)	395.440
P13$^{\delta}$	11*	8.08	9.3602(5)	8.5126(6)	5.1655(3)	106.815(5)	393.985
P14$^{\delta}$	12*	8.30	9.3546(6)	8.5066(9)	5.1617(5)	106.792(6)	393.227
P15$^{\delta}$	13*	8.70*	9.3443(5)	8.4965(7)	5.1560(4)	106.742(5)	392.004
P16$^{\delta}$	14*	9.10	9.3381(4)	8.4893(6)	5.1522(3)	106.709(4)	391.189
P17$^{\delta}$	15*_new2	9.69*	9.3263(4)	8.4751(6)	5.1451(3)	106.649(5)	389.631
P18$^{\delta}$	16*	10.36	9.3152(4)	8.4627(6)	5.1383(3)	106.593(4)	388.190
P19$^{\delta}$	17*	11.10	9.3057(4)	8.4531(6)	5.1321(3)	106.545(4)	386.986

Note: Space group = *C*2/*c*

* Intensity data collected at this pressure

$^{\delta}$ Second loading of diamond anvil cell with the same crystal

Table 2. Structural parameters for $NaGaSi_2O_6$ in air at room conditions.

atom	*x*	*y*	*z*	B_{eq} (Å^2)	β_{11}	β_{22}	β_{33}	β_{12}	β_{13}	β_{23}
NaM2	0	0.3004(2)	¼	1.41(3)	0.00495(18)	0.00372(18)	0.01164(54)	0	0.00002(25)	0
GaM1	0	0.90189(4)	¼	0.82(1)	0.00268(5)	0.00253(5)	0.00759(16)	0	0.00109(6)	0
Si	0.29119(7)	0.09114(8)	0.23208(12)	0.75(1)	0.00255(8)	0.00242(8)	0.00751(24)	-0.00008(6)	0.00118(11)	-0.00004(9)
O1	0.11179(19)	0.07795(18)	0.13369(34)	0.88(3)	0.00270(18)	0.00296(20)	0.00767(57)	-0.00033(15)	0.00079(26)	0.00010(26)
O2	0.35901(19)	0.25899(19)	0.30196(34)	1.06(3)	0.00344(19)	0.00329(21)	0.01075(58)	-0.00070(16)	0.00206(28)	-0.00072(28)
O3	0.35273(18)	0.00959(20)	0.00780(31)	0.99(3)	0.00301(20)	0.00342(22)	0.00959(62)	-0.00001(15)	0.00166(27)	-0.00073(28)

Note: Space group = *C*2/*c*

Table 3. Structural parameters for $NaGaSi_2O_6$ as a function of pressure

P (GPa)	1 atm (P0 af P8)	0.70 P1	2.71 P4	4.09 P6-2	6.00 P7-1	7.60 P10	8.70 P13	9.69 P15-2
obs refl	489	222	172	221	207	206	206	220
total refl	601	317	236	300	293	287	285	318
p*	0.020	0.090	0.040	0.061	0.046	0.061	0.078	0.035
R_w	0.025	0.095	0.048	0.066	0.052	0.066	0.083	0.041
Ga *y*	0.90601(7)	0.9021(3)	0.9029(2)	0.9032(2)	0.9039(2)	0.9040(2)	0.9040(2)	0.9045(2)
B	0.75(1)	1.04(7)	0.88(5)	1.00(5)	0.95(4)	1.08(5)	1.17(6)	1.24(8)
Na *y*	0.3006(1)	0.3010(10)	0.3012(7)	0.3028(7)	0.3044(6)	0.3042(8)	0.3055(10)	0.3059(8)
B	1.31(2)	1.64(15)	1.31(11)	1.43(10)	1.25(8)	1.38(9)	1.51(12)	1.51(18)
Si *x*	0.29063(4)	0.2906(4)	0.2913(3)	0.2914(3)	0.2919(2)	0.2917(3)	0.2918(3)	0.2920(3)
y	0.09334(4)	0.0912(5)	0.0917(3)	0.0923(3)	0.0926(3)	0.0927(3)	0.0927(4)	0.0931(4)
z	0.22786(8)	0.2322(6)	0.2332(5)	0.2334(4)	0.2337(4)	0.2342(5)	0.2337(6)	0.2349(4)
B	0.73(1)	1.01(8)	0.90(6)	0.98(5)	0.91(5)	1.11(6)	1.18(7)	1.26(9)
O1 *x*	0.1093(1)	0.1117(11)	0.1124(7)	0.1118(8)	0.1111(7)	0.1113(8)	0.1117(10)	0.1114(7)
y	0.0759(1)	0.0775(11)	0.0769(8)	0.0787(9)	0.0804(8)	0.0806(9)	0.0816(11)	0.0823(8)
z	0.1280(2)	0.1359(20)	0.1352(11)	0.1360(13)	0.1378(10)	0.1380(13)	0.1382(16)	0.1381(10)
B	0.82(2)	1.31(17)	1.00(11)	1.22(11)	1.10(9)	1.31(12)	1.36(15)	1.33(20)
O2 *x*	0.3611(1)	0.3588(11)	0.3575(7)	0.3587(8)	0.3581(7)	0.3574(7)	0.3578(9)	0.3591(7)
y	0.2634(1)	0.2602(11)	0.2611(8)	0.2627(8)	0.2622(7)	0.2630(9)	0.2631(11)	0.2642(8)
z	0.2929(2)	0.3059(16)	0.3042(11)	0.3072(12)	0.3088(11)	0.3109(12)	0.3155(15)	0.3161(11)
B	0.98(2)	1.13(16)	0.96(12)	1.17(11)	1.15(10)	1.31(12)	1.38(14)	1.23(21)
O3 *x*	0.3537(1)	0.3531(10)	0.3532(7)	0.3534(6)	0.3547(6)	0.3548(6)	0.3565(7)	0.3563(7)
y	0.0071(1)	0.0106(13)	0.0123(8)	0.0137(9)	0.0145(8)	0.0142(10)	0.0159(12)	0.0166(9)
z	0.0057(2)	0.0116(15)	0.0060(11)	0.0046(10)	0.0048(10)	0.0045(11)	0.0042(12)	0.0023(10)
B	0.93(2)	1.20(17)	1.00(12)	0.97(12)	1.09(10)	1.16(12)	1.25(14)	1.36(21)

Note: $x_{Ga} = x_{Na} = 0$; $z_{Ga} = z_{Na} = ¼$.

* weights computed by $\omega = [\sigma_F^2 + (pF)^2]^{-1}$

Table 4. Selected bond lengths (Å), volumes (Å^3) and angles (°) from structure refinements

P (GPa)	0.0001[δ]	0.70	2.71	4.09	6.00	7.60	8.70	9.69
run	P0 aft P8	P1	P4	P6-2	P7-1	P10	P13	P15-2
R(SiO1)	1.637(2)	1.631(11)	1.623(7)	1.625(7)	1.628(6)	1.621(7)	1.614(9)	1.616(7)
R(SiO2)	1.594(2)	1.603(11)	1.591(7)	1.598(8)	1.583(6)	1.582(8)	1.583(9)	1.587(7)
R(SiO3a)	1.632(2)	1.615(9)	1.626(6)	1.624(6)	1.619(6)	1.618(6)	1.614(8)	1.620(6)
R(SiO3b)	1.645(2)	1.663(9)	1.640(7)	1.638(6)	1.638(6)	1.630(7)	1.636(8)	1.626(6)
<*R*(SiO)>	1.6272	1.6281	1.6200	1.6213	1.6171	1.6126	1.6117	1.6123
V(SiO_4)	2.1988	2.2017	2.1710	2.1764	2.1607	2.1428	2.1385	2.1411
R(NaO1)	2.378(2)	2.376(11)	2.372(8)	2.356(9)	2.338(8)	2.326(9)	2.321(11)	2.312(8)
R(NaO2)	2.393(2)	2.377(9)	2.383(6)	2.368(7)	2.359(6)	2.347(7)	2.326(8)	2.320(6)
R(NaO3c)	2.415(2)	2.404(13)	2.414(8)	2.408(9)	2.388(8)	2.380(9)	2.371(11)	2.373(8)
R(NaO3d)*	2.777(2)	2.772(10)	2.726(7)	2.695(7)	2.661(6)	2.649(7)	2.614(9)	2.596(7)
diff	0.399	0.396	0.354	0.339	0.323	0.323	0.293	0.284
<*R*(NaO)>	2.4905	2.4824	2.4735	2.4568	2.4364	2.4258	2.4077	2.4004
R(GaO1a)	2.063(2)	2.048(10)	2.033(7)	2.029(7)	2.018(6)	2.010(7)	2.012(10)	2.006(7)
R(GaO1b)	1.987(2)	1.995(10)	1.987(6)	1.984(6)	1.983(5)	1.979(6)	1.977(8)	1.973(5)
R(GaO2)	1.912(2)	1.911(10)	1.905(6)	1.889(7)	1.893(6)	1.890(7)	1.889(8)	1.874(6)
<*R*(GaO)>	1.9875	1.9847	1.9747	1.9672	1.9649	1.9599	1.9593	1.9510
V(GaO_6)	10.2693	10.2252	10.0735	9.9630	9.9356	9.8571	9.8522	9.7305
Si-O3-Si	139.4(1)	138.9(7)	138.9(5)	138.7(4)	138.1(4)	138.0(4)	136.8(5)	136.8(5)
O3-O3-O3	172.8(2)	172.0(10)	170.7(6)	169.7(7)	169.1(6)	169.3(7)	168.0(9)	167.5(7)

[δ] Structure at 0.0001 GPa was refined with anisotropic temperature factors
*unbonded pair at all pressures in this study
The O3a in SiO3a is at [0.353,0.010,0.008]
The O3c in NaO3c is at [-0.141,0.241,-0.198]
The O1a in GaO1a is at [0.112,1.078,0.133]

Table 5. Raman peak positions (cm^{-1}) from $NaGaSi_2O_6$ with pressure. Estimated errors in pressure are ±0.05 GPa and in peak positions are ±4 cm^{-1}.

Run #		P15	P14	P13	P12	P11	P10	P9	P8	P7	P001	P6	P5	P002	P4	P003	P004	P005	P006	P2	P007	P008	P1	P009
P (GPa)	0.0001	1.64*	1.73*	2.07*	2.41*	2.99*	3.57*	3.75*	4.94*	5.65*	6.44	6.85*	7.49*	9.46	10.20*	10.81	11.75	12.51	14.07	14.56*	15.3	15.73	15.98*	16.38
v_1	170	--	--	--	--	175	175	176	176	178	177	178	181	180	182	181	182	183	184	183	185	185	185	186
v_2	177	181	181	--	--	185	185	188	188	190	189	191	194	194	--	--	--	194	--	--	--	--	--	--
v_3	186	190	190	191		193	193	195	195	197	196	197	199	199	201	200	201	201	201	201	202	202	202	202
v_4	207	210	210	210	211	212	212	214	214	215	215	216	220	218	221	220	221	222	223	223	224	224	225	226
v_5	217	220	223	--	223	227	227	230	231	232	232	233	237	236	239	238	240	240	241	241	242	243	243	243
v_6	301	308	308	307	308	309	311	314	314	314	314	316	326	324	330	327	330	332	334	335	337	339	339	339
v_7	351	356	357	358	359	361	362	365	365	368	368	370	377	374	379	377	379	379	381	381	382	382	384	384
v_8	370	375	--	376	376	377	--	382	382	386	385	386	393	391	395	394	396	--	--	--	--	--	--	--
v_9	398	404	405	406	407	410	410	414	415	417	417	420	427	424	429	428	430	431	434	435	437	438	438	440
v_{10}	467	--	--	--	--	--	--	475	--	--	482	--	--	--	--	487	493	--	--	--	--	--	--	--
v_{11}	510	514	515	516	517	519	519	524	525	526	526	528	535	533	537	535	538	540	--	--	--	--	--	--
v_{12}	541	543	543	544	545	545	546	548	549	551	550	552	557	556	559	558	560	561	562	564	565	565	567	568
v_{13}	685	692	693	694	696	698	699	703	705	708	706	710	717	716	721	720	722	722	723	722	725	726	727	728
v_{14}	766	773	770	773	774	778	781	782	782	787	786	789	794	795	800	797	801	800	802	801	805	805	806	810
v_{15}**	874	889	890	890	892	896	897	902	905	909	907	910	921	918	925	923	926	928	932	933	935	935	938	939
v_{16}	969	976	978	979	981	983	983	990	991	994	993	996	--	--	--	--	--	--	--	--	--	--	--	--
v_{17}***	1034	1035	1035	1037	1039	1043	1044	1051	1051	1056	1052	1057	1070	1066	1075	1072	1075	1077	1083	1084	1086	1087	1089	1091
v_{18}	1058	1056	--	1061	--	--	--	--	--	--	--	--	--	--	--	--	--	--	--	--	--	--	--	--

* collected during the pressure reduction phase of the experiment

** v_{15} is likely swamped by an ethanol peak at ~885 cm^{-1}

*** v_{17} broadens significantly with pressure, probably due to an interfering peak from the pressure medium.

Table 6. Unit strain ellipsoid parameters for a variety of silicate clinopyroxenes from the literature.

			Unit strain ellipsoid axes (GPa^{-1}) ($\times 10^2$)			Orientation	Strain Ellipsoid Axial Ratios					
Mineral name or formula	Space group	ΔP	ε_1	ε_2	ε_3	$\varepsilon_3 \wedge \mathbf{c}$	ε_1	ε_2	ε_3	V_0*	K_0*	Reference
spodumene	$P2_1/c$	3.34-8.84	-0.1647	-0.2086	-0.3185	16.3	1.00	1.27	1.93	385.50	119.6	Arlt and Angel (2000)
$LiFeSi_2O_6$	$P2_1/c$	1.08-7.22	-0.1891	-0.2760	-0.4641	25.7	1.00	1.46	2.45	414.82	94.0	Downs et al. in prep.
$(Li_{0.85}Mg_{0.09}Fe_{0.06})(Fe_{0.85}Mg_{0.15})Si_2O_6$	$P2_1/c$	0-6.83	-0.1561	-0.2883	-0.4377	29.7	1.00	1.85	2.80	415.67	96.0	Gatta et al. (2005)
$LiScSi_2O_6$	$P2_1/c$	0.66-4.80	-0.2176	-0.2732	-0.4884	30.3	1.00	1.26	2.24	440.39	85.1	Arlt and Angel (2000)
$ZnSiO_3$	$P2_1/c$	1.99-4.80	0.6820	-0.5912	-0.6742	31.7	1.00	-0.87	-0.99	439.63	68.8	Arlt and Angel (2000)
kosmochlor	$C2/c$	0-9.28	-0.1407	-0.2556	-0.2930	32.1	1.00	1.82	2.08	418.87	127.5	Origlieri et al. (2003)
$CaNiSi_2O_6$	$C2/c$	0-7.76	-0.1074	-0.2987	-0.3001	32.7	1.00	2.78	2.79	435.20	124.0	Nestola et al. (2005)
aegirine	$C2/c$	0-10.8	-0.1196	-0.2725	-0.3050	34.1	1.00	2.28	2.55	428.72	117.2	McCarthy et al. submitted
aegirine	$C2/c$	0-9.74	-0.1109	-0.2883	-0.3269	34.2	1.00	2.60	2.95	429.25	117.5	Nestola et al. (2006)
hedenbergite	$C2/c$	0-9.97	-0.1280	-0.3080	-0.3170	35.1	1.00	2.41	2.48	449.86	118.0	Zhang et al. (1997)
diopside	$C2/c$	0-10.16	-0.1385	-0.2841	-0.3008	35.2	1.00	2.05	2.17	438.64	117.2	Thompson and Downs accepted
jadeite	$C2/c$	0-9.17	-0.1391	-0.2274	-0.2922	36.3	1.00	1.63	2.10	402.03	134.4	McCarthy et al. (2007)
jadeite	$C2/c$	0-8.31	-0.1367	-0.2245	-0.2919	36.8	1.00	1.64	2.14	402.42	135.5	Nestola et al. (2006)
$NaGaSi_2O_6$	$C2/c$	0-9.69	-0.1194	-0.2527	-0.2934	36.9	1.00	2.12	2.46	416.90	125.0	This study
$ZnSiO_3$	HP $C2/c$	4.90-7.43	0.1291	-0.3520	-0.6406	37.8	1.00	-2.73	-4.96	423.57	90.8	Arlt and Angel (2000)
$ZnSiO_3$	$C2/c$	0-1.92	0.1128	-0.6189	-0.7723	40.3	1.00	-5.49	-6.85	442.77	73.9	Arlt and Angel (2000)
spodumene	$C2/c$	0-3.19	-0.1483	-0.2419	-0.2581	49.6	1.00	1.63	1.74	388.87	147.7	Arlt and Angel (2000)

Notes: *V_0 as determined by fitting algorithm, K_0 calculated with K'_0 fixed to 4.0.

APPENDIX D

SUGGESTED FUTURE RESEARCH

Suggested Future Research

The studies reported in this dissertation raised a number of questions that could be investigated further.

Phase transition in Na-clinopyroxenes

A logical next step in the study of clinopyroxenes at pressure would be to subject an Na-clinopyroxene such as jadeite to pressures up to ~25 GPa. Such pressures can be achieved with a gas-loaded diamond anvil cell. Examination of the crystal with X-ray diffraction may confirm the postulated $C2/c \rightarrow C2/c$ phase transition, with Na at M2 changing from 6- to 8-coordinated with oxygen. The Na-pyroxene would then have a bond topology identical to diopside and should remain on the "upper trend" in terms of its compression behavior. The pressures of the expected phase transitions in various Na-pyroxenes are predicted in the other appendices of this dissertation.

Changes in Raman spectra with pressure

The study of an Na-clinopyroxene to pressures over 20 GPa using X-ray diffraction may also allow explanation of the changes observed in the Raman spectra to 16.4 GPa in $NaGaSi_2O_6$, as detailed in Appendix C.

Bond theory explanation of the antipathetic/sympathetic bonds

A bond between two atoms tends to seek an equilibrium length based on the conditions within the structure. As pyroxene structures are compressed, bonded distances decrease as all interatomic distances decrease. For antipathetic bonds to restrain tetrahedral rotation, the rotation must be attempting to hold the bridging O3 atom farther

from M2 than bond equilibrium would dictate. The antipathetic/sympathetic bond phenomenon needs to be examined in detail and explained in terms of bond energies.